Characterization of human iPS cell derived neurons and synapse impairment by amyloid-β

Inaugural-Dissertation

zur Erlangung des Doktorgrades
der Mathematisch-Naturwissenschaftlichen Fakultät
der Heinrich-Heine-Universität Düsseldorf

vorgelegt von

Simon Klapper
aus Duisburg

Düsseldorf, April 2015

aus dem Institut für Neuro- und Sinnesphysiologie
der Heinrich-Heine-Universität Düsseldorf

Gedruckt mit der Genehmigung der
Mathematisch-Naturwissenschaftlichen Fakultät der
Heinrich-Heine-Universität Düsseldorf

Referent: Prof. Dr. K. Gottmann

Koreferent: Prof. Dr. D. Willbold

Tag der mündlichen Prüfung: Mittwoch, 13.05.2015

Abstract

The central nervous system (CNS) is a complex, highly organized dynamic structure which uses neurons to receive, process and send information. Its complexity renders the system vulnerable to a wide range of neurologic and psychiatric diseases. Especially dementia, a group of mainly incurable neurological diseases, which occur mostly late in the life of patients, massively affect cognitive function and are gaining more importance with the increasing average life span. The frequent use of animal models to gain insights into the diseases is currently challenged by the failure to transfer the results from animal models to human patients for development of drugs and therapies. Fortunately, the advent of the human induced pluripotent stem cell (iPSC) technology as a more physiological disease model is providing a promising alternative to animal models. However, differentiation to mature human neuronal networks is still a challenge as human neurons take a rather long time to maturate. In this work, a recently developed protocol for the generation of mature human iPSC derived neurons was used and compared to novel neural culture system, that additionally contained human astrocytes to enhance neuronal maturation. Interestingly, in depth electrophysiological analyses revealed an enhanced excitability of a neuronal subpopulation by human iPSC derived astrocytes. This appeared to have an enhancing effect on the overall network activity in cultures with astrocytes, because without astrocytes, a reduced ability to generate population bursts was detected by Ca^{2+} imaging. Surprisingly, properties of excitatory snyapses appeared not to change upon astrocyte co-culture.

The most common form of dementia is Alzheimer's disease (AD) with its deleterious effects on memory and personality. Apart from risk factors and genetically inherited variants of the disease, its cause is not yet understood, making it subject to intensive research. One key factor, the amyloid-β peptide (Aβ) is of special interest as it seems to be a major player in the aetiology of the disease. Aβ acts as a synaptotoxic molecule in the CNS, and finally leads to further aggregation to amyloid plaques and to cell death, both being pathological hallmarks of AD. The variety of Aβ species and the use of animal models complicate research aimed at defining a molecular pathway of Aβ mediated toxicity. In the present work, a simple but physiologically relevant synthetic Aβ preparation was used and characterized. Furthermore, this Aβ preparation was applied to mature human iPSC derived neurons, exhibiting synaptotoxic effects without affecting cell viability. Finally, Aβ might express its synaptotoxicity depending on the plasticity state of the synapse. This was addressed by application of naturally secreted Aβ to up-scaled synapses of murine hippocampal neurons. Interestingly, up-scaled synapses appeared to be more prone to Aβ mediated impairment of glutamatergic synaptic transmission.

Zusammenfassung

Das zentrale Nervensystem (CNS) ist ein komplexes, hoch organisiertes Organ welches durch Neuronen Informationen empfängt, verarbeitet und zurücksendet. Seine Komplexität macht es jedoch empfänglich für neurologische und psychiatrische Erkrankungen. Besonders die Demenz, eine Gruppe von hauptsächlich unheilbaren neurologischen Krankheiten, die meist erst im hohen Alter auftreten und die kognitiven Funktionen stören, gewinnen mit steigendem Durchschnittsalter mehr an Bedeutung. Die bisherige Verwendung von Tiermodelle, um Einsichten in Mechanismen dieser Erkrankungen zu erforschen birgt die Schwierigkeit, die gewonnenen Erkenntnisse auf den Menschen zu übertragen. Dabei lässt die Entwicklung von menschlichen, induzierten, pluripotenten Stammzellen (iPSC) hoffen, dass in Zukunft physiologischere krankheitsmodelle zur Verfügung stehen werden. Die Differenzierung zu reifen, humanen, neuronalen Netzwerken ist immer noch schwierig, da Neuronen relativ lange brauchen, um funktionell auszureifen. In der vorliegenden Arbeit wurde ein kürzlich entwickeltes Protokoll zur Erzeugung reifer, humaner Neuronen aus iPSC angewandt und mit einem neuen neuralen Kultursystem verglichen, welches zusätzlich Astrozyten enthielt, um die neuronale Ausreifung zu verbessern. Detaillierte funktionelle Messungen zeigten dabei eine erhöhte Erregbarkeit einer Untergruppe von Neuronen in Kulturen, die humane Astrozyten aus iPSC enthielten. Dies schien eine positive Auswirkung auf die synchrone Netzwerkaktivität von Kulturen mit Astrozyten zu haben, da Kulturen ohne Astrozyten eine verminderte Fähigkeit zur Ausbildung von synchroner Netzwerkactivität zeigten. Überraschenderweise schienen die Astrozyten keinen Einfluss auf die erregende synaptische Übertragung zu haben.

Die häufigste Form der Demenz ist die Alzheimer-Krankheit (AD), mit verheerenden Auswirkungen auf Gedächtnis und Persönlichkeit. Abgesehen von einigen Risikofaktoren und erblichen Varianten von AD, ist ihre Ursache nicht hinreichend geklärt, sodass sie Objekt zahlreicher Forschungsstudien ist. Besonders dem Amyloid-β Peptid (Aβ) gilt dabei Interesse, da es eine Hauptrolle in der AD zu spielen scheint. Es wirkt synaptotoxisch im CNS und führt letztlich zur Aggegation zu senilen Plaques und Zelltod. Die Fülle an einzelnen Aβ-Strukturen und die Verwendung von Tiermodellen haben die Aufdeckung von Aβ-Signalwegen bisher erschwert. In der vorliegenden Arbeit wurde eine physiologische, synthetische Aβ-Präparation verwendet und charakterisiert. Diese wurde dann auf humane Neurone aus iPSC gegeben, wobei sie eine toxische Wirkung auf die Synapsen zeigte, ohne Zelltod zu induzieren. Schließlich wurde gezeigt, dass die synaptotoxischen Wirkungen von Aβ von deren Plastizitätszustand abhängen könnten, indem natürlich sekretiertes Aβ auf hoch skalierte Synapsen von hippokampalen Mausneuronen gegeben wurde. Interessanterweise schienen hoch skalierte glutamaterge Synapsen empfindlicher gegenüber den toxischen Wirkungen von Aβ zu sein.

Table of contents

1 Introduction

The brain and thus the central nervous system (CNS) is a highly complex structure which is specialized to receive, integrate and send information from and to regions in the whole body, performing autonomous functions some of which are breath and heart rate control, gut muscle tension and movement coordination. Finally, it is the home of human consciousness and personality, the source of free will and thought. This requires a complex, carefully balanced information processing system. In the brain, this is achieved mainly by cells called neurons. They code information in the form of electrical signals and communicate with each other through chemical signals (synapses). Neurons are supported by glial cells and blood vessels. The complexity of the system makes it vulnerable to various psychiatrical and neurological diseases and especially neurodegenerative diseases and dementia are gaining importance as they are getting more and more abundant in an aging society.

1.1 Neuronal morphology and function

The most obvious cell type in the brain is the neuron, which conducts the primary function of transmitting and integrating information from other neurons and/or sensory cells. The brain consists of around 10^{11} neurons and there are more than thousand types of them (Kandel et al., 2000). However, all of them share the same basic architecture (Figure 1). Neurons consist of a cell soma which contains the nucleus. From there, small branches of membrane, the dendrites, are sprouting, generating long processes which are designed to receive synaptic inputs from other neurons. To send information, the axon, a long, very thin tube-like structure that originates at the initial segment is connected to other neurons. It is usually much thinner, but longer than dendrites and can have a high number of branches.

To receive, integrate and send information, neurons are highly specialized to generate fast ion flux across their membrane, thus creating electrical signals. The membrane itself is a good insulator because of its lipid content, whereas selective ion channels inside the membrane can mediate different currents, depending on channel density, ion type and electromotive force. The electromotive force is determined by the balance between two factors: The concentration gradient of the ions and the electric potential across the membrane. At rest, the membrane potential is usually negative (typically in the range of -85 mV to -60 mV in pyramidal neurons; Bean, 2007) because leak channels mediate mainly the efflux of K^+ which is higher

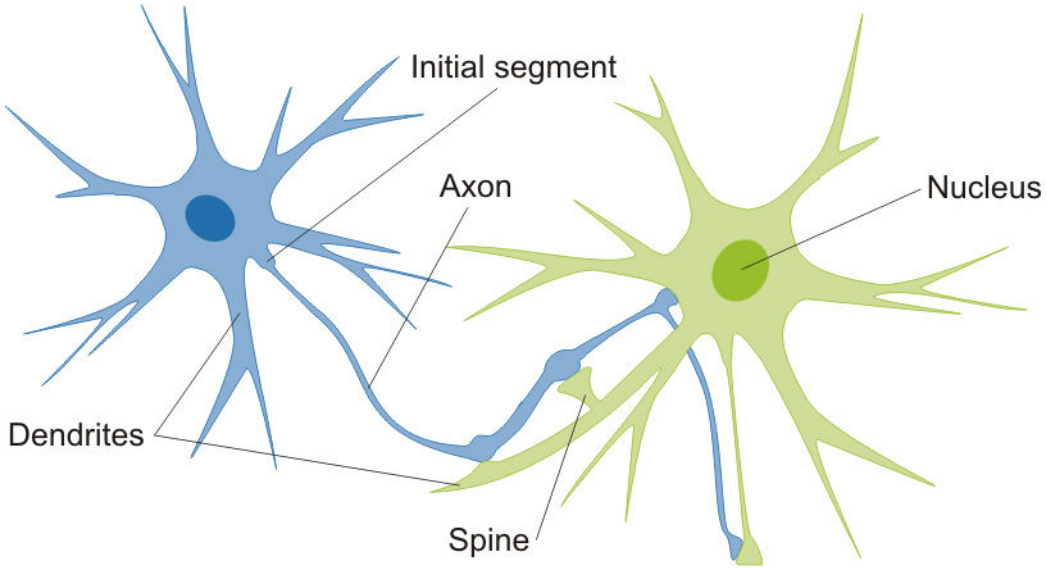

Figure 1: Morphology of neurons.
Neurons are connected via axons, building synapses on dendrites, spines, somata and other synapses.

concentrated inside the cell, thus creating a constant negative current, whereas passive flow of Na^+ ions into the cell is partially counteracting this negative current. A Na^+-K^+ ATPase pump constantly transports three Na^+ ions out of and two K^+ ions back into cell to keep the ion gradients.

After ion influx, the resulting current is propagated through space along the membrane by electrotonic conductance, which is determined by the length constant and the time constant tau. Both describe the length and the time after which the amplitude of the resulting potential is attenuated to $1/e \approx 37\%$ of the initial amplitude, respectively. In addition to this passive conductance which is limited in time and space, neurons are capable to mediate active propagation of signals through long distances. This active signal is called action potential (AP) and is transmitted along the axon.

1.1.1 Signal propagation by action potentials

Inside a single neuron, the main way to pass a signal along spatial distance, is the AP. It is generated at the initial segment upon depolarization above the voltage threshold (Bean, 2007; Figure 2). Then, voltage dependent Na^+ channels open to mediate a strong positive ion influx along the concentration gradient, which further depolarizes the cell membrane and generates the AP upstroke. After reaching the overshoot above 0 mV, these channels close and inactivate and can not be opened again before repolarization, thus stopping the influx at the peak of the

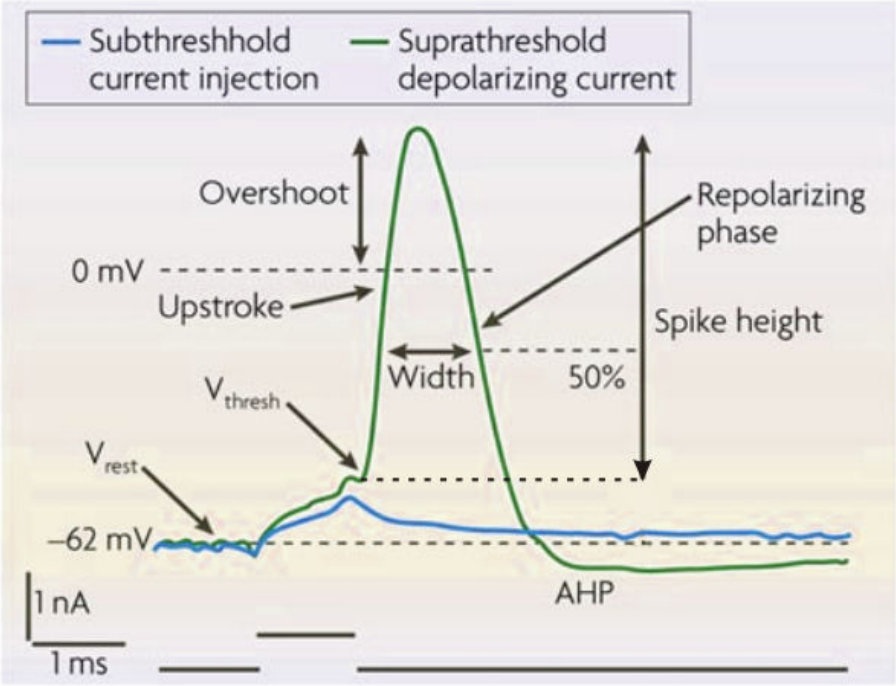

Figure 2: Anatomy of an action potential.
Modified after Bean (2007). An action potential (AP) recorded from a CA1 pyramidal neuron of a rat hippocampus, illustrating commonly measured parameters. The AP was elicited by the injection of just-suprathreshold depolarizing current (green). Use of a brief (1 ms) injection (bottom, black) has the advantage that the spike and the afterpotentials are not directly influenced by the current injection. The response to a subthreshold current injection is also shown (blue). V_{rest} = resting potential, V_{thresh} = voltage threshold (most negative voltage that must be achieved by the current injection for all-or-none firing). The upstroke of the AP typically reaches a maximum velocity at a voltage near 0 mV. Overshoot = peak relative to 0 mV. Spike height = peak relative to V_{thresh}. AHP = afterhyperpolarization. Spike width = width at half-maximal spike amplitude.

AP. At the same time, voltage dependent K^+ channels open which mediates an inverse current flow, because K^+ flows out of the cell. Thus, the membrane potential is repolarized to its negative value, and Na^+ channels can be opened again upon the next depolarization at the initial segment. In some neurons, the repolarizing current drops below the resting potential and creates an afterhyperpolarization (AHP), which then slowly recovers to reach the resting potential. Because of their shape, APs are often named spikes.

Because of the inactivation of the voltage gated Na^+ channels, propagation of the AP can only happen in the direction where Na^+ channels are in a resting state which usually is away from the soma and the initial segment to the axon terminal. To safe energy and to make transmission faster, axons are myelinated in the mammalian CNS. Oligodendrocytes provide a special myelin containing sheath of membrane which is wrapped around the axon, thus creating an insulation. Active AP generation is interrupted here and only performed at the nodes of Ranvier, small areas on the axon which are not covered by myelin. Myelinated

pieces of axon conduct the charge in an electrotonic fashion which is more efficient because of the additional insulation by myelin.

When the AP reaches the axon terminal, it is usually triggering synaptic transmission, a way to chemical transmit signals between neurons. However, as APs are generated by an *all or none* principle, their amplitude is constant and does not carry any information. Information can thus only be mediated by the timing of APs which renders the AP frequency and firing rhythm very important parameters for signal transduction by APs and information coding by networks.

1.1.2 Transmission at the chemical synapse

Connections between neurons are made by so called synapses, areas of highly specialized dynamic structures consistent of small compartments of cell membrane with tens of nm distance to the specialized cell membrane of the next neuron (Laßek et al., 2015). While the presynaptic cell is usually sending information through the axon via APs, the postsynaptic cell is receiving it through the soma or dendrites, where the receiving end on dendrites can be a separate very small membrane structure called spine (Figure 1). A single neuron can develop a large amount of synapses in its axon, whereas dendrites and soma can receive even more synaptic inputs. The type of the synapse is usually represented by the type of neurotransmitter used, which can mediate negative or positive current, depending on the channel and transmitter type involved. Also, metabotropic receptors can be activated by the neurotransmitter which mediates a second messenger response instead of direct current flow. The most prominent excitatory neurotransmitters in the CNS is glutamate.

Glutamatergic synaptic transmission is initiated by an AP running down the axon in the presynaptic neuron and depolarized the presynaptic terminal (Figure 3A). This opens voltage dependent Ca^{2+} channels, followed by Ca^{2+} influx (Figure 3B) which makes the presynaptic vesicles fuse with the cell membrane via the SNARE (soluble N-ethylmaleimide-sensitive factor attachment proteinreceptor) complex (Acuna et al., 2014; Figure 3C). The neurotransmitter is thus released into the synaptic cleft and diffuses and binds to postsynaptic receptors (Figure 3D), for example AMPA (α-amino-3-hydroxy-5-methyl-4-isoxazolepropionic acid) and NMDA (N-Methyl-D-aspartic acid) type glutamate receptors. These are ligand activated cation channels which mediate positive inward current. This positive current depolarizes the inside of the postsynaptic neuron to create an excitatory

postsynaptic potential (EPSP; Figure 3E) and if several of these depolarizations add up until they cross a certain threshold at the initial segment, an AP is generated. The excess glutamate is taken up by the presynaptic neuron or astrocytes via glutamate transporters (Figure 3F). In the astrocytes, glutamate is converted to glutamin and transported back to the presynaptic neuron, where it is converted to glutamate again. Endocytosed vesicles are refilled with glutamate and set up for the next presynaptic release (Figure 3G). These processes happen in a few ms and because of the multiple signals involved can be intensively modulated.

1.1.3 Synaptic plasticity

Synapses are highly dynamic structures which can change their way of signal transduction according to their activity (Malinow and Malenka, 2002). There are many types of plasticity processes, some act in the time range of milliseconds to minutes, while others can effect signaling for hours to years. Signals can be amplified and attenuated depending on the activity pattern and the type of synapse present. The most prominent plasticity processes are long term potentiation (LTP) and long term depression (LTD). The names already state the time scales and direction of these processes. LTP is an increase of postsynaptic potential response to the same presynaptic stimulus after a high frequency stimulation (tetanus). It involves two phases with different time scales. The first phase takes around several hours and is characterized by its NMDA receptor dependence. This receptor only opens upon glutamate binding and postsynaptic depolarization, making it a coincidence detector. Only if a second signal follows the first one before the postsynaptic depolarization is attenuated, NMDA receptors open and mediate Ca^{2+} influx in addition to a Na^{+} influx which increases the response. Ca^{2+} is acting as a second messenger and influences a wide range of signaling cascades, where at the end protein synthesis is involved. The latter is responsible for the late second phase of LTP, where the synapse structure is permanently altered by changes in molecular and structural composition. It can last for months. Interestingly, LTD is mediated by the same processes as LTP and is solely dependent on the timing of presynaptic signals, pointing to another activity timing sensor in the postsynaptic compartment. As plasticity processes are regulated on a single synapse level, they could easily lead to over excitation in the postsynaptic neuron if multiple synpases are potentiated. This might create an infinite, unconstrained potentiation, disrupting the synapses physiological function by losing specificity and eventually leading to cell death due to excitotoxicity. Thus, t is necessary to keep neuronal activity at reasonable

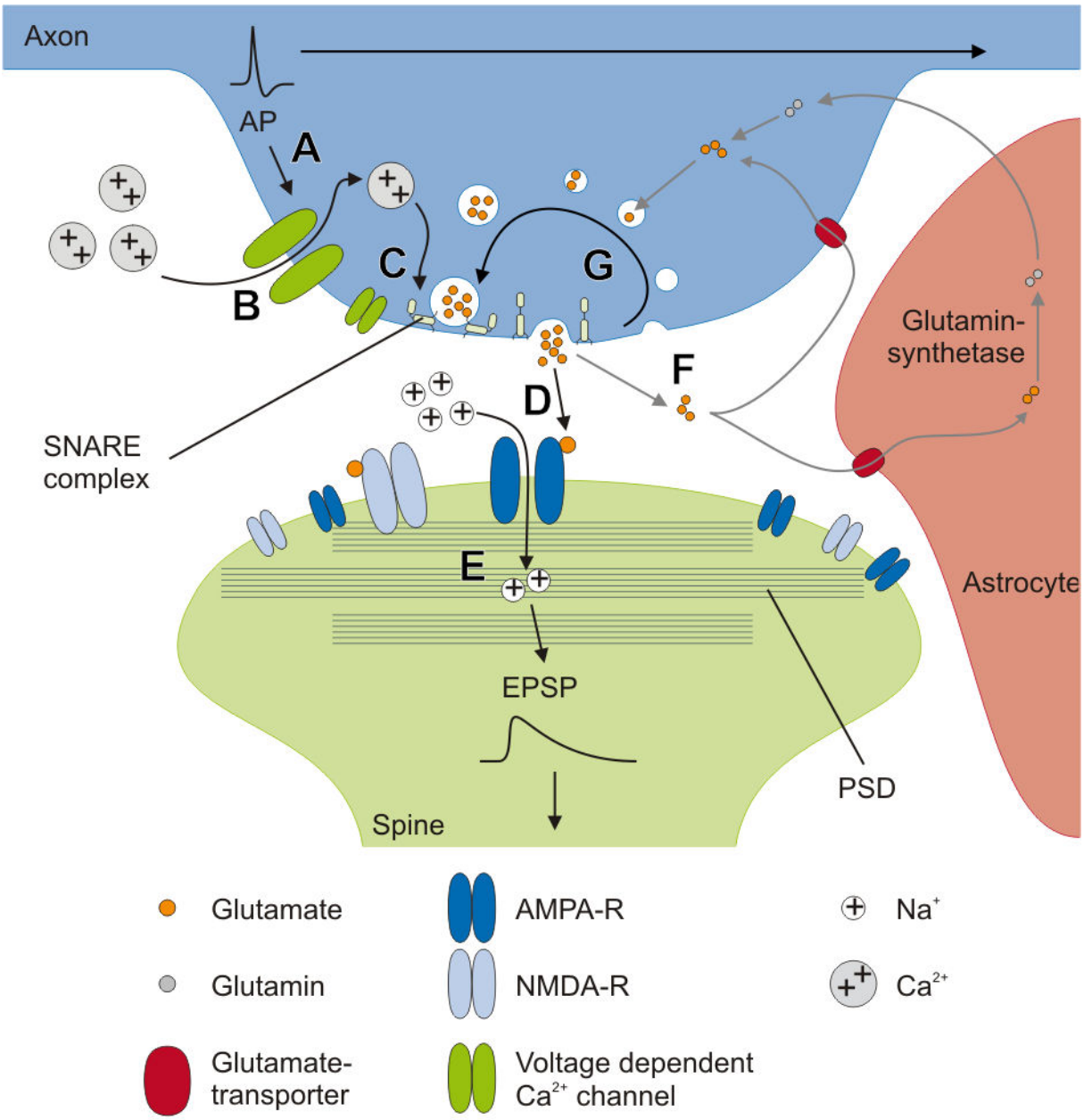

Figure 3: Signal transmission at the glutamatergic synapse.
A: An action potential (AP) runs down the axon and depolarizes the presynaptic terminal. **B:** Voltage dependent Ca^{2+} channels open upon depolarization of the presynaptic terminal and mediate Ca^{2+} influx. **C:** Ca^{2+} triggers the fusion of synaptic vesicles with the presynaptic membrane via SNARE complex. **D:** Glutamate is realeased from synaptic vesicles and diffuses to the postsynaptic membrane, binding to AMPA and NMDA receptors bound to the scaffold of the postsynaptic density (PSD). **E:** Glutamate binding opens AMPA receptors which mediate Na^{+} influx and thus an excitatory postsynaptic potential (EPSP). **F:** Glutamate is taken up through glutamate transporters by the presynaptic neuron and astrocytes, where it is converted to glutamin by glutamin synthetase and transported back to the presynaptic neuron where it is converted back to glutamate. **G:** Endocytosis is maintaining the vesicle cycle, where vesicles are refilled with glutamate and set up for the next release.

levels to maintain information processing but at the same time, the plasticity code of individual synapses has to be maintained, too (Figure 4A). This process is called homeostatic

scaling and it is thought to function as a neuron wide proportional scaling mechanism that maintains relative synaptic strength but changes overall input strenght, in glutamatergic synapses mainly through changes in AMPA receptor number (Figure 4B; Turrigiano, 2008).

1.1.4 Neuronal networks

Although the neuron itself has already integrative functions on the single cell level, a single neuron is powerless unless it is connected with several other neurons of different types to create a network that is able to do dynamic computations of information. These dynamics are mainly driven by the synapses, but also by the neurons themselves and their connections. In networks, different types of neurons and thus synapses play an important role. The major difference can be deduced from the type of transmitter the neuron is expressing. This has direct influence on the effect of signal transmission. That is, whether transmission is inhibitory or excitatory, for example. These two states are already enough to build highly complex networks which express specific computational functions. Adding more transmitter

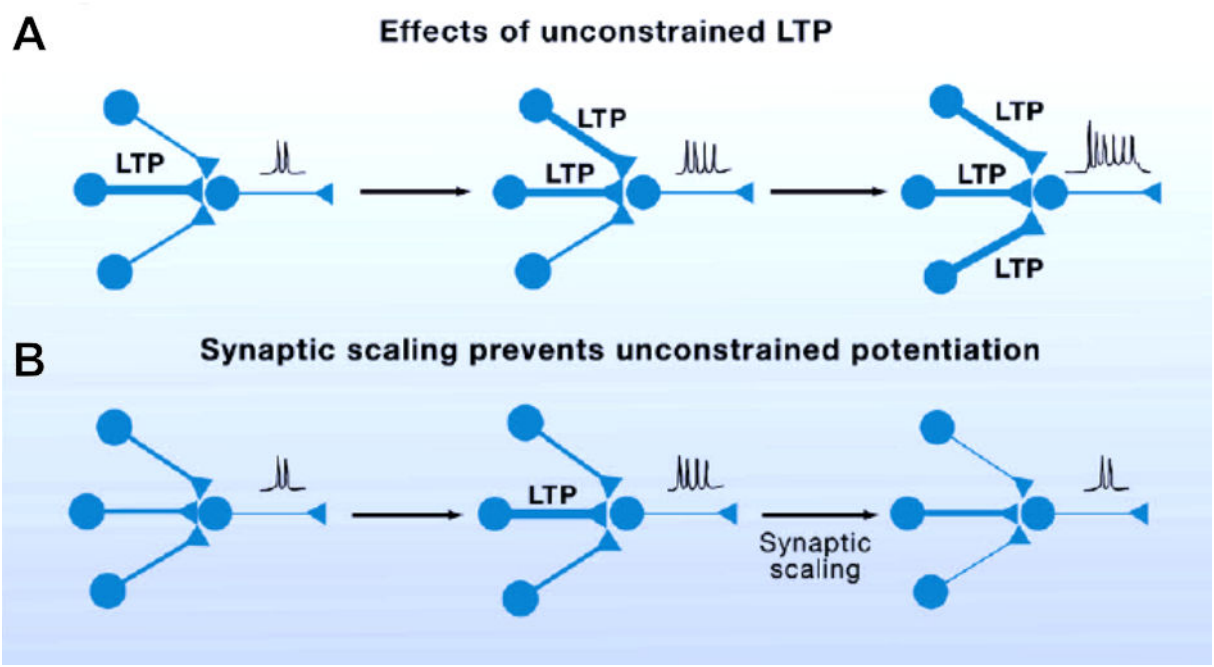

Figure 4: Synaptic scaling prevents unconstrained potentiation.
From Turrigiano (2008). **A:** Unconstrained LTP will lose synapse specificity, because when one input undergoes LTP and drives the postsynaptic neuron more strongly, it makes it easier for other inputs to make the postsynaptic neuron fire, and they begin to undergo LTP as well. **B:** Homeostatic synaptic scaling prevents this runaway potentiation. When LTP of one input increases postsynaptic firing, synaptic scaling will reduce the strength of all synaptic inputs until the firing rate returns to control levels. Note that synaptic strengths are reduced proportionally, so that the relative strength of the potentiated synapse remains the same.

types, different AP firing behaviors of neurons and synaptic plasticity processes, not to mention the number of these elements present in the brain, a large range of mechanisms is at hand to solve the most complex problems.

During development, once the morphological structures like dendrites, axons and synapses have been set up, the network experiences a transition from almost no activity to a hyperexcited state in the brain (Ben-Ari, 2001). For a limited period of time, neurons in the network synchronize to each other in a regular pattern, the population bursts which are thought to be important for synaptic priming of future connections in a range of brain structures. Later in development, these simple synchronous population bursts are taken over by functional, more complex patterns of activity. However, in *in vitro* cultures, these population bursts seem to stay for a long period of time, although with changes in the complexity of the rhythm and are regarded as a sign of maturity (Chiappalone et al., 2006). Massive synchronization in the adult brain instead is a sign of neurological malfunction, like in epilepsy (Kramer and Cash, 2012).

1.1.5 Glial cells support neuronal function

Glial cells play an important role in the support of neurons by clean up of the extracellular space and the synaptic cleft by uptake of excess and toxic ions and neurotransmitter (Figure 3F). However, recent work shows that a specific subtype of glial cells, the astrocytes can have an active influence on the development and maintenance of synapses via secreted signals. Astrocyte signals can induce neuronal synapse formation through thrombospondin (Christopherson et al., 2005) or hevin (Figure 5A, B) and inhibit neuronal synapse formation through SPARC (secreted protein acidic and rich in cysteine; Kucukdereli et al., 2011). Furthermore, astrocytes regulate neuronal glutamate receptor localization and synaptic strength (Allen et al., 2012). There, glypican 4 and 6 secreted by astrocytes can increase synaptic levels of AMPA receptors containing GluA1 subunits and induce structural synapse formation (Figure 5C). In addition to its inhibition of synaptogenisis, SPARC can also reduce the number of synaptic AMPA receptors (Jones et al., 2011; Figure 5D).

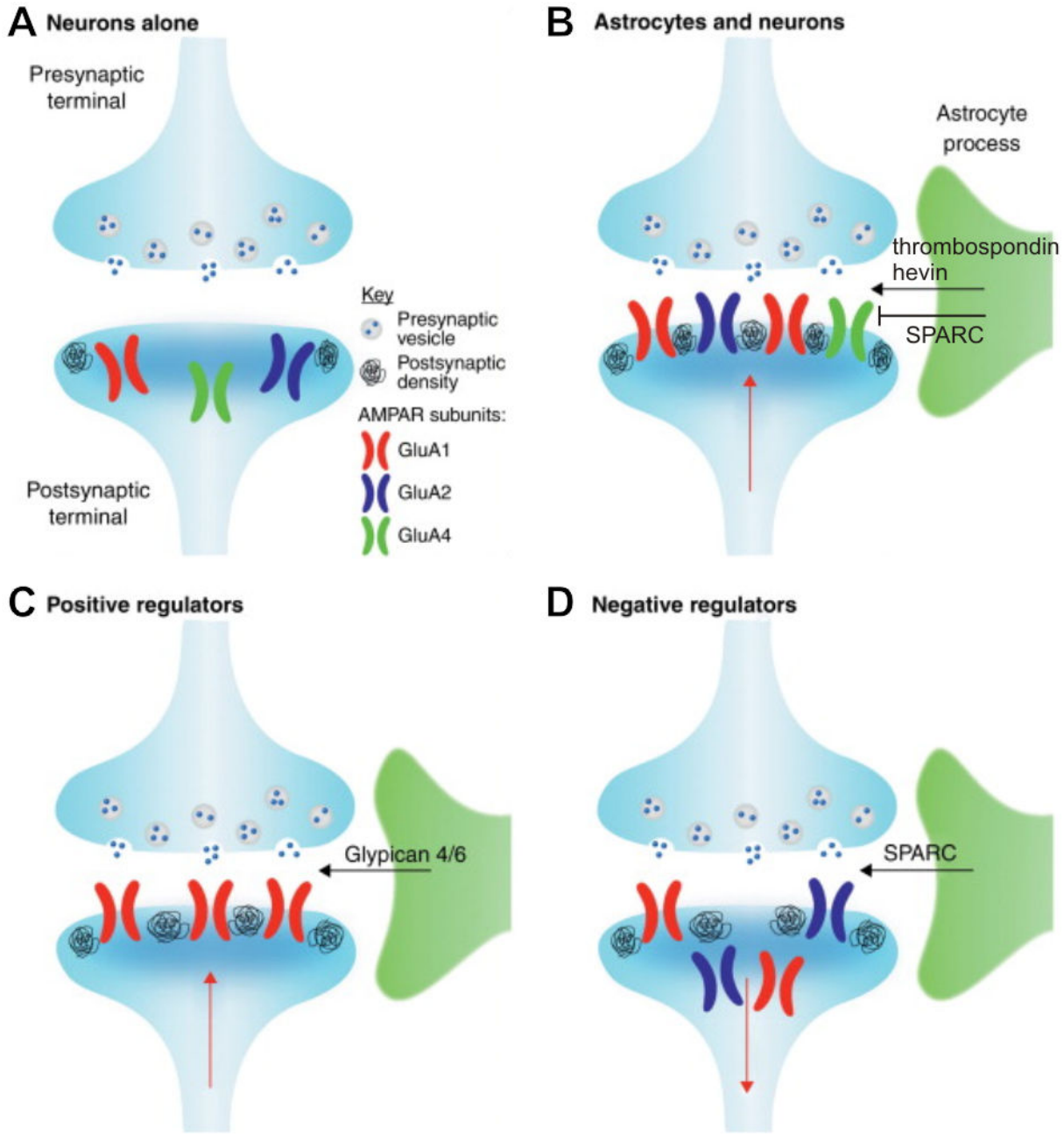

Figure 5: Astrocyte signals regulate synaptic glutamate receptors.
Modified after Allen (2013). **A:** Neurons grown in isolation in vitro form few synapses, and these synapses have low levels of AMPA glutamate receptors. **B:** The presence of astrocytes enhances synapse formation between neurons via thrombospondin and hevin, which is inhibited by SPARC. **C:** Astrocytes secrete positive regulators of AMPA receptors that increase synaptic levels of AMPA receptors and synaptic strength, including glypicans 4 and 6 which increase synaptic levels of the GluA1 subunit of the AMPA receptor. **D:** Astrocytes also secrete negative regulators of AMPA receptors that decrease synaptic levels of AMPA receptors and synaptic strength, including SPARC.

1.2 Alzheimer's disease

Alzheimer's disease (AD) is a neurodegenerative disease and a form of dementia which was named after Alois Alzheimer, a psychiatrist who described and reported the disease for the

first time as a distinct neurodegenerative disorder in the year 1907. Today, it is estimated that a fast growing number of 44 million people currently live with dementia worldwide while AD makes 50 to 75% of the cases (Prince et al., 2014). There is a sporadic and a genetically inherited variant, familial AD (FAD) which usually occurs earlier in live. The sporadic form has an unknown cause, although some genes have been identified to bear risk factors, for example the apolipoprotein E ε4 gene (Roses, 1996). FAD involves mutations in genes for APP (amyloid precurosr protein) or its cleavage enzymes, for example presenelin-1 and -2 (Kim et al., 2014). All forms of AD are characterized by general symptoms of dementia like cognitive impairment, memory loss, speech problems and personality change.

The pathology of AD is defined by the loss of neurons in the cortex which is preceded by the accumulation and aggregation of amyloid-β peptide (Aβ) into amyloid plaques and the formation of fibrilar tangles, consistent of tau protein. Additionally, a strong inflammatory response and oxidative stress are observed during development of the disease. However, both Aβ and tau pathologies are regarded as the hallmarks of AD and are thus studied intensively. Especially Aβ is suspicious to be an early cause of disease symptoms due to its potential to specifically interfere with plasticity at excitatory synapses (Mucke and Selkoe, 2012).

1.2.1 Physiological turnover and function of the amyloid-β peptide

Aβ is a fragment of APP, which is a transmembrane protein with several functions in neural development and function (Thinakaran and Koo, 2008). It is cleaved by enzymes in two different pathways. The non-amylodiogenic pathway is characterized by a cleavage by α-secretase which generates the fragments C38 and sAPPα (Figure 6). The amyloidogenic pathway creates the Aβ peptide by γ-secretase mediated cleavage from C99, leaving the AICD as a residue. C99 is generated by the β-secretase mediated cleavage of sAPPβ from APP. As the γ-secretase does not only cleave at one site, Aβ peptides of lengths 38 to 43 amino acids are created. The 42 amino acids long $A\beta_{42}$ is the most hydrophobic and thus most prone to aggregation, rendering it the a primary candidate as a mediator and thus a therapeutic target of AD (Funke and Willbold, 2012). It is thought that a primary event of the disease is a shift in production of Aβ peptides to a higher ratio of $A\beta_{42}$ to $A\beta_{40}$ (Kuperstein et al., 2010). Furthermore, Aβ is released in amounts that depend on neuronal activity (Bero et al., 2011).

Aβ itself is processed in different ways, mainly by neprilysin and IDE (insulin degrading enzyme; Duyckaerts et al., 2009). Furthermore, Aβ is transported out of the parenchym of the

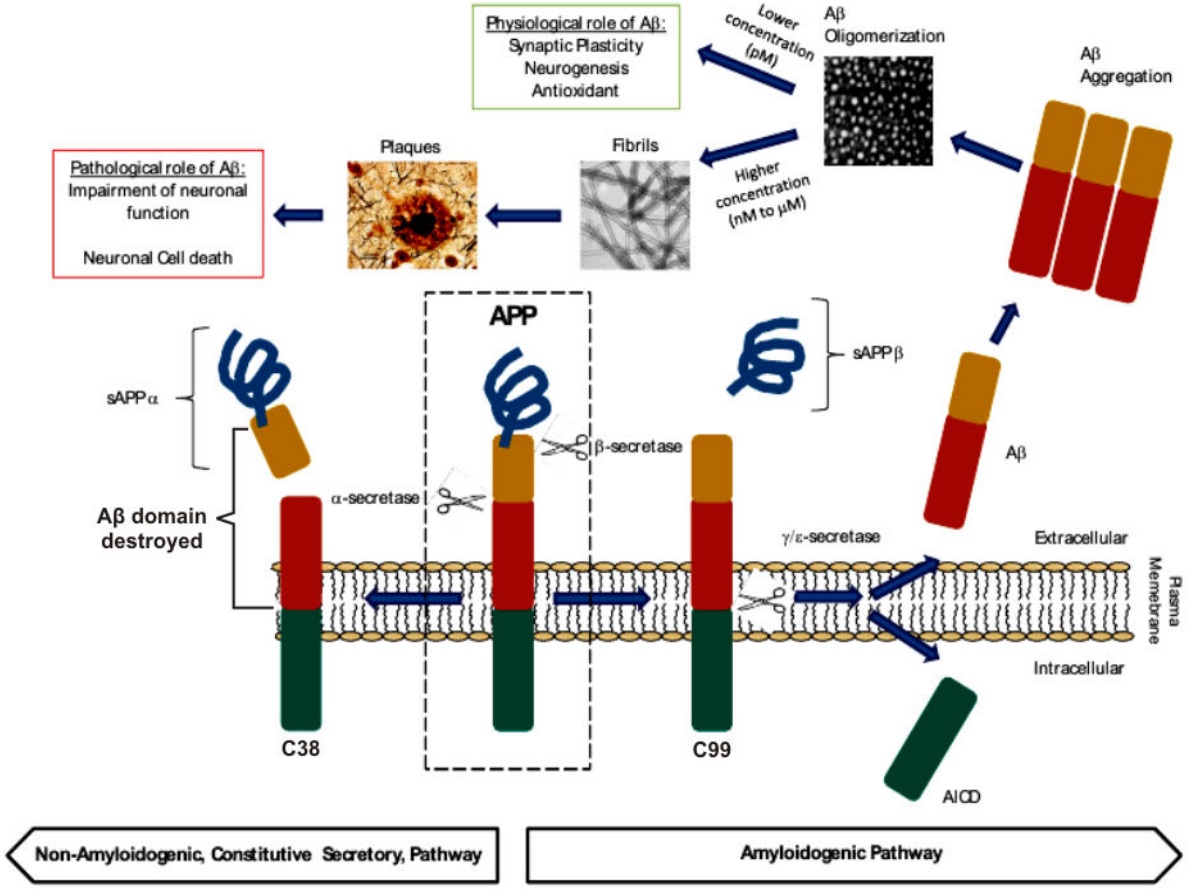

Figure 6: Proteolytic processing of APP.
Modified after Cárdenas-Aguayo et al. (2012). Non-amyloidogenic processing of APP (left): Sequential processing of APP by membrane-bound α- and γ-secretases. α-Secretase cleaves within the Aβ domain, thus precluding generation of intact Aβ peptide. The fates of N-terminally truncated Aβ (p3) and AICD are not fully resolved. Amyloidogenic processing of APP (right): Sequential action of membrane-bound β- and γ-secretases. Aβ peptide is released to the extracellular space and forms different aggregation species with functions in plasticity and neurogenesis. At higher concentrations, this leads to neurotoxicity and plaque formation. C = C-terminal fragment.

brain through the blood-brain barrier by LRP-1 (lipoprotein receptor like protein; Shibata et al., 2000) or P-glycoprotein (Cirrito et al., 2005) over interstitial fluids or the lymphatic system (Weller et al., 2009). A back transport mechanism is mediated by RAGE (receptor for advanced glycation endproducts; Deane et al., 2003).

At low, physiological concentrations of Aβ (pM range), it can function as a neurotrophic factor (Plant et al., 2003) with a role in neurogenisis, as a modulator of synaptic plasticity (Garcia-Osta and Alberini, 2009) and might play a role in homeostasis of calcium ions, metal ions and oxidative stress (Zou et al., 2002). It is thought that higher concentrations of $A\beta_{42}$ lead to an overshoot of these functions and thus to a more toxic action in AD, as it is known

from the FAD patients, who bear mutations in genes relevant to Aβ metabolism (for example in the genes for presenilin, which is an important part of the γ-secretase complex).

1.2.2 Synaptotoxicity mediated by amyloid-β peptide

It was shown that synaptic loss is better correlated with AD symptoms than amyloid plaque deposition (De Kosky and Scheff, 1990), giving rise to the idea that soluble forms of Aβ have an early effect on synapses before cell death is initiated and that plaques get only visible at later stages of the disease. Aβ, apart from different lengths, can have different aggregation states, too, ranging from monomer over dimer, trimer, higher oligomers to protofibrils and fibrils. The latter are the main component in the amyloid plaques and are insoluble. Thus they are regarded as inactive, although they might be source of smaller, soluble aggregation states, somewhat buffering the soluble Aβ species (Grüning et al., 2013). They might also act as seeds, accelerating aggregation of other Aβ peptides (Stine et al., 2003). However, evidence is there that more mobile, medium sized oligomers are the major toxic species (Walsh and Selkoe, 2007). It was shown that these oligomers, from both natural and synthetic source can mediate specific synaptotoxic effects on glutamatergic synapses through NMDA receptors. Subunit composition as well as localization of the NMDA receptors seems to have an influence on the effects of Aβ (Li et al., 2011). These processes are reversible and together with data on the physiological function of the peptide (Cárdenas-Aguayo et al., 2012), this gives further evidence to the fact that Aβ mediated synaptotoxicity is an early phenomena of the disease. Still, the mechanisms are not identified yet, and different pathways of Aβ action are reported (Benilova and De Strooper, 2013). Currently, consistent results and reproducible studies are hampered by differences in Aβ preparations and their composition (Benilova et al., 2012), as different species mediate different effects through different mechanisms (Ladiwala et al., 2012).

1.3 Human induced pluripotent stem cells

Since 2006, the generation of stem cells out of any somatic cell of mice is possible by introduction of only four factors: Oct3/4, Sox2, c-Myc, and Klf4 (Takahashi & Yamanaka, 2006). One year later, this was shown to work with human cells, too (Takahashi et al., 2007). The resulting cells have stem cell like properties and can theoretically be differentiated into any other cell type, hence they were named induced pluripotent stem (iPS) cells. The

possibility to create iPSCs from human somatic cells overcomes ethical constraints about the use of human embryonic stem (ES) cells. As they can be created from any specific individual, amplification and differentiation into somatic cells of any type gives new possibilities for different fields of biology and medicine, especially for translational approaches.

1.3.1 Goals and aims of iPSC technology

First, the replacement and support of diseased tissue in patients is a goal of the iPSC technique (Daley and Scadden, 2008; Figure 7A). Up to now, transplantation of tissue is always a risk because of immune responses and rejection of foreign tissue, making the treatment with immunosuppressive drugs necessary. This could be overcome, when tissues and cells have the same genetic and immunological identity as the receiving patient. Here, two options are possible. Organs could be grown outside the human body and then transplanted or cells with the potential to replace tissue are just injected into the site of interest. While the first method raises ethical problems, the latter has the risk of unpredictability due to migration and proliferation of injected cells. However, as another point is the accessibility and individuality of tissue which has to be renewed. Some organs like the brain cannot be replaced as a whole. Furthermore, access to deeper areas is not possible without damaging surrounding tissue. Limiting this damage to a small injury by only injecting the needed cells which are then able to integrate into the surrounding tissue is a promising option. Nonetheless, a major risk with transplantation of these cells is the possible introduction of stem or progenitor cells into the target tissue, which might create cancer due to unlimited proliferation or other side effects due to undirected differentiation.

The second use of the iPSC technique is drug screening and development and fine tuning of individualized medicine (Inoue et al., 2014; Figure 7B). Individual variations in genetic background and development of drugs from animal models sometimes hamper the success of clinical drug trials, thus render cost intensive research obsolete and make clinical trials risky (Schnabel, 2008). With the iPSC technique, drugs could be screened in human live tissue with genuine genetic background without harming patients or animals. However, this option still has the drawback of every *in vitro* system, as it is simplifying the *in vivo* situation.

Third, iPSCs can be used to gain new insights into diseases, as research on human tissue is limited by ethical constraints and availability (Nityanandam and Baldwin, 2015; Figure 7C). The development of new sophisticated human disease models with the advantage of a genuine

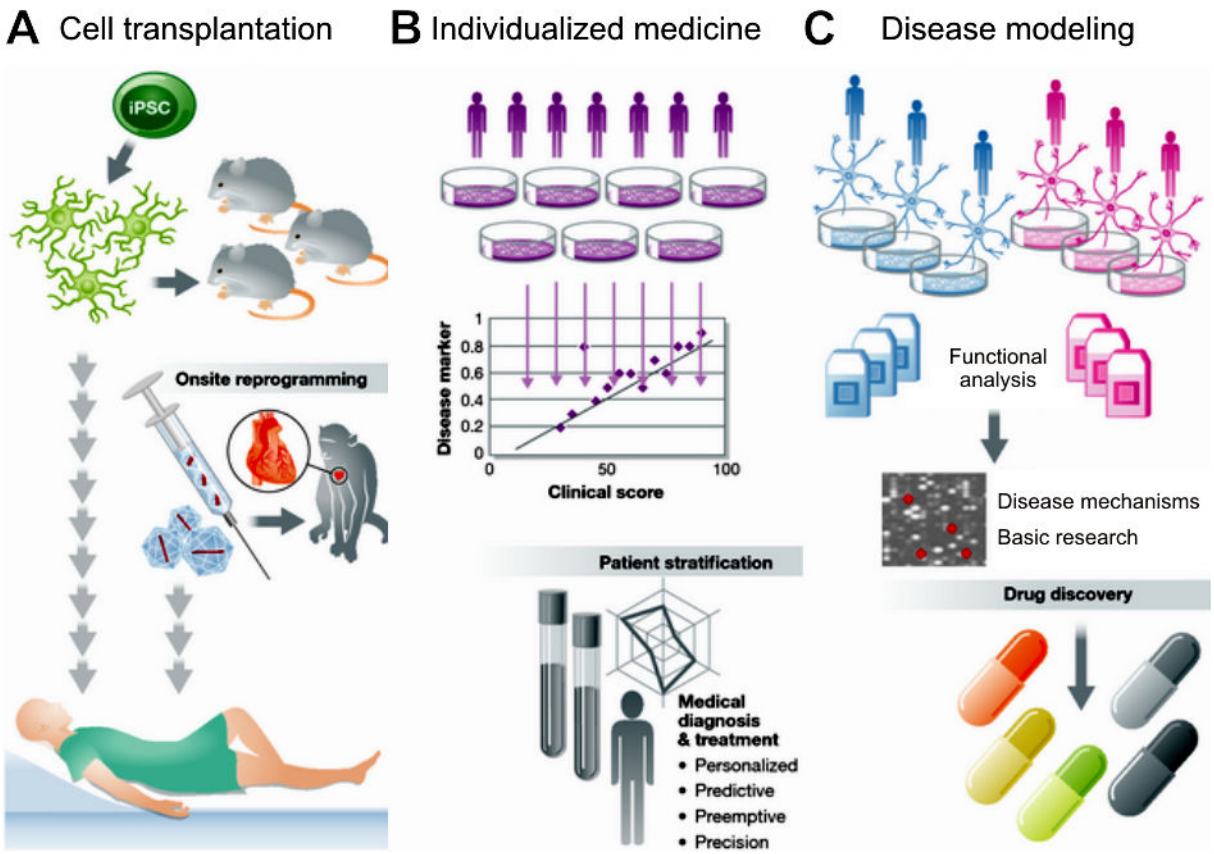

Figure 7: Goals of the human iPSC technology.
Modified after Inoue et al. (2014). **A:** Induced pluripotent stem cells (iPSC) can be differentiated into cells that support or replace diseased tissue in patients after transplantation. Risks have to be estimated in animals before. Another approach is the direct reprogramming of cells in diseased tissue for regeneration. **B:** Patient specific tissue can be used for drug screening before the treatment to verify efficiency of the drug. Also, it might help in diagnosis. **C:** Disease modeling with human disease specific cells can help to find disease mechanisms and new insights for basic research. Finally, new drugs can be discovered and tested.

genetic background will give and is already giving new insight into disease mechanisms, opening new horizons for therapies and drugs. Finally, basic research can also benefit from these techniques, while new insights into human biology are gained.

For neuroscience, the advent of the iPSC technique is of outstanding interest, as neurodegenerative diseases get more and more important in an aging society and both, therapeutic and mechanistic development is hampered by the lack of proper disease models. Research on neurodegenerative diseases is limited by several constraints, starting from the sporadic nature of some diseases, late onset of symptoms, lack of accessibility of brain tissue and availability of bio markers. Finally the inability of neurons to regenerate and proliferate makes diseases which are marked by neuronal loss excellent candidates for the transplantation of healthy cells.

1.3.2 Neural differentiation of human iPSCs

Up to now, to obtain human neurons from iPSCs for disease modeling and therapy, the *in vitro* differentiation usually mimics the natural differentiation through a neuronal precursor state (neuronal progenitor cells, NPC), which is followed by first neuronal and then glial differentiation. To some extent, differentiation can be sped up by the use of so called small molecules which interfere with cell signaling pathways that are involved in stem cell maintenance and proliferation (Choi and Nam, 2012). For example, PD0325901 (PD) is used to inhibit the MEK1/2 (mitogen-activated protein kinase kinase 1/2) pathway, which mediates the regulation of growth and differentiation in response to extracellular stimulants such as mitogens and hormones (Spicer, 2008). PD was first created as an advanced drug for the inhibition of tumor growth with a half maximal inhibition at 1 nM against activated MEK1 and MEK2 (Barrett et al., 2002) and can thus be used as a potent inhibitor of stem cell fate. Another small molecule, dorsomorphin (DM) is inhibiting the BMP (bone morphogenic protein) pathway by reduction of SMAD1/5/8 phosphorylation through BMP type 1 receptors ALK2, ALK3, and ALK6 (Paul et al., 2008). DM was shown to support differentiation towards a neuronal fate (Morizane at al., 2010).

Maturation of the resulting neuronal cultures takes long time as it seems to resemble the natural human development (Payne et al., 2015). Neuronal maturity has two factors, first of all, the structural basis has to be met, that is neurons have to grow dendrites, axons and synaptic connections. Second, it is necessary to gain functionality in form of electrical and chemical signal conduction, with the latter involving the whole network of neurons and makes connectivity an important factor. As synaptic developmental and plasticity processes are very dynamic, they are not easy to foresee, especially in an artificial *in vitro* culture system. Thus, basic principles of neural functions are widely used to assess neuronal maturity, regarding neurons that express these functions as mature which is crucial for neurodegenerative disease modeling as most of these diseases occur in the adult brain only.

1.4 Aims of the study

Aims of the study were to develop and functionally characterize a human neuronal culture system with high maturity. Furthermore, the effect of glial cells on the functional maturity of this culture system was of interest, as well as the usability of this culture as an AD model by the use of synthetic amyloid-β. In addition, the activity dependence of naturally secreted amyloid-β mediated synaptotoxicity was assessed in mouse hippocampal cultures.

Since Takahashi & Yamanaka (2006) described the generation of pluripotent stem cells out of any somatic cell from mice and Takahashi el al. (2007) showed that iPSCs can also be generated from human cells in this way, a lot of progress has been made on the differentiation of human neuronal cells. Now, the technique is regarded as a "game changer for future medicine" (Inoue et al., 2014). Nonetheless, the definition, characterization and purity of human neurons is still an issue along with maturity, which is crucial in models of neurodegenerative diseases because of their late onset nature (Payne et al., 2015). To overcome these problems, a human neuronal culture system with high maturity has been developed in this study by permitting a non-neuronal subpopulation, the glial cells, to differentiate along with the neurons in the same preparation. The cellular composition of the culture was verified by immunostainings to identify neurons and glial cells. The advantage of having these intrinsic glial cells in the preparation is the homogenous identity of the whole culture, in contrast to co-cultures which use murine astrocytes as neuronal support (Odawara at al., 2014). Especially for disease modeling, a homogenous genetic background can be crucial. To achieve highly mature cultures, a long term cultivation procedure (> 8 weeks post immunopanning) was used in addition to the support by glial cells. To assess their maturity, in-depth analysis of neuronal function has been conducted using electrophysiology at a single cell level while dissecting subpopulations defined by morphology. Passive electrical properties as well as AP parameters and spike patterns were analyzed by current clamp experiments per subpopulation to gain insight into the major functionality of these neurons. Furthermore, Na^+ currents and synaptic transmission, other important factors for neuronal maturity, were addressed by voltage clamp experiments. To estimate the overall connectivity and integration of neurons into the network, a Ca^{2+} imaging method was established. By measuring synchronous network activity, this method should give insights into the general state of the human neuronal network and allow conclusions about its maturity. To verify that

human glia cells have a positive effect on maturity, all these characterization studies were conducted in comparison to a glia free preparation of similar neurons.

The second part of the project addressed AD, a neurodegenerative disease which creates symptoms like cognitive impairment, memory loss and personality change. The pathology of AD is defined by the massive loss of neurons in the cortex which is preceded by the deposition of amyloid-β into plaques and the formation of fibrillar tangles, consisting of tau protein. Both pathologies are regarded as hallmarks of AD and are thus studied intensively. While there are a lot of studies on synaptotoxic effects of Aβ, its mechanism is still not known, because it is not clear, which of the many aggregation states is causing the deleterious effects, if not plenty or all of them. In this study, a simple synthetic Aβ preparation has been developed for disease modeling in human iPSC derived neurons while using a new combination of native PAGE (polyacrylamid gel electrophoresis) and Western blot to characterize it. Synthetic Aβ should give more reproducible mixtures of aggregation states than naturally secreted forms, for example 7PA2 supernatant preparation which is often used because of its relation to FAD and its efficiency (Podlisny et al. 1995; Nieweg at al. 2015). The Aβ preparation was then tested on human neurons for its suitability as a disease model. Na^+ currents and synaptic transmission were assessed by electrophysiology to verify effects on membrane and synaptotoxicity, respectively while excluding cytotoxic effects and cell death by a cell viability essay. In addition, the activity dependence of Aβ effects was analyzed by applying 7PA2 conditioned medium to mouse hippocampal neurons which were synaptically up-scaled before by TTX treatment.

2 Materials and methods

2.1 Buffers and reagents

2.1.1 Media supplements

ITS

Reagent	Distributor	Catalog no.	Concentration	Amount
DMEM/F-12	Invitrogen	31330-095	1×	90.2 ml
Insulin	Sigma	I1882	10 mg/ml	9.99 ml
Holo-transferrin	Calbiochem	616424	20 mg/ml	2.76 ml
Sodium-Selenite	Sigma	S5261	1.4 mg/ml	51.5 µl

N2

Reagent	Distributor	Catalog no.	Concentration	Amount
DMEM/F-12	Biochrom	FG4815	1×	79 ml
Insulin	Sigma	I1882	10 mg/ml	20 ml
Holo-transferrin	Calbiochem	616424	20 mg/ml	20 ml
BSA	Sigma	A4919	10 mg/ml	40 ml
Putrescine	Sigma	P5780	161 mg/ml	900 µl
Sodium-Selenite	Sigma	S5261	0.52 mg/ml	80 µl
Progesteron	Sigma	P8783	0.62 mg/ml	80 µl

NS21

NS21 was prepared as described in Chen et al. (2008) at a 50× concentration.

Sato

Reagent	Distributor	Catalog no.	Concentration	Amount
NB	Invitrogen	21103	1×	33.8 ml
BSA	Sigma	A4919	20 mg/ml	20 ml
Insulin	Sigma	I1882	10 mg/ml	10 ml
Holo-transferrin	Calbiochem	616424	20 mg/ml	10 ml
Putrescine	Sigma	P5780	161 mg/ml	400 µl
Sodium-Selenite	Sigma	S5261	0.4 mg/ml	400 µl
Progesteron	Sigma	P8783	0.62 mg/ml	400 µl

2.1.2 Media formulations

E8

Reagent	Distributor	Catalog no.	Concentration	Amount
DMEM/F-12	Invitrogen	31330-095	1×	49 ml
ITS			50×	1 ml
P/S	Invitrogen	15140-122	100×	500 µl
$NaHCO_3$	Sigma	S3817	34.3 mg/ml	500 µl
bFGF	PeproTech	100-18B	20 µg/ml	250 µl
TGFβ	PeproTech	100-21	2 µg/ml	50 µl
Ascorbic acid	Sigma	A8960	221 mM	50 µl

N2B27

Reagent	Distributor	Catalog no.	Concentration	Amount
DMEM/F-12	Biochrom	FG4815	1×	250 ml
NB	Invitrogen	21103	1×	250 ml
Pen Strep	Invitrogen	15140-122	100×	5 ml
B27 -RA	Invitrogen	17504-036	50×	5 ml
N2			50×	5 ml
Glutamax	Invitrogen	35050-038	100×	2.5 ml
β-mercaptoethanol	Invitrogen	31350-010	50 mM	1 ml
Heparine	Sigma	H3149	10 mg/ml	150 µl

NBNS21S

Reagent	Distributor	Catalog no.	Concentration	Amount
NB	Invitrogen	21103	1×	50 ml
NS21*			50×	1 ml
Sato			50×	1 ml
Pen Strep	Invitrogen	15140-122	100×	500 µl
Glutamax	Invitrogen	35050	100×	500 µl
Sodium-Pyruvate	Invitrogen	11360	100 mM	500 µl
BDNF	Preprotech	450-02	30 µg/ml	50 µl

*NS21 was filtered with 20 ml of NB at 0.2 µm before adding the other reagents.

NBNS21

Reagent	Distributor	Catalog no.	Concentration	Amount
NB	Invitrogen	21103	1×	50 ml
NS21*			50×	1 ml
Pen Strep	Invitrogen	15140-122	100×	500 µl
Glutamax	Invitrogen	35050-038	100×	500 µl

*NS21 was filtered with 20 ml of NB at 0.2 µm before adding the other reagents.

Preparation medium

Reagent	Distributor	Catalog no.	Concentration	Amount
BME	Invitrogen	41010-026	1×	45 ml
FBS	Invitrogen	10500-064	100%	5 ml
Pen Strep	Invitrogen	15140-122	100×	500 µl
ITS	Invitrogen	51300-044	100×	500 µl
Glutamax	Invitrogen	35050-038	100×	500 µl
Glucose	Merck	1083371000	40%	300 µl

CHO medium

Reagent	Distributor	Catalog no.	Concentration	Amount
D-MEM	Invitrogen	61965-026	1×	500 ml
FBS	Invitrogen	10500-064	100%	50 ml
Sodium-Pyruvate	Invitrogen	11360	100 mM	5 ml
Pen Strep	Invitrogen	15140-122	100×	5 ml

Additional cell culture reagents

Reagent	Distributor	Catalog no.	Concentration
Ara-C	Sigma	C-6645	2.5 mM
DMSO	Sigma	D4540	100%
DNAse	Sigma	DN25	
Dorsomorphine	Tocris	3093	10 mM
Laminin	Sigma	L2020	1 mg/ml
Matrigel	BD	354277	83.3 µg/ml
PD 0325901	Tocris	4192	5 mM
Poly-L-Ornithine	Sigma	P3655	50 mg/ml
Serum replacement			100%
Trypsin	Invitrogen	25050-014	0.25%

2.1.3 Buffers for immunopanning and re-dissociation

Immunopanning reagents

Reagent	Distributor	Catalog no.	Concentration
Accutase	Sigma	A-6964	
DPBS, -Ca^{2+}/Mg^{2+}	Pan Biotech	P0436500	1×

DPBS, +glucose/pyruvate

Reagent	Distributor	Catalog no.	Concentration	Amount
DPBS, -Ca^{2+}, -Mg^{2+}	Pan Biotech	P0436500	1×	500 ml
Sodium-pyruvate	Invitrogen	11360	100 mM	1.63 ml
Glucose	Merck	1083371000	33.3%	1.5 ml

1% BSA

Reagent	Distributor	Catalog no.	Concentration	Amount
DPBS, +glucose/pyruvate			1×	3.5 ml
BSA	Invitrogen	15260-037	7.5%	533 µl

0.2% BSA

Reagent	Distributor	Catalog no.	Concentration	Amount
DPBS, +glucose/pyruvate			1×	48.7 ml
BSA	Invitrogen	15260-037	7.5%	1.33 ml

0.02% BSA

Reagent	Concentration	Amount
DPBS, +glucose/pyruvate	1×	45 ml
BSA	0.2%	5 ml

50mM Tris/HCl, pH 9.5

6.06 g Tris in 1 l ddH_2O, set pH to 9.5 with HCl (Merck 1.00316.1000).

Blocking antibody mix

Reagent	Distributor	Catalog no.	Concentration	Amount
Tris/HCl, pH 9.5	Sigma	T6066	50 mM	10 ml
Goat anti mouse IgG + IgM	Jackson labs	115-005-068	1.8 mg/ml	45 µl

Primary antibody mix

Reagent	Distributor	Catalog no.	Concentration	Amount
BSA	Invitrogen	15260-037	0.2%	5.4 ml
NCAM antibody	DSHB	VIN-IS-53	19 µg/ml	1.6 ml
Pen Strep	Invitrogen	15140-122	100×	70 µl

Filtered at 0.2 µm.

2.1.4 Immunocytochemistry buffers and antibodies

Immunocytochemistry reagents

Reagent	Distributor	Catalog no.	Concentration
DAPI	Sigma	D9542	1 mg/ml
Fluor safe reagent	Calbiochem	345789	
Normal goat serum	Invitrogen	16210064	30%
PFA	Polysciences	18814	4%
Tween	Serva	37470	0,1%

Permeabilization buffer

Reagent	Distributor	Catalog no.	Concentration	Amount
DPBS, -Ca^{2+}/Mg^{2+}	Pan Biotech	P0436500	1×	5.4 ml
Glycine	Sigma	50046-1250G	1 M	600 µl
Triton X100	Sigma	X100-100ML	10%	150 µl

Antibody buffer

Reagent	Distributor	Catalog no.	Concentration	Amount
DPBS, -Ca^{2+}, -Mg^{2+}	Pan Biotech	P0436500	1×	4.8 ml
BSA	Sigma	A3059	20%	600 µl
Sucrose	Merck	1076871000	50%	600 µl

Primary antibodies

Reagent	Distributor	Catalog no.	Concentration
Chicken anti MAP2	Abcam	AB92434	1:2000
Rabbit anti GFAP	Dako	Z0334	1:2000
Mouse anti GAD67	Millipore	MAB5406	1:500

Secondary antibodies

Reagent	Distributor	Catalog no.	Concentration
Alexa 488 goat anti chicken	Invitrogen	A11034	1:1000
Alexa 555 goat anti rabbit	Invitrogen	A21429	1:1000
Alexa 555 goat anti mouse	Invitrogen	A21424	1:1000

2.1.5 Calcium imaging buffers & reagents

Calcium imaging reagents

Reagent	Distributor	Catalog no.	Concentration
Fluo-4 AM	Invitrogen	F-1420	5 µM

Basal imaging buffer (Mg^{2+} free)

Reagent	Distributor	Catalog no.	Concentration
NaCl	Roth	9265.1	140 mM
Glucose	Merck	1083371000	20 mM
HEPES	Applichem	A1069.0100	15 mM
KCl	Niedel-de-Haën	31248	5 mM
$CaCl_2$	Niedel-de-Haën	12074	1.5 mM
NaH_2PO_4	Sigma	S8282-500G	1.25 mM

Reagents were dissolved in and filled up with ddH_2O to 500 ml. The pH was set to 7.4 with NaOH (1 M, Aldrich 22.146-5) and the solution was filtered at 0.2 µm. $CaCl_2$ (1 M, Niedel-de-Haën 12074) was added to a volume of 50 ml basal buffer as needed to achieve concentrations of 0.5, 1, 1.5, 2, 5 and 10 mM. Default concentration was 1.5 mM.

Mg^{2+} imaging buffer

37.5 µl of $MgCl_2$ (1M, J.T. Baker 163) was added to a volume of 50 ml basal buffer to achieve a final concentration of 0.75 mM.

2.1.6 Electrophysiology buffers and inhibitors

Standard extracellular solution

Reagent	Distributor	Catalog no.	Concentration
NaCl	Roth	9265.1	130 mM
HEPES	Applichem	A1069.0100	20 mM
KCl	Niedel-de-Haën	31248	5 mM
$CaCl_2$	Niedel-de-Haën	12074	2.5 mM
$MgCl_2$	J.T. Baker	163	1 mM

Reagents were dissolved in and filled up with ddH_2O to 500 ml. The pH was set to 7.3 with NaOH (1 M, Aldrich 22.146-5) and the solution was filtered at 0.2 µm.

Standard intracellular solution

Reagent	Distributor	Catalog no.	Concentration
KCl	Niedel-de-Haën	31248	110 mM
KOH	J.T. Baker	0385	20 mM
HEPES	Applichem	A1069.0100	20 mM
EGTA/Triplex VI	Merck	1.08435.0025	10 mM
$CaCl_2$	Niedel-de-Haën	12074	250 µM

Reagents were dissolved in and filled up with ddH_2O to 50 ml, starting with KOH and EGTA/Triplex VI.. The pH was set to 7.3 with KOH (1 M, J.T. Baker 0385) and the solution was filtered at 0.2 µm.

Alexa Fluor 488 intracellular solution (5:4)

Reagent	Distributor	Catalog no.	Concentration
KCl	Niedel-de-Haën	31248	138 mM
KOH	J.T. Baker	0385	25 mM
HEPES	Applichem	A1069.0100	25 mM
EGTA/Triplex VI	Merck	1.08435.0025	12.5 mM
$CaCl_2$	Niedel-de-Haën	12074	313 µM

Reagents were dissolved in and filled up with ddH_2O to 50 ml. The pH was set to 7.3 with HCl (Merck 1.00316.1000) and the solution filtered at 0.2 µm. 100 µl Alexa Fluor 488 (2 mM, Invitrogen A-10436) was added to 400 µl of 5:4 intracellular solution to achieve final concentrations of ions equal to standard intracellular solution and a concentration of 400 µM for Alexa Fluor 488.

Extracellular solution for sodium ion current measurements

Reagent	Distributor	Catalog no.	Concentration
NaCl	Roth	9265.1	130 mM
HEPES	Applichem	A1069.0100	20 mM
CsCl	Sigma	289329	5 mM
$CaCl_2$	Niedel-de-Haën	12074	2.5 mM
$MgCl_2$	J.T. Baker	163	1 mM

Reagents were dissolved in and filled up with ddH_2O to 500 ml. The pH was set to 7.3 with NaOH (1 M, Aldrich 22.146-5) and the solution was filtered at 0.2 µm.

Intracellular solution for sodium ion current measurements

Reagent	Distributor	Catalog no.	Concentration
CsCl	Sigma	289329	110 mM
KOH	J.T. Baker	0385	20 mM
HEPES	Applichem	A1069.0100	20 mM
EGTA/Triplex VI	Merck	1.08435.0025	10 mM
$CaCl_2$	Niedel-de-Haën	12074	250 µM

Reagents were dissolved in and filled up with ddH_2O to 50 ml, starting with KOH and EGTA/Triplex VI. The pH was set to 7.3 with KOH (1 M, J.T. Baker 0385) and the solution was filtered at 0.2 µm.

Extracellular solution for mouse neurons

Reagent	Distributor	Catalog no.	Concentration
NaCl	Roth	9265.1	130 mM
HEPES	Applichem	A1069.0100	20 mM
KCl	Niedel-de-Haën	31248	5 mM
$MgCl_2$	J.T. Baker	163	1 mM
$CaCl_2$	Niedel-de-Haën	12074	250 µM

Reagents were dissolved in and filled up with ddH_2O to 500 ml. The pH was set to 7.3 with NaOH (1 M, Aldrich 22.146-5) and the solution was filtered at 0.2 µm.

Inhibitors

Reagent	Distributor	Catalog no.	Concentration
AP5	Tocris	0105	5 µM
Gabazine	Tocris	1262	10 µM
NBQX	Tocris	1044	10 µM
TTX	Tocris	1078	1 µM

2.1.7 Native PAGE and Western blot buffers and antibodies

3× native gel buffer

90.85 g Tris (Roth 4855.2) was dissolved in and filled up with ddH_2O to 250 ml. The pH was set to 8.45 with HCl (Merck 1.00316.1000).

10% gel

Reagent	Distributor	Catalog no.	Concentration	Amount
Polyacrylamid	Biorad	161-0154	30%	2.67 ml
native gel buffer			3×	2.67 ml
ddH_2O			100%	1.93 ml
Glycerol	Sigma	G8773	100%	640 µl
APS	Applichem	A0834.0250	10%	80 µl
Temed	Applichem	A1148.0100	100%	8 µl

Tris-Hcl, pH 6.8

12.11 g Tris (Roth 4855.2) was dissolved in and filled up with ddH_2O to 100 ml. The pH was set to 6.8 with HCl (Merck 1.00316.1000).

4× laemmli buffer

Reagent	Distributor	Catalog no.	Concentration	Amount
Glycerol	Sigma	G8773	100%	20.0 ml
ddH_2O			100%	17.4 ml
Tris-Hcl, pH 6.8			1 M	12.6 ml
Bromphenol blue	Aldrich	11439-1	669.98 g/mol	20 mg

10× cathode buffer

Reagent	Distributor	Catalog no.	Amount
Tricine	Roth	6977.2	179.2 g
Tris	Roth	4855.2	121.1 g

5× anode buffer

121.1 g Tris was dissolved in and filled up with ddH2O to 1 l. The pH was set to 8.9 with HCl (Merck 1.00316.1000).

10× transfer buffer

Reagent	Distributor	Catalog no.	Amount
Glycine	Sigma	50046-1250G	144.16 g
Tris	Roth	4855.2	30.28 g

PBS

Tablets (Gibco 18912-014) were dissolved in ddH_2O following manufacturers manual.

50% PBS

250 ml PBS was diluted with the same volume of ddH_2O.

10x TBS

Reagent	Distributor	Catalog no.	Concentration	Amount
NaCl	Roth	9265.1	58.44 g/mol	80.0 g
Tris	Roth	4855.2		24.2 g

Reagents were dissolved in and filled up with ddH_2O to 1 l. The pH was set to 7.6 with HCl (Merck 1.00316.1000).

TBS-T

Reagent	Distributor	Catalog no.	Concentration	Amount
TBS			10x	100 ml
Tween 20	Serva	37470	100%	1 ml

Reagents were dissolved in and filled up with ddH_2O to 1 l.

5% milk in TBS-T

5 g milk powder (Roth T145.3) was dissolved in and filled up with TBS-T to 100 ml.

Antibodies

Reagent	Distributor	Catalog no.	Concentration
Mouse 4G8	Covance	SIG 39220-200	1:2000
IgG-HRP goat anti mouse	Santa Cruz Biotech.	SC-2005	1:20000

Antibodies were dissolved in 5% milk in TBS-T right before usage.

Chemiluminescence Kit

Chemiluminescence kit (ECL) was bought from GE Healthcare (RPN2232).

2.1.8 Cell viability assay reagents

Reagent	Distributor	Catalog no.	Concentration
Ethidium homodimer	Invitrogen	E1169	2 µM
Calcein green AM	Calbiochem	206700	2 µM
Hoechst 33342	Calbiochem	382065	10 µg/ml

2.2 Cell culture

2.2.1 Thawing and maintenance of human iPSCs

Integration free human iPSCs (iPS-DF6-9-9T.B, WiCell) were kept frozen in cryotubes (Thermo Scientific 377267) containing E8 with 10% DMSO (dimethyl sulfoxide) in a liquid nitrogen tank. Cells were thawed 37°C for a few minutes. Freezing medium was then diluted 1:1 with serum replacement (Invitrogen 10828) and 10 ml of DMEM/F-12 before centrifugation at 2000 rpm for 3 min. The supernatant was removed and the resuspended pellet was plated onto a 6-well plate (Sarstedt 83.3920). The plate was previously coated for 1h at room temperature with matrigel.

Medium was changed 6 times per week and usually 1 well was splitted onto matrigel coated 6 well plate on a weekly basis when density reached around 50% confluency. Sporadic differentiation was monitored and differentiated cells were removed using a vacuum pump with a glass Pasteur pipette (Brand 747715) when necessary.

For splitting, cells were washed and incubated for 10 minutes with DPBS without calcium and magnesium ions (DPBS-/-) before scraping them with a cell spatula (Biochrom 99010). Detached iPSCs were collected and centrifuged before dilution and seeding into fresh 6-well plates. The remaining wells were used for neural differentiation.

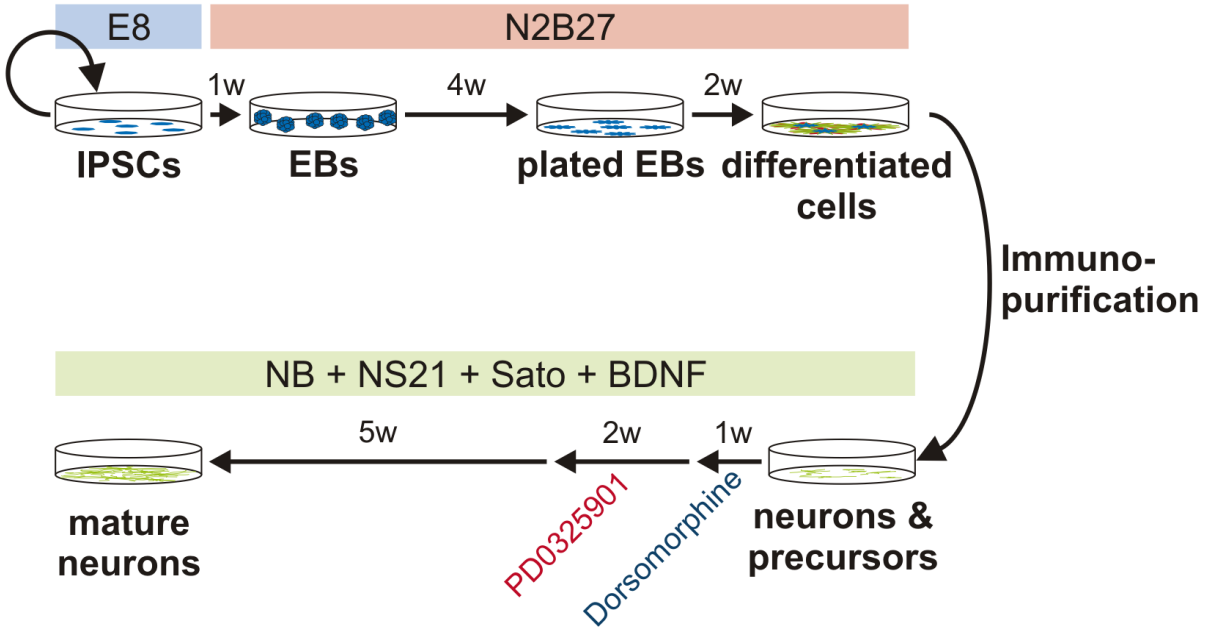

Figure 8: Neural differentiation protocol.
Blue, red and green bars represent used media, time between steps is indicated in w = weeks.

2.2.2 Neural differentiation of human iPSCs

iPSCs were pre-treated with N2B27 for 6 days (6 d) before detachment of the cultures and subsequent embryoid body (EB) generation (Figure 8). The medium was changed every second day during pretreatment. Detachment of cultures was achieved the same way as for splitting with DPBS-/- for 5 min, subsequent centrifugation and dilution.

Resulting cells were transferred to T-25 flasks (Sarstedt 83.1810.002) containing fresh N2B27 and kept in floating state for four weeks. Medium was changed after 1, 3, 5 and 7 d. After that, medium was changed on a weekly basis. During that time, EBs were formed as evident from the presence of big round structures.

After four weeks, EBs were plated onto a 100 mm culture dish (Sarstedt 83.1802) containing fresh N2B27 and medium was changed weekly. After 2 weeks, most cells were differentiated and processes and cells extended from the plated EBs.

2.2.3 Immunopurification of immature human neurons

To select neurons and neuronal precursors out of the inhomogeniously differentiated EBs, an immunopurifiaction procedure (immunopanning) was applied.

Plated EBs with clearly visible neurite outgrowth were selected with a 1000 ml plastic pipette tip and collected into a 15 ml tube (Greiner 188271). Cells were centrifuged for 2 min at

1100 rpm and the supernatant was replaced by Accutase. Digestion was done in a waterbath at 37°C for 20 min while tube was shaken several times in between. Again, the solution was centrifuged at 1100 rpm for 2 min.

The supernatant was replaced by 0.2% BSA and cells were dissociated by slow trituration with plastic pipette tips of decreasing size. Centrifugation at 400 rpm for 2 min in between ensured that dissociated cells were saved from additional mechanical stress by collecting the supernatant that contained the single cells. After eight steps of dissociation, the collected single cell suspension was centrifuged at 900 rpm for 10 min to harvest the cells in the pellet.

The pellet was resuspended in 0.02% BSA and distributed onto panning plates which were prepared from bacterial culture dishes (BD Falcon 351029). They were pre-incubated at 4°C over night with goat anti mouse IgG and IgM in 50mM Tris/HCl, pH 9.5. Panning plates were subsequently washed with DPBS-/- and incubated with NCAM (neuronal cell adhesion molecule) antibody solution over night at 4°C. On the day of panning, the antibody solution was removed, plates washed with DPBS-/- and incubated with 0.2% BSA. NCAM antibody solution was reused for up to ten immunopannings. Before putting the single cell suspension onto the plates, 0.2% BSA was exchanged with 0.02% BSA. Single cells were incubated on panning plates for 8 min and the supernatant was replaced with DPBS-/- for all plates before extensive washing of plates with 50 ml DPBS-/- each. Bound cells were removed by flushing the plates with a total volume of 7 ml 0.02% BSA through a 1000 µl plastic pipette tip, covering all areas of the plate. Collected cells were mixed and counted before centrifugation at 900 rpm for 10 min.

2.2.4 Glial cell enriched cultures

To obtain glial cell containing (glia+) cultures, the pellet from the immunopanning was resuspended in NBNS21S to a concentration of 5000 cells per µl. 8 µl of cell suspension was plated on each glass coverslip (Assistant 1001/12). Coverslips were previously coated with PO and laminin in 35 mm dishes (BD Falcon 353001). After 1h at 37°C, cells attached to the surface and 2 ml of NBNS21S with BDNF and 3 µM dorsomorphine (DM) was added. After 6d, DM was removed and media was replaced by NBNS21 with laminin and 1 µM PD0325901 (PD). PD treatment was refreshed after 7d, included in a half medium change. After another 7d, PD treatment was stopped and medium was replaced with fresh NBNS21S with laminin. From then, half medium was changed on a weekly basis, while adding laminin

and water (Sigma W3500) to compensate for evaporation. Cultures were used at 8 to 10 weeks post immunopanning.

2.2.5 Low glia cultures and re-dissociation

To remove glial cells out of the culture (glia-), the pellet from immunopanning was resuspended in NBNS21S to a concentration of 600 to 2000 cells/µl and plated in a volume of 500 µl onto 12-well plates (Sarstedt 83.3921). Coverslips were previously coated with PO and laminin. After 1 h at 37°C, 500 µl fresh NBNS21S with DNA synthesis inhibitor Ara-C (arabinofuranosyl cytidine) was added to kill proliferating cells. After 5 d, Ara-C treatment was stopped by replacement of media with fresh NBNS21 with laminin.

Re-dissociation was done 4 d after Ara-C treatment. Before adding Accutase, cells were washed with DPBS with calcium and magnesium ions. Digestion was done at 37°C and 5% CO_2 for 15 min. Subsequent shaking and flushing with 1% BSA ensured detachment of all the cells and the supernatant was collected. Cell suspension was centrifuged at 1100 rpm for 5 min and the resulting pellet was dissociated in 200 µl BSA (0.2%) using plastic pipette tips of decreasing sizes. After dilution of cells in 0.2% BSA, they were counted and centrifuged at 900 rpm for 10 min. The pellet was resuspended in NBNS21S to a concentration of 4000 cells/µl and 5µl cell suspension was plated onto each glass coverslip. Coverslips were previously coated with PO and laminin in 35 mm dishes. After 20 min, 2 ml of fresh NBNS21 was added. From then, half medium was changed on a weekly basis, while adding laminin and water (Sigma W3500) to compensate for evaporation. Cultures were used at 8 to 10 weeks post immunopanning, except for Na^+ current experiments, where cells were treated with Aβ before redissociation and were measured 1 h after redissociation.

2.2.6 Mouse primary hippocampal neurons

Pregnant wildtype C57-Bl/6 mice were killed by CO_2 and subsequently decapitated. Embryos (E-18) were extracted and kept cool while removing the head and opening the skull. Before separation of the hippocampi, hemispheres were separated and meninges were removed. Hippocampi were cut to small pieces and subsequently treated with Trypsin and DNAse at 37°C for 5 min. After centrifugation, the pellet was washed, resuspended and dissociated in 300 µl preparation medium by slow trituration first through a 1 ml plastic pipette tip, then through a 20 µl plastic pipette tip. To remove remaining cell clumps, cell suspension was

centrifuged at 400 rpm for 1 min. The supernatant was then centrifuged at 900 rpm for 5 min and the pellet was resuspended in 2 ml preparation medium before counting the cells. Dilution was done with preparation medium to a concentration of 285.7 cells/µl and 70 µl of cell suspension was plated onto each glass coverslip. Coverslips were previously coated with PO in 35 mm dishes. After 1 h at 37°C, cells attached to the surface and 2 ml of NBNS21 was added per dish. Cells were used after 14d for treatment.

2.3 Immunocytochemistry

For immunostaining, coverslips with mature neurons were washed with PBS and fixed with 4% PFA for 13 min at room temperature. After washing with PBS, reactive aldehyde groups were blocked and cells were permeabilized in permeabilization buffer for 10 min. This and the following steps were all done at room temperature on a shaker set to low rpm. Before incubating the primary antibody solution, blocking was done with 30% NGS for 1h. Primary antibody solution was incubated for 1 h and subsequently washed with PBS-T before incubating secondary antibody solution for another 1 h. Then, cells were washed with PSB-T and treated for 10 min with DAPI (4',6-diamidino-2-phenylindole) to stain nuclei. DAPI was washed away first with PBS-T, then PBS and finally ddH2O. Coverslips were mounted using Fluor Safe Reagent, cured over night at room temperature and stored at 4°C until imaging. Staining was done either with MAP2 and GFAP or MAP2 and GAD67, both always co-stained with DAPI.

Imaging was done at an epifluorescence microscope (Zeiss Apotome.2) using the following filter sets.

Dye	Zeiss filter set	λ_{Ex}	λ_{Em}
DAPI	49 (DAPI)	365 nm	445 nm
Alexa Fluor 488	38 (EGFP)	470 nm	525 nm
Alexa Fluor 555	43 (Cy3)	545 nm	605 nm

For each dye, images from four different fields of view were taken with 20× Objective (Zeiss Plan-Apochromat 420650-9901) with constant exposure times from each coverslip and the ratio of positive somata per total DAPI nuclei was calculated. The mean of the four images was used for statistics, so that n represents the number of coverslips.

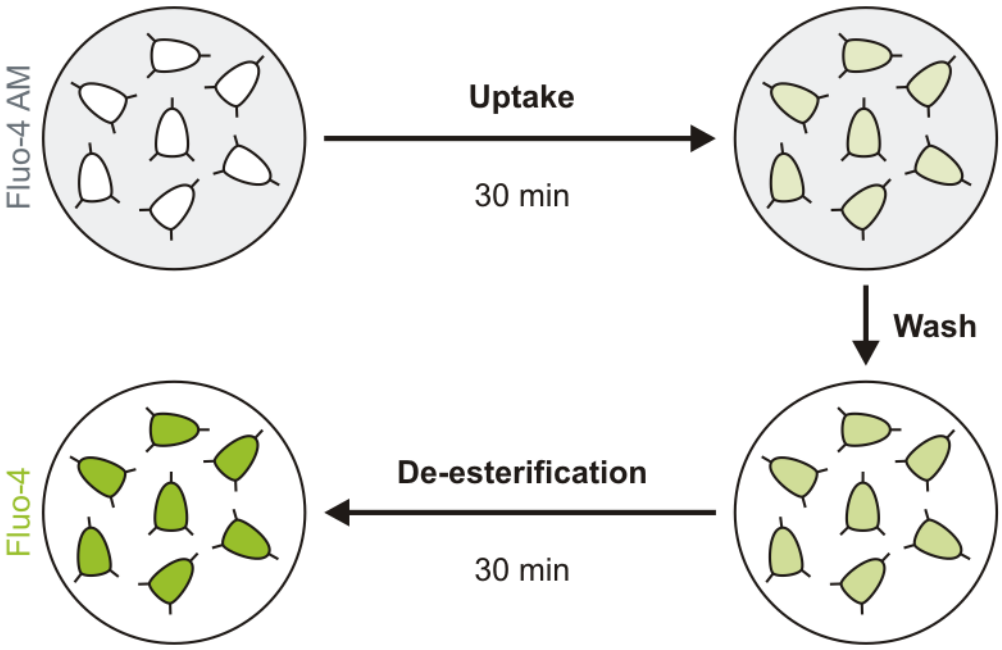

Figure 9: Fluo-4 AM loading procedure.
After uptake of Fluo-4 AM, the AM ester is shedded by cell innate esterases and Fluo-4 becomes fluorescent and Ca^{2+} sensitve.

2.4 Calcium imaging

Ca^{2+} imaging was done using Fluo-4 AM. Because of the acetoxymethyl (AM) ester, the dye is easily taken up by cells when added to the basal imaging buffer with Mg^{2+} and 1.5 mM Ca^{2+}. Cells were allowed to take up the dye for 30 min at 37°C and 5% CO2 before washing of excess dye to prevent further uptake and unspecific staining (Figure 9). Cells were incubated at 37°C and 5% CO_2 for another 30 min to allow de-esterification of the AM ester by cell innate esterases. The dye was then fluorescent and Ca^{2+} sensitive.

Imaging was done using an epifluorescence microscope (Zeiss Axiovert 200M) with Zeiss filter set 17 (FITC, λ_{Ex} 485 nm, λ_{Em} 540 nm) and 10× Objective (Zeiss Achrostigmat 440131). Images were acquired using Metavue Software (MDS Analytical Technologies) with a CCD camera (Photometrics Coolsnap ES^2) at 1 Hz for 5 min each. Exposure time was 500 ms at all times. Each coverslip was regarded as a single network and as independent n. For details of image analysis see results section.

2.5 Electrophysiology

Electrophysiological patch-clamp recordings were performed in whole cell mode using electrodes of approximately 8 MΩ made from glass capillaries (Science Products GB150ETF-

8P) that were pulled to fine tips using a horizontal programmable puller (Zeitz DMZ Universal Puller) and subsequently filled with intracellular solution. A chloridized sliver wire was used for current conversion between ion and electron conduction in the pipette electrode and in the bath electrode. Both were connected to the headstage (Axon Instruments CV203BU) of the amplifier (Axon Instruments Axopatch 200B). Preceding data recording onto hard drive via Clampex Software (Axon Instruments) at 20 kHz sample rate, signals were conditioned with a lowpass bessel filter (80dB/decade, 5 kHz cutoff frequency) and digitized by a Digidata 1322A (Axon Instruments). Analog signals were observed with an oscilloscope (Tektronix 2212) and pipette capacitance was compensated at all times.

Cells were located at phasecontrast with an Axiovert 35M micoscope (Zeiss) and approached with the electrode via Narishige micromanipulators (MHO-103) (Figure 10A). Positive pressure was applied until cell membrane showed a small indention. Then, pressure was released and an increase of resistance was observed, measured in voltage clamp mode as the current response to a 3 mV stimulation pulse (Figure 10B). To promote sealing, negative pressure was applied until the resistance increased to GΩ range and the pipette was clamped to -60 mV. To open the cell membrane, short pluses of negative pressure were applied with increasing intensity until capacitive transient artifacts increased, resembling the cell capacitance (Figure 10C).

2.5.1 Voltage clamp recordings

Recordings of miniature post synaptic currents (mPSC) were done at a holding potential of -60 mV and with tetrodotoxin (1 µM, TTX), a voltage dependent Na^+ channel blocker in the extracellular solution. To isolate AMPA receptor mediated currents, gabazine (10 µM) was added. To isolate $GABA_A$ (γ-aminobutyric acid) receptor mediated currents, NBQX (10 µM) was added. Currents were recorded for 5 min in gap free mode. mPSC frequencies and amplitudes were analyzed using MiniAnalysis Software (Synaptosoft), while pooling mPSC of the same cell. Thus, n is representing the individual cells.

Qualitative Na^+ current experiments were conducted with standard buffers at a holding potential of -60 mV. Cells were depolarized by voltage pulses increasing by 10 mV up to 40 mV.

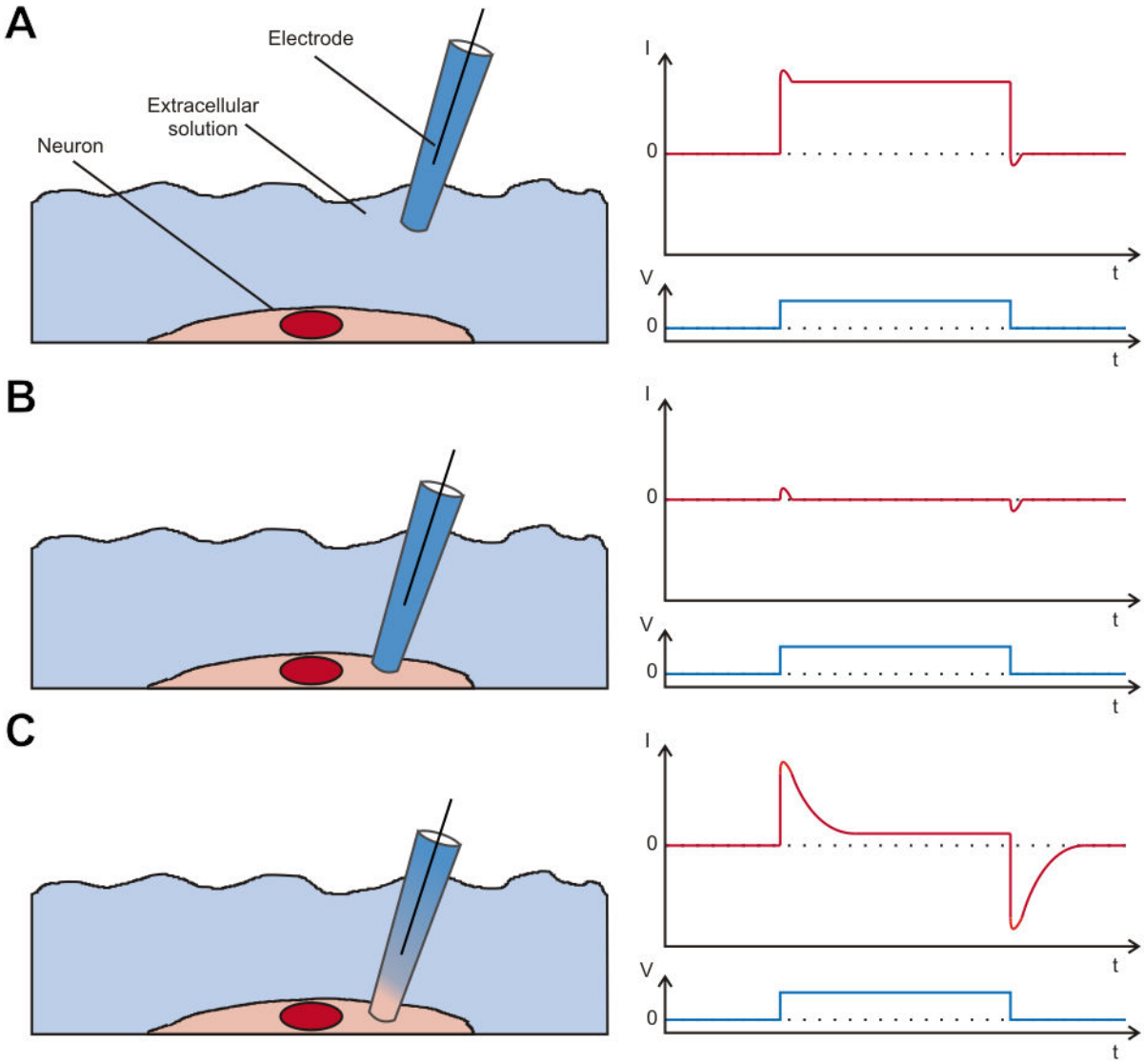

Figure 10: Whole cell patch-clamp technique.
Modified after .Walz et al. (2002). **A:** Immersion of electrode into extracellular solution and application of voltage pulse gives rise to a defined current; **B:** The current decreases while the cell membrane is approached and the resistance increases until reaching the range of several GΩ; **C:** Cell membrane is ruptured at the pipette tip by pulses of negative pressure, resulting in massive increase of capacitive currents. Red trace = measured current (I); blue trace = applied voltage (V) versus time.

In quantitative Na^+ current I/V experiments, young and freshly dissociated cells were used to achieve maximum control ofter the potential inside the cell. Holding was set to -80 mV and cells were depolarized by pulses of 40 ms, stepwise increasing by 5 mV from holding potential to +40 mV. Current traces were then analyzed by scaling a negative capacitive trace to the transient peaks and subtracting it to remove cell capacitance and leak current from traces. Negative peak current was then measured and normalized to each cells capacitance to obtain current density.

2.5.2 Current clamp recordings with Alexa Fluor 488

For current clamp experiments and simultaneous morphology analysis, intracellular solution was supplemented with Alexa Fluor 488 to stain the patched cells (Figure 11). Images were acquired at the patch clamp setup using a Cool $Snap_{CF}$ CCD camera (Photometrics) in combination with Zeiss filter set 13 (GFP, λ_{Ex} 470 nm, λ_{Em} 518 nm) and Metavue Software (MDS Analytical Technologies). The pipette was retracted before taking images to avoid spill over of fluorescence from the solution in the pipette that would otherwise mask morphology. Except for measuring membrane potential which was done in $I = 0$ mode, negative current was injected to hold the cells around -70 mV.

Analysis was done with Clampfit (Axon Intruments) on single cell level, which is represented by statistical n.

Resting membrane potentials were analyzed from 15 s long recordings by running a lowpass filter (8pole Bessel, 2 Hz cutoff frequency) to remove spikes and synaptic potentials and taking the mean of the last 13 s.

The potential response to 400 ms long current pulses of -20 pA was measured to assess passive cell parameters. 20 of these pulses were recorded and averaged per cell. For analysis, the rise of the average trace was fitted with an exponential decay function to obtain time constant τ and ΔV. ΔV was then used to calculate the resistance $R = \Delta V/I$. Capacitance was calculated from τ and R as $C = \tau/R$.

AP analysis was done on the first spike occurring upon depolarization from the same data which input/output relations were derived from (see next paragraph). Parameters were

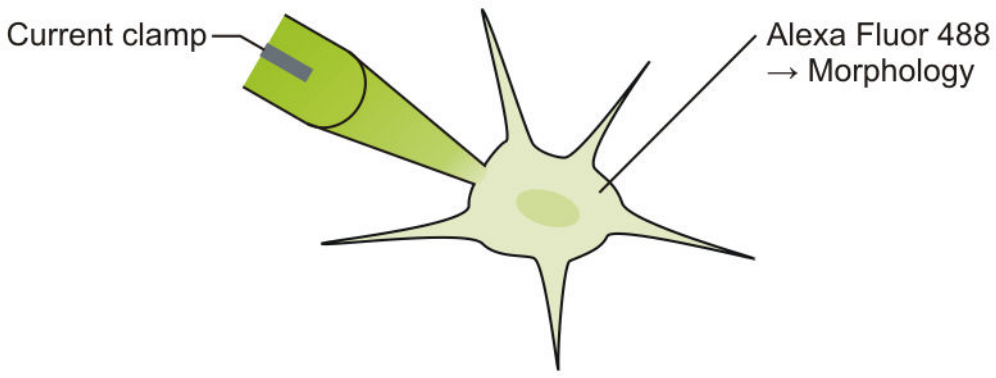

Figure 11: Current clamp recordings with Alexa Fluor 488.
Upon achieving whole cell configuration, Alexa Fluor 488 dye diffuses into soma and neurites of the patched cell making the morphology visible.

obtained by hand with the help of cursors in Clampfit. The amplitude was measured from threshold which was indicated by a fast change in slope (Figure 2). The half width is the duration of the AP at half maximum amplitude. The minimum after the AP was measured from threshold and was taken as afterhyperpolarization (AHP).

Input/output relations were measured by applying 900 ms long current steps of 10 pA from -50 to 240 pA. Resulting potentials were searched for APs by using the *threshold search* function of Clampfit after running a RC highpass filter (10 Hz cutoff frequency) over the traces to remove voltage offset. Detection threshold was set to 30 mV and the detected number of APs were converted into frequencies per injected current. To plot against potential, a lowpass bessel filter (8-pole, 2 Hz cutoff frequency) was run before measuring the plateau potential at the end of each depolarizing current pulse. Potentials and respective spike frequencies were binned into 10 mV bins, each cell only giving rise to one value per bin. When multiple potentials of the same cell fell into the same bin, the mean frequency of the corresponding traces was taken instead.

2.6 Amyloid-β

2.6.1 Synthetic amyloid-β

Synthetic amyloid-$\beta_{1\text{-}42}$ (Aβ, Bachem 4014447.0500) was dissolved to a nominal concentration of 10 µM in NBNS21S by shaking over night at room temperature. Before storage at -80°C, solution was centrifuged at 3250×g to remove most of the bigger unsolved and aggregated species. For treatment, Aβ was diluted to a nominal concentration of 1 µM in a mixture of fresh and conditioned NBNS21S before addition to the culture to resemble the weekly half medium change. As a vehicle condition, a same amount of fresh NBNS21S was treated exactly the same as the Aβ vial, starting from the dissolving procedure until centrifugation and storage at -80°C.

Monomer control Aβ (Biotrend BP0028) for Western blots was dissolved in HFIP (hexafluoro-2-propanol, Fluka 52517) to a concentration of 73,8 µM and stored at -80°C. Before usage, HFIP was evaporated under constant N_2 flow and remaining Aβ film was reconstituted with DMSO to a final concentration of 1 µM.

2.6.1.1 Native tris-tricine PAGE

Native PAGE was done using a Biorad Mini-PROTEAN system and a tris-tricine buffer system. Self-cast 10% gels in absence of SDS (sodium dodecyl sulfate) and β-mercaptoethanol were used. Samples were mixed with 4× native Laemmli buffer and the according amount of water to reach the same 1× buffer concentration in every sample. Into each of the 10 gel wells, 30 µl of sample was loaded. The gel was run at 40 V until the bromphenol blue marker front was concentrated in the bottom of the well. Then, 180 V was applied for 4 h. Constant cooling was provided during the whole procedure.

2.6.1.2 Western blot

Western blot was done using a Biorad Mini Trans-Blot system without methanol. Constant cooling was supplied during blotting from the native PAGE gel onto a 0.2 µm nitrocellulose membrane (Biostep 01-14-101) at 90 V for 1:40 h. After blotting, membrane was boiled in 50% PBS using a microwave for 10 min. The following incubation and washing steps were all done on shaker. The membrane was blocked in 5% milk at 4°C over night. On the next day, the 4G8 antibody solution was added and incubated over night at 4°C again. Before adding the secondary HRP conjugated antibody, membrane was washed three times with TBS-T for ten minutes. Antibody was then incubated at room temperature for 1:30 h and washed away three times with TBS-T and three times with ddH_2O. The membrane was kept in PBS at 4°C until detection.

Chemiluminescence was detected on a Fusion FX system in combination with a horseradish peroxidase activity detection kit (ECL). Substrate and enhancer were mixed right before detection and added to the membrane, which was embedded between two plastic sheets to ensure a thin surface of ECL covering the membrane. Imaging was executed immediately after addition of the ECL. Exposure times were varied in each experiment to receive optimal signal to noise ratio, usually 1 to 10 minutes were optimal.

2.6.2 Naturally secreted amyloid-β peptides

CHO cells carrying the V717F-Indiana mutation in the APP751 gene naturally secret different species of Aβ into the medium (Podlisny et al., 1995). The cells were kindly provided by the Department of Neuropathology. Approximately 10×10^5 cells were plated onto a 100 mm culture dish and kept in CHO medium until they were confluent. Medium was then changed

to NBNS21 and incubated for 3d. The supernatant (7PA2) was purified by centrifugation and filtration and kept at -80°C until usage. For treatment, 7PA2 was added directly to the cultures, fresh NBNS21 served as a control.

Mouse hippocampal neurons were treated with TTX or not 4 d before 7PA2 or vehicle was added for another 4 d.

2.7 Cell viability assay

To assess cell viability after Aβ treatment, live cells were triple stained by ethidium homodimer (EthD-1), calcein green AM and hoechst 33342 without fixation for 30 min at room temperature. Before and after staining, cells were washed two times with PBS. Imaging was done using an epifluorescence microscope (Zeiss Axiovert 200M) with 10× Objective (Zeiss Achrostigmat 440131). For filter sets used, please refer to the following table.

Dye	Zeiss filter set	λ_{Ex}	λ_{Em}
Hoechst 33342	49 (DAPI)	365 nm	445 nm
Calcein AM	17 (FITC)	485 nm	540 nm
EthD-1	43 (Cy3)	545 nm	605 nm

For each dye, images from four different fields of view were taken with constant exposure times from each coverslip. Live cells were determined by co-staining of hoechst and calcein, dead cells were counted from EthD-1 staining only. The sum of both was regarded as the total cell number and the ratio of live cells per total cells was calculated. The mean of the four images was used for statistics, so that n represents the number of coverslips.

2.8 Statistics

Data collection and calculations were performed in Excel (Microsoft) and statistical tests were made in Sigmaplot Software (Systat). Comparisons were done with Student's two sample two tailed t-test, except for excitability and Ca^{2+} imaging data.

Electrophysiological excitability data was tested by two way repeated measures ANOVA with culture condition (glia+ or glia-) as one factor and injected current or bin center potential as second factor. When significant interaction was found between the two factors, multiple comparison by Holm-Sidak method was applied to identify data points that differed between glia+ and glia- conditions.

The synchronous network burst frequency of gabazine treated networks versus control was tested by paired t-test, as pre and post gabazine data were sampled from the same networks. Ca^{2+} imaging data on Ca^{2+} dependence was tested by one way repeated measures ANOVA with Ca^{2+} concentration as factor, because data for different concentrations were derived from the same networks. *Post-hoc* comparison versus default 1.5 mM Ca^{2+} condition was done by Holm-Sidak method. Synchronous network burst frequencies in Mg^{2+} removal experiments were tested with paired t-test, as pre and post Mg^{2+} removal data was sampled from the same networks.

p-values smaller than 0.05 were regarded as significant and marked with a single asterisks in graphs. Two asterisks mark p-values smaller than 0.01 and three asterisks p-values smaller than 0.001. Bars in graphs and text values represent the arithmetic means. Errors in text and on bars in graphs represent the standard errors of the mean. Statistical n is mentioned in respective paragraphs in the results section and in figure legends. Graphs were created in Sigmaplot (Systat) except vertical point graphs, which were created with Origin (Originlab) and layout of figures was created using Corel Draw.

3 Results

3.1 Influence of intrinsic glial cells on human neuronal networks

In the field of human neuronal *in vitro* cultures, maturity is still an important issue, because neurons that are comparable to murine cultures regarding functional maturity are hard to obtain and usually poorly characterized. Although murine glial cells have already been used to enhance maturation of human neuronal networks *in vitro* (Odawara at al., 2014), the effects of co-culturing human glial cells with human networks (glia+ culture) were not yet characterized. This work establishes human neuron-glia co-cultures, inwhich the glial cells are derived from the same iPSC derived NSC population as the neurons. A parallel, detailed functional analysis of an almost glia free culture (glia- culture)allowed to study the effect of intrinsic glial cells on the function of the neurons and their network by means of immunocytochemistry, electrophysiology and Ca^{2+} imaging.

3.1.1 Cellular composition of human neuronal networks *in vitro*

Phase contrast images revealed a dense network of neurites after eight weeks post immunopanning. Somata and dendrites were observed in phase contrast in both, glia+ and glia- cultures (Figure 12). Neuronal morphologies and density were similar in both types of cultures. Compared to cultures at one week post immunopanning, the neuritic network dramatically increased in density. In addition to the neurons (usually bright in phase contrast), another cell type characterized by its flat translucent morphology was present in the glia+ cultures (Figure 12C, arrows) which was absent in the glia- cultures (Figure 12D).

To identify cell types, immunocytochemistry was applied to cultures after eight weeks post panning (Figure 13). Using microtubule-associated protein 2 (MAP2) as a neuronal marker abundant in soma and dendrites (Caceres et al., 1984), most of the cells exhibited neuronal morphology as well as a strong dendritic arborization, which did not differ between cells from glia+ and glia- cultures (Figure 13A, B). For quantification, co-staining with the nuclear marker DAPI was used to identify single cells in the MAP2 signal. The ratio of MAP2 positive cells per DAPI nuclei increased significantly from 74 ± 2.3% (n = 6) in glia+ cultures to 88 ± 1.8% (n = 8) in glia- cultures (Figure 13E, $p < 0.001$). The absolute density of MAP2 positive cells was not different with 368 ± 79 cells/mm² (n = 10) and 392 ± 42 cells/mm²,

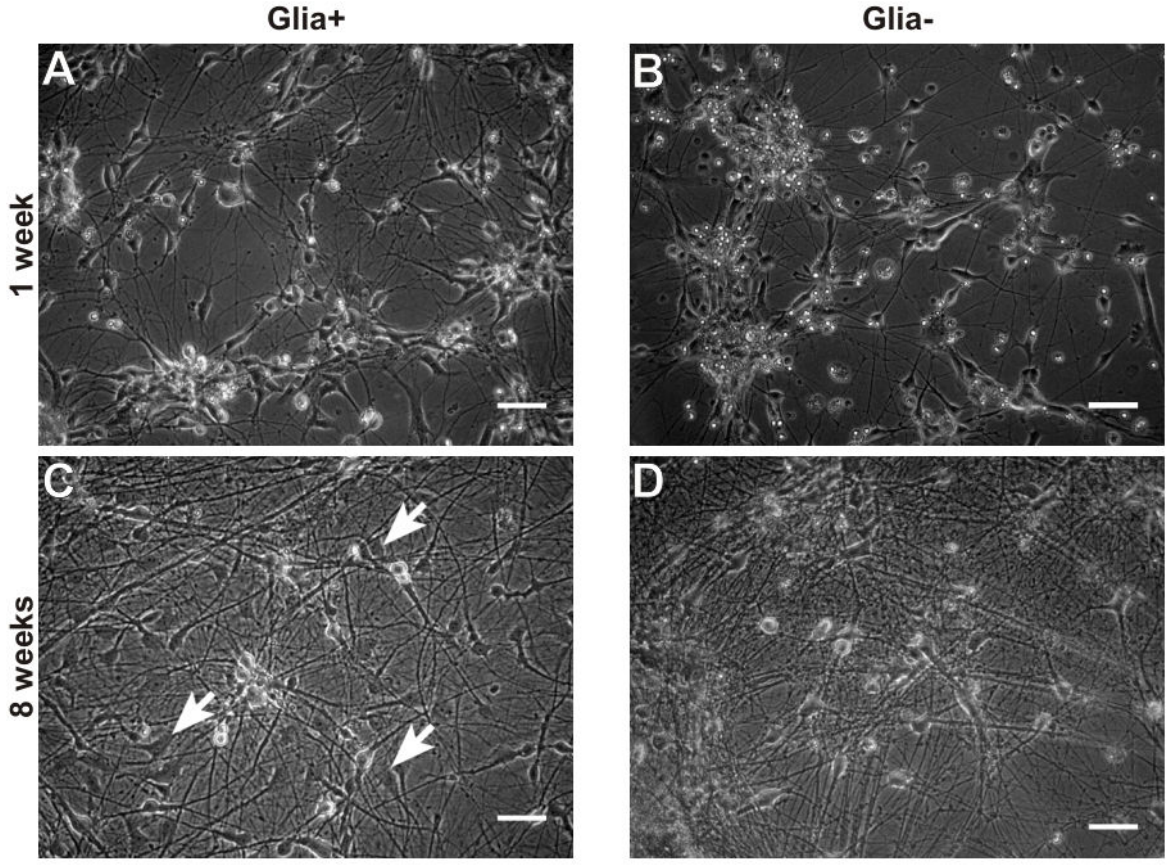

Figure 12: *In vitro* maturation of human iPSC derived neurons.
Phase contrast images. **A, B:** Glia+ (A) and glia- (B) culture 1 week post immunopanning. **C, D:** Glia+ (C) and glia- (D) culture 8 weeks post immunopanning, arrows = glial cells. Scale bar = 50 µm.

respectively (n = 10), indicating, that glia+ cultures contained some additional non-neuronal cells (Figure 13G).

To check whether the non-neuronal cells, that were also observed in phase contrast, were glial cells, immunostaining for glial fibrillary acidic protein (GFAP) as a somatic astrocyte cell marker was used (Eng, 1985). As evident from GFAP positive somata, the additional cell population in the glia+ cutlures was identified as glial cells (presumably astrocytes) by immunostaining (Figure 13C), whereas in glia- cultures, GFAP positive cells were almost completely absent (Figure 13D). Long and thin processes could be observed in all cultures, crossing a long distance through the field of view as also glia- cultures were not completely free of glial cells. DAPI co-staining was used to quantify single cells showing GFAP signal. Quantification revealed a significant reduction of glial cells per DAPI nuclei from $10.9 \pm 5.3\%$ (n = 6) in glia+ cultures to $1.0 \pm 0.3\%$ (n = 8) in glia- cultures (Figure 13F, $p < 0.05$).

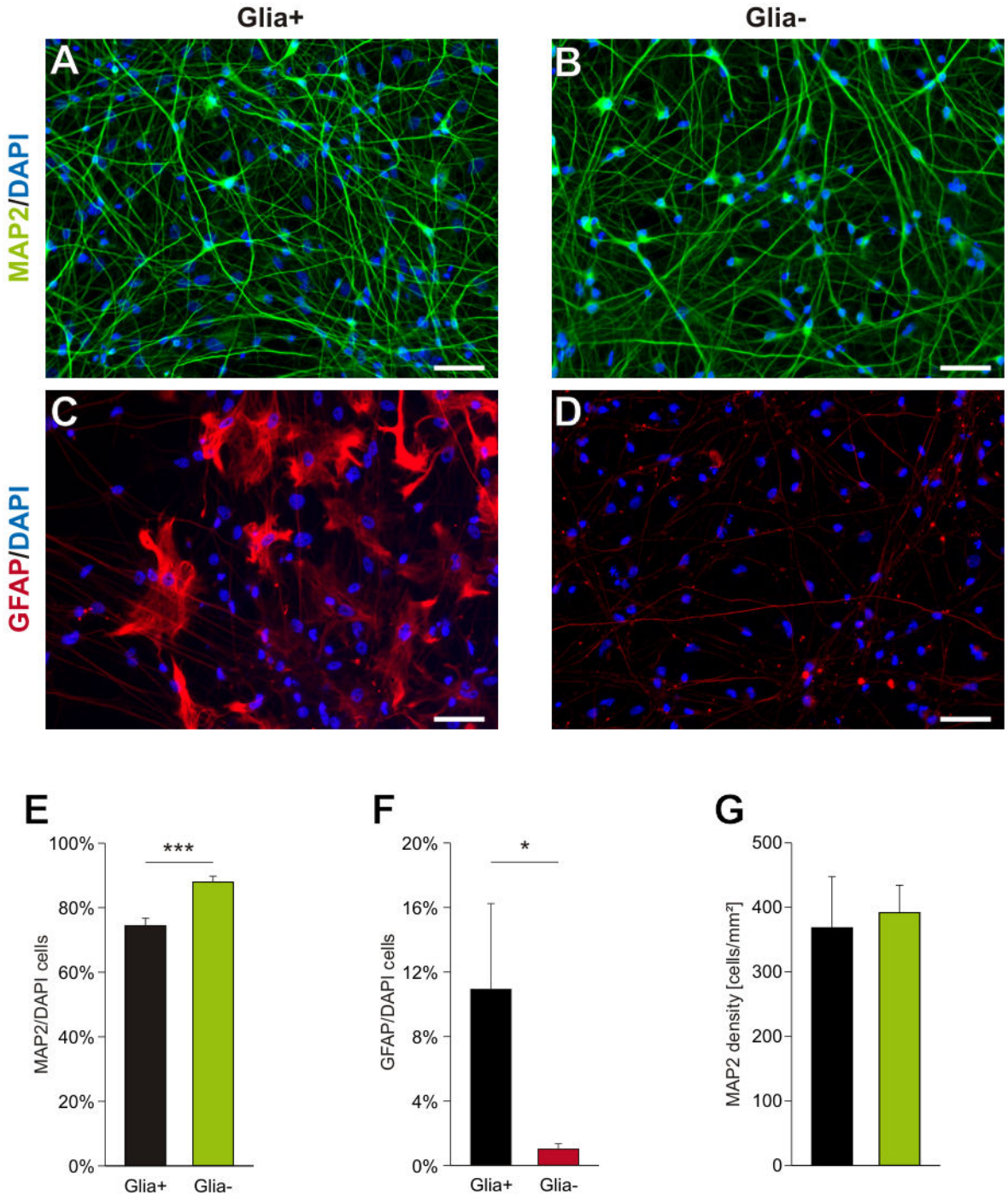

Figure 13: Immunocytochemistry for MAP2 and GFAP in human iPSC derived neurons.
Glia+ cultures are enriched in glial cells (presumably astrocytes). **A, B:** MAP2 (green) and nuclei (DAPI, blue) co-stain of glia+ (A) and glia- (B) culture. **C, D:** GFAP (red) and nuclei (DAPI, blue) co-stain of glia+ (C) and glia- (D) culture. **E:** Quantification of MAP2 positive cells as ratio to DAPI positive nuclei in glia+ (n = 6) and glia- (n = 8) cultures. **F:** Quantification of GFAP positive cells as ratio to DAPI positive nuclei in glia+ (n = 6) and glia- (n = 8) cultures. **G:** Quantification of absolute density of MAP2 positive cells per area in glia+ (n = 10) and glia- (n = 10) cultures. Scale bars = 50µm. Bars and error bars represent means and standard errors of the mean, respectively. * $p < 0.05$, *** $p < 0.001$, Student's t-test.

To asses neuronal cell type identity, glutamate decarboxylase 67 (GAD67) immunostaining was used. GAD67 is a somatic GABA-ergic cell marker, thus making it possible to identify GABA-ergic neurons (Gonzales et al., 1991). GAD67 revealed clear somatic staining which was overlapping with MAP2, demonstrating its neuronal specificity. DAPI co-staining was used to quantify cells. Both GAD67 negative and GAD67 positive neurons were present. Quantification of GAD67 immunostaining resulted in 23.8 ± 4.8% (n = 6) GAD67 positive per MAP2 positive cells in glia+ and in 29.7 ± 1.9% (n = 6) in glia- cultures. There was no significant difference between cultures, suggesting that the identity of neurons is not affected by the presence of glial cells.

In summary, the absence of glial cells in the glia- cultures as compared to glia+ cultures did not affect neuronal density, identity or neurite outgrowth, thus forming the basis for a comparative functional study.

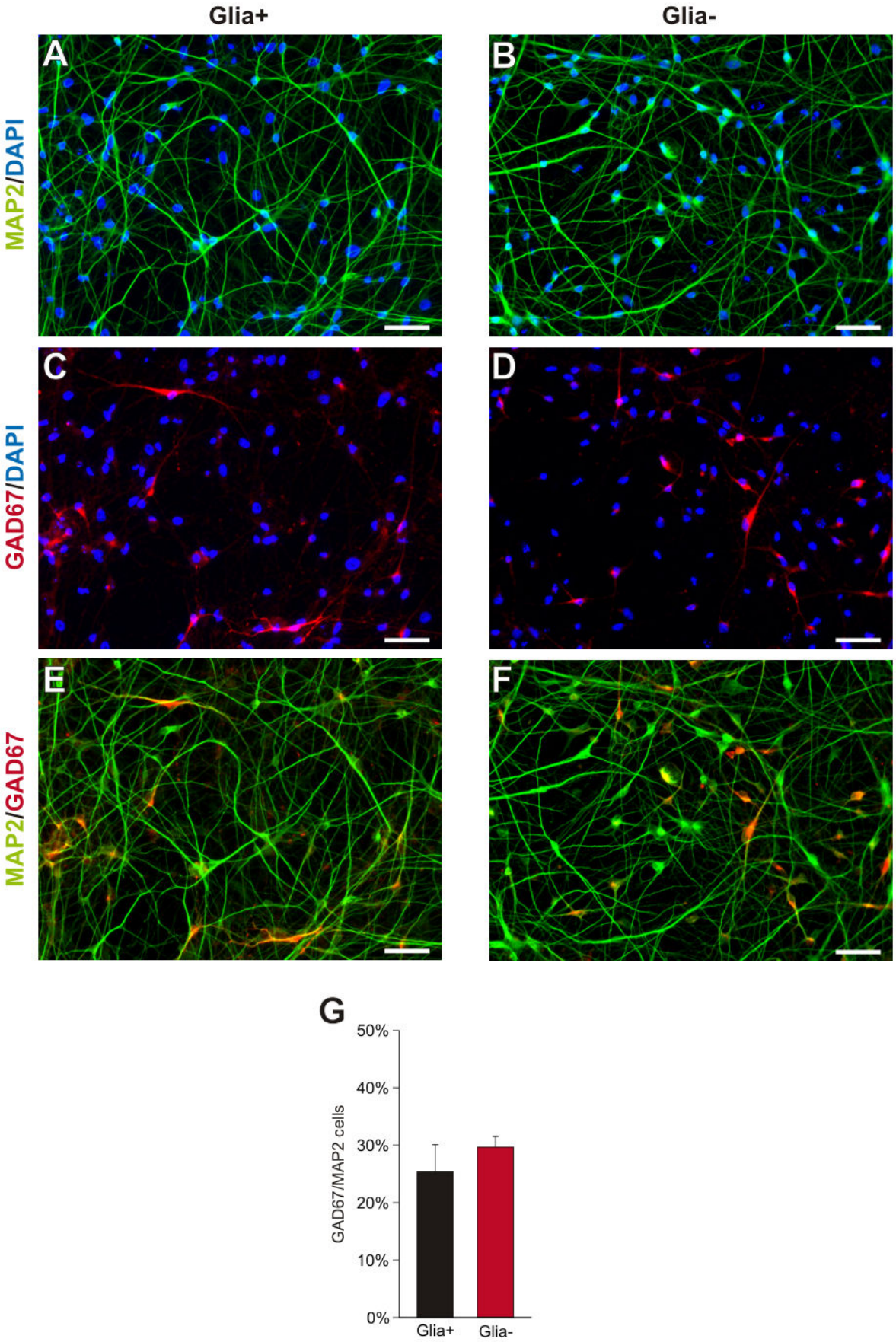

Figure 14: Immunocytochemistry for GAD67 in human iPSC derived neurons.
Figure legend on next page.

Figure 14 legend: A, B: MAP2 (green) and nuclei (DAPI, blue) co-staining of glia+ (A) and glia- (B) cultures. **C, D:** GAD67 (red) and nuclei (DAPI, blue) co-staining of glia+ (C) and glia- (D) cultures. **E, F:** GAD67 (red) and MAP2 (green) co-staining of glia+ (C) and glia- (D) culture. **G:** Quantification of GAD67 positive cells as fraction of MAP2 positive cells in glia+ (n = 6) and glia- (n = 6) cultures. Scale bars = 50 µm. Bars and error bars represent means and standard errors of the mean, respectively. No significant effect was found with Student's t-test.

3.1.2 Effect of glial cells on electrophysiological properties of neurons

To functionally characterize the human neurons and to study influences of glial cells on their function, electrophysiological properties of mature neurons from glia+ and glia- cultures were analyzed. Whole cell patch clamp experiments were conducted to assess passive and spiking properties at subpopulation level and voltage dependent Na^+ currents as well as general synaptic integrity.

3.1.2.1 Definition of subpopulations

In depth electrophysiological analysis was done by whole cell current clamp recordings with the fluorescent dye Alexa Fluor 488 in the patch pipette, which diffuses into the cytosol upon opening of the cell (Figure 11). Thus making the detailed morphology of the patched cell visible. Taking fluorescence images of these cells after electrophysiological measurements enabled the definition of morphological subpopulations.Morphological observations gave rise to three groups of cells. The most abundant cell morphology was the multipolar type, which was defined as a roughly radial symmetric cell with multiple dendrites branching into all directions and creating several levels of subbranches (Figure 15A). The pyramidal type was characterized by an asymmetric morphology, which was dominated by a single, long and straight “apical” dendrite with limited branching and smaller, short “basal” dendrites directly originating from the soma (Figure 15B). All cells that could not be sorted into one of these two subpopulations were sorted into the unidentified group. Mostly small and bipolar cells were sorted into this group (Figure 15C). Damaged cells were ignored completely and not further analyzed.

The same morphologies were found in glia- cultures without any obvious differences between the two types of cultures (Figure 16). However, a slight tendency to reduced branching and smaller cell size was observed in neurons from glia- cultures.

All cell types were observed in both glia+ and glia- cultures in similar amounts, as evident from the quantification (Figure 17). 69% in glia+ and 64% in glia- cultures were of the

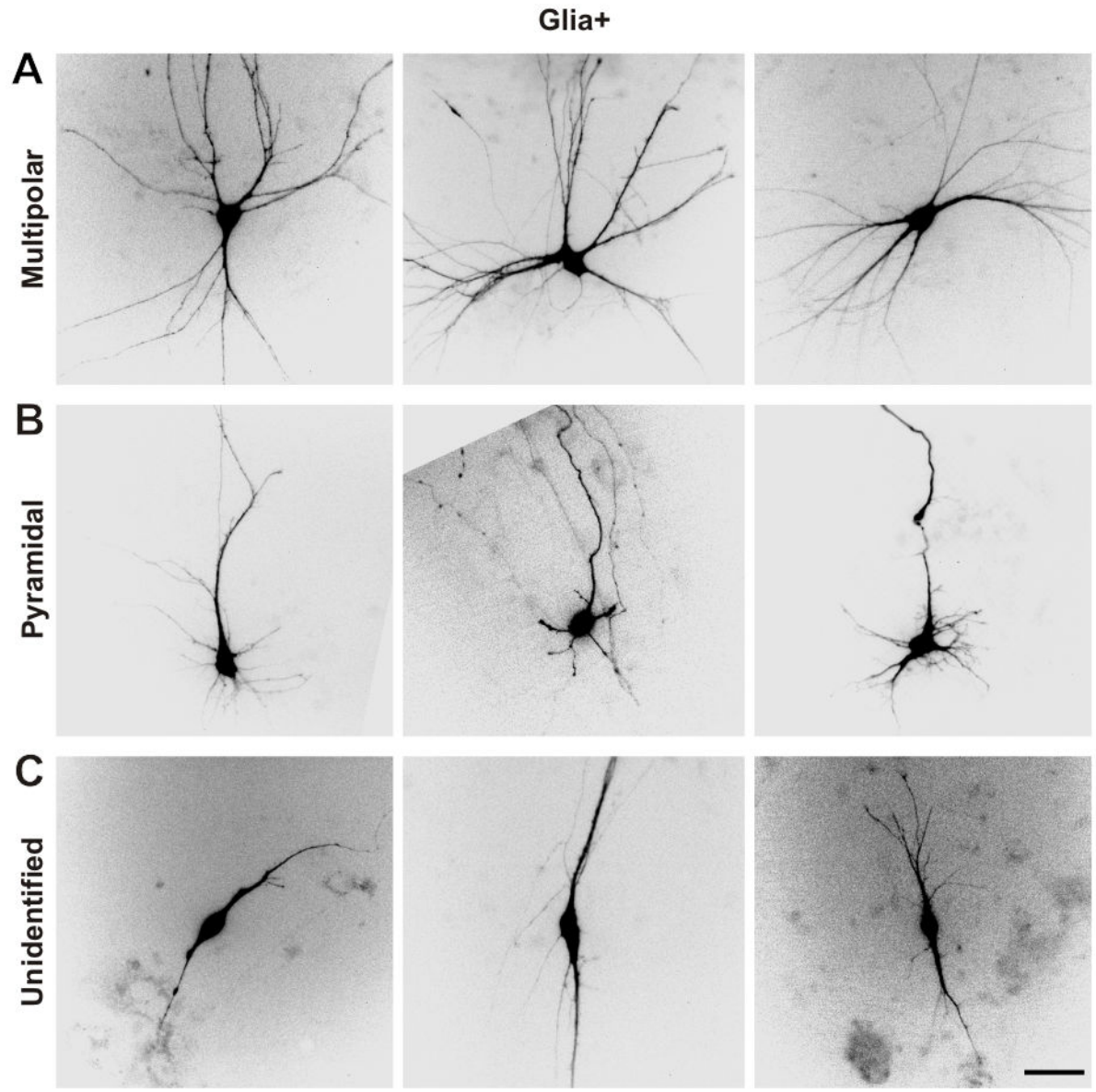

Figure 15: Human iPSC derived neurons from glia+ cultures filled with Alexa Fluor 488.
A: Neurons with multipolar morphology. **B:** Neurons with pyramidal morphology. **C:** Unidentified neurons with bipolar morphology. Scale bar = 50 µm.

multipolar cell type. Pyramidal cells were less abundant with only 14% in both cultures. The unidentified population was approximately in the same range as the pyramidal population with 17% in glia+ and 22% in glia- cultures.

In summary, the fractions of morphologically identified neurons in glia+ and glia- cultures was not different despite a very slight tendency to less branching and smaller cell sizes in the glia- cultures as compared to glia+ cultures.

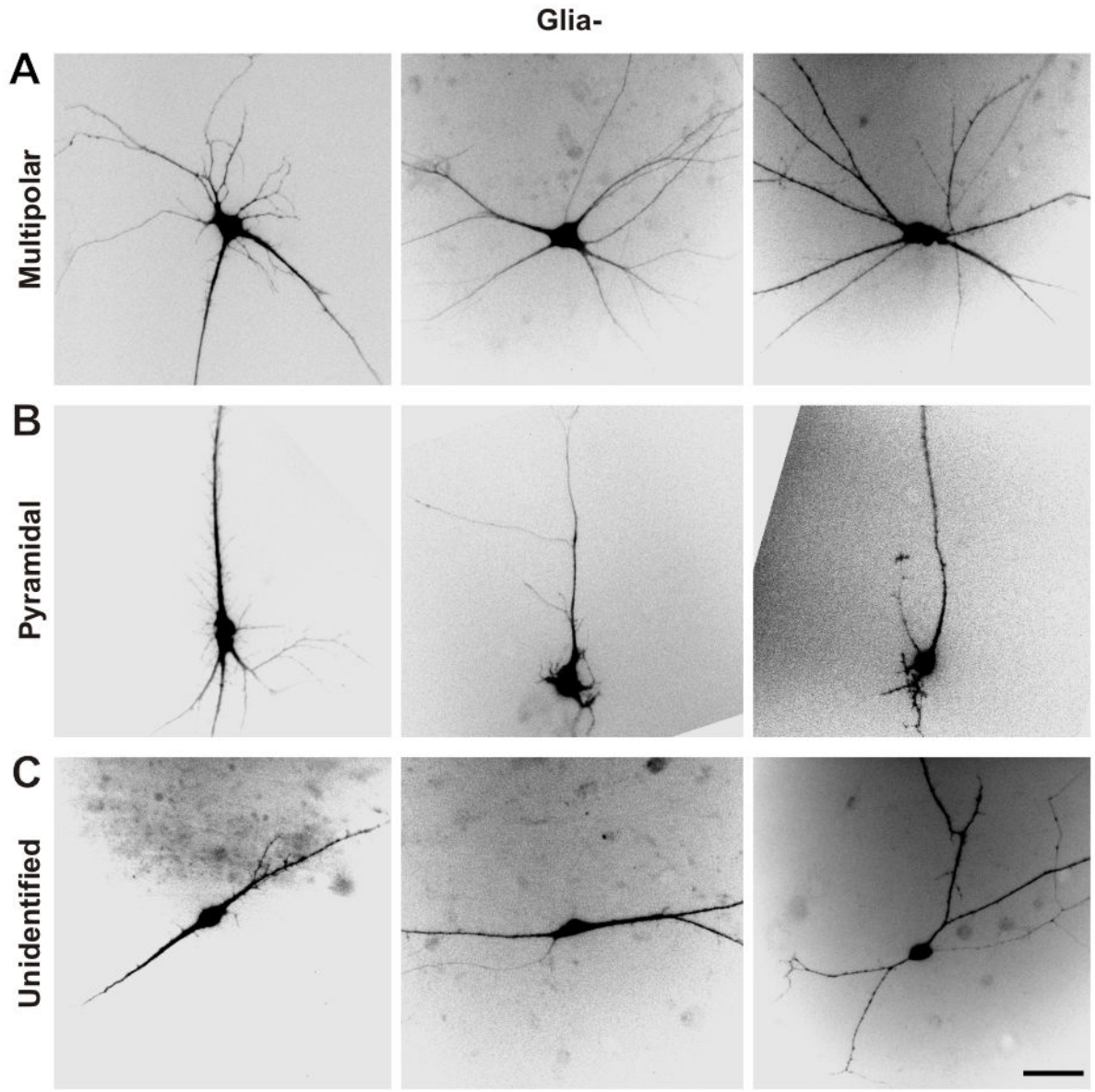

Figure 16: Human iPSC derived neurons from glia- cultures filled with Alexa Fluor 488.
A: Neurons with multipolar morphology. **B:** Neurons with pyramidal morphology. **C:** Unidentified neurons with bipolar morphology. Scale bar = 50 µm.

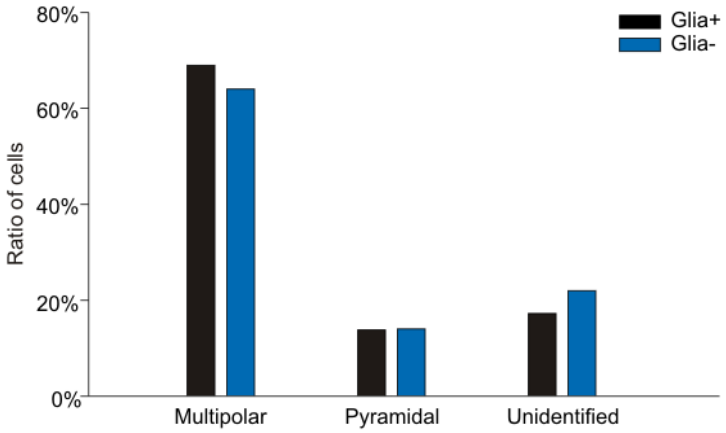

Figure 17: Quantification of morphologies of human iPSC derived neurons filled with Alexa Fluor 488.
Ratios of indicated subpopulations per total cell number in glia+ and glia- cultures.

3.1.2.2 Effects of glial cells on passive properties of subpopulations

To check the basic cell membrane properties, passive electrophysiological properties have been analyzed from multipolar (glia+: n = 40, glia-: n = 33) and pyramidal (glia+: n = 8, glia-: n = 8) cells (Figure 18). Unidentified cells were not used for further analysis because of their heterogeneity and partially immature appearance. Before application of any current, resting membrane potential (RMP) was recorded. No significant differences were found between glia+ and glia- cultures in any of the two subpopulations. In the multipolar population, glia+ cultures had a RMP of -39.9 ± 2.1 mV and glia- cultures had a RMP of -43.4 ± 2.4 mV. Pyramidal cells had a RMP of -51.4 ± 2.5 mV in glia+ and -42.7 ± 3.7 mV in glia- cultures (Figure 18C, D).

Current was then injected to hold cells at a potential of -70 mV and a 400 ms long pulse of additional -20 pA was applied 20 times. The resulting potentials were averaged and had the typical exponential shape (Figure 18A, B). Traces were analyzed to obtain time constant tau, total input resistance and cell capacitance. For the multipolar cell type, neurons from glia+ cultures exhibited a mean tau of 47.2 ± 3.2 ms and neurons from glia- cultures showed a mean tau of 46.3 ± 4.0 ms (Figure 18E, F). Pyramidal cells had a mean mean tau of 37.4 ± 4.6 ms in glia+ and of 43.6 ± 6.3 ms in glia- cultures. There was no significant difference between glia+ and glia- cultures. In the multipolar population, there was a significant difference between neurons from glia+ and glia- cultures in total input resistance (Figure 18G, H, $p < 0.05$). Total input resistance was increased from 577 ± 55.1 MΩ in neurons from glia+ cultures to 980 ± 161 MΩ in neurons from glia- cultures. In the pyramidal population, there was no

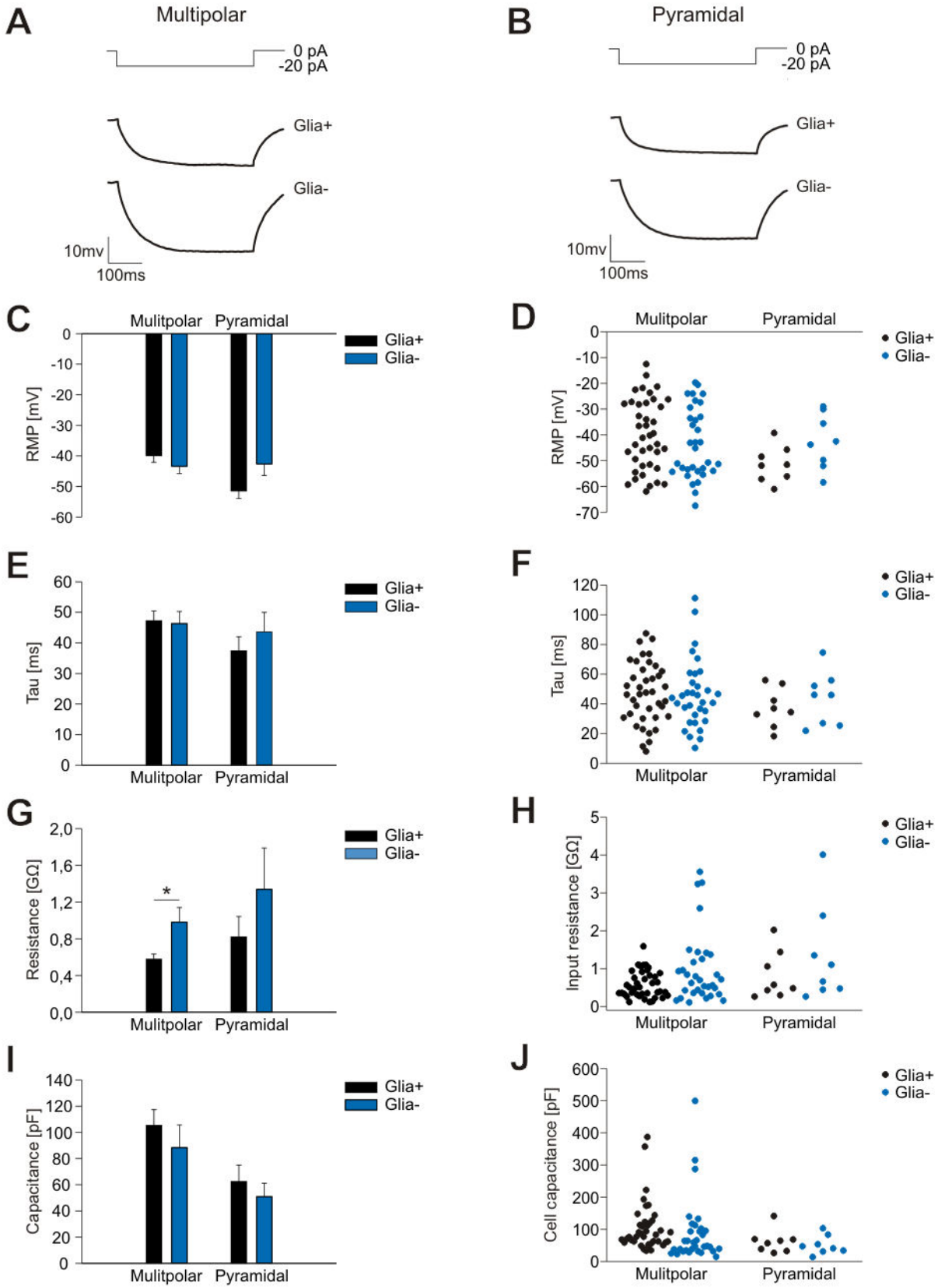

Figure 18: Passive electrophysiological properties of human iPSC derived neurons.
Multipolar (glia+: n = 40, glia-: n = 33) and pyramidal (glia+: n = 8, glia-: n = 8) cells were analyzed separately. Legend continues on next page.

Figure 18 legend continued: A, B: Mean potential responses to 20 hyperpolarizing current pulses of -20 pA in multipolar (A) and pyramidal (B) neurons from glia+ (top) and glia- (bottom) cultures. **C:** Resting membrane potential (RMP) of multipolar and pyramidal neurons from glia+ and glia- cultures. **D:** Single cell values corresponding to C. **E:** Time constant tau determined from hyperpolarizing potential responses of multipolar and pyramidal neurons from glia+ and glia- cultures. **F:** Single cell values corresponding to E. **G:** Total input resistance analyzed from hyperpolarizing potential responses in multipolar and pyramidal neurons from glia+ and glia- cultures, * $p < 0.05$, Student's t-test. **H:** Single cell values corresponding to G. **I:** Cell capacitance calculated from time constant tau and total input resistance of multipolar and pyramidal neurons from glia+ and glia- cultures. **J:** Single cell values corresponding to G. Bars and error bars represent means and standard errors of the mean, respectively.

significant difference. Resistance was 820 ± 223 MΩ in neurons from glia+ and $1{,}338 \pm 452$ MΩ in neurons from glia- cultures. Cell capacitance showed no significant difference between neurons from both culture types (Figure 18I, J). The multipolar population had a capacitance of 105.3 ± 12.1 pF in glia+ and 99.8 ± 17.4 pF in glia- cultures. Pyramidal capacitance was lower, with 62.3 ± 12.7 pF in glia+ and 50.9 ± 10.3 pF in glia- cultures.

In summary, there were only relatively slight differences in passive electrophysiological properties between neurons from glia+ and glia- cultures. An increase in total input resistance in the multipolar subpopulation indicated a less differentiated arborization in neurons from glia- cultures.

3.1.2.3 Effects of glial cells on action potentials of subpopulations

To investigate, whether AP generation was affected by the presence of glial cells, the first AP occurring upon depolarization (see 3.1.2.4 Effects of glial cells on excitability of subpopulations) was analyzed in multipolar (glia+: n = 38, glia-: n = 33) and pyramidal cells (glia+: n = 8, glia-: n = 8). APs of all human neurons showed the characteristic change in slope upon threshold crossing and a fast rise time to peak amplitude followed by a fast drop in voltage into afterhyperpolarization (AHP), which then slowly recovered to resting membrane potential (Figure 19A, B).

The threshold for firing an AP was not different betweeen the two culture types. In the multipolar subpulation, it was -37.5 ± 1.8 mV in glia+ and -33.6 ± 2.0 mV in in neurons from glia- cultures. Pyramidal cells had similar thresholds of -37.1 ± 1.9 mV and -35.9 ± 1.6 mV in neurons from glia+ and glia- cultures, respectively (Figure 19C, D). Similarly, the AP amplitude, which was 71.5 ± 4.4 mV in neurons from glia+ and 71.6 ± 3.9 mV in neurons from glia- cultures in the multipolar population and 81.4 ± 4.5 mV in neurons from glia+ and

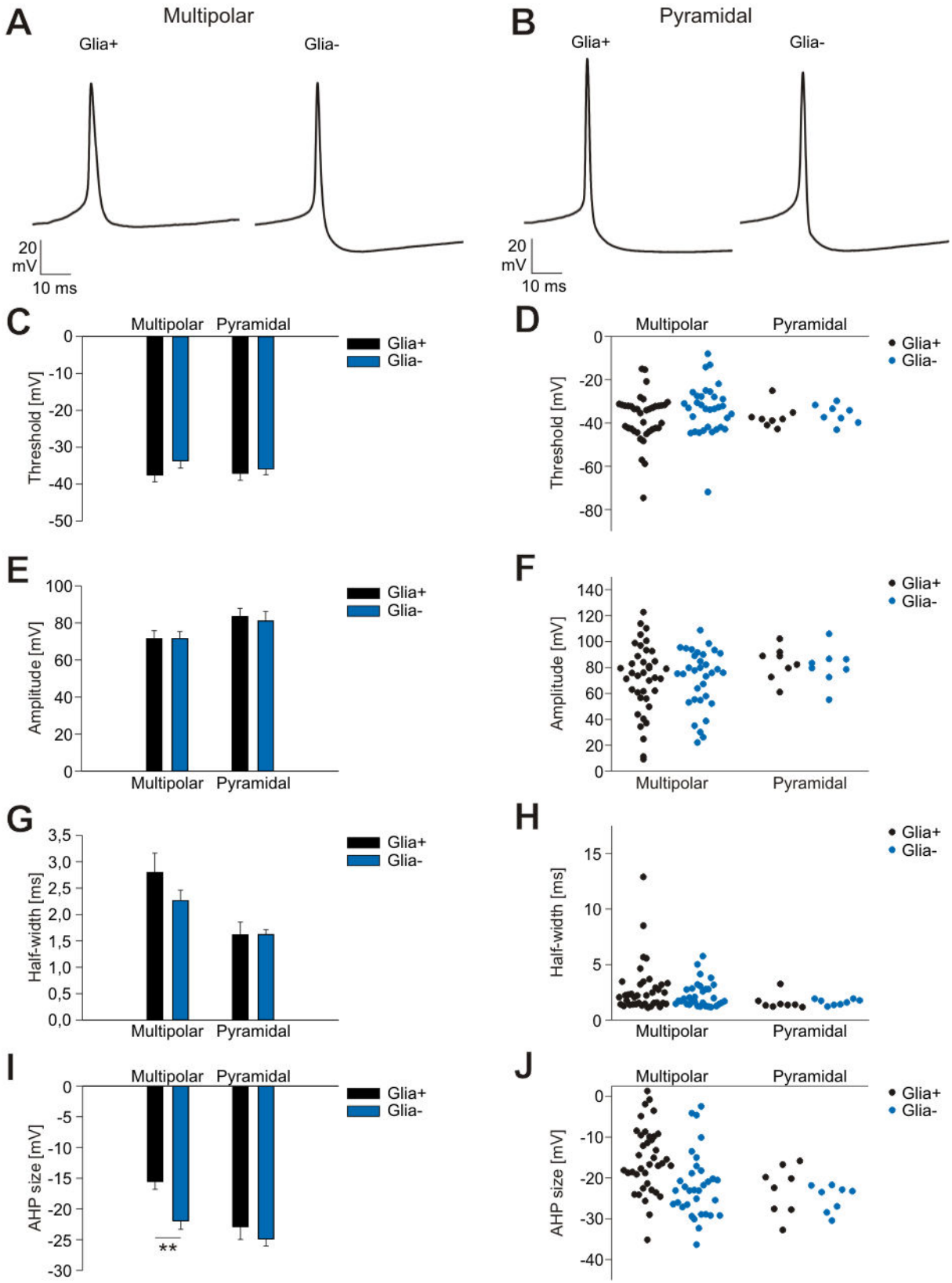

Figure 19: Action potentials of human iPSC derived neurons.
Multipolar (glia+: n = 40, glia-: n = 33) and pyramidal (glia+: n = 8, glia-: n = 8) cells were analyzed separately. Legend continues on next page.

Figure 19 legend continued: A, B: The first action potentials (APs) that occurred upon depolarization in multipolar (A) and pyramidal (B) neurons from glia+ (left) and glia- (right) cultures are shown. **C:** AP threshold of multipolar and pyramidal neurons from glia+ and glia- cultures. **D:** Single cell values corresponding to C. **E:** AP amplitudes of multipolar and pyramidal neurons from glia+ and glia- cultures. **F:** Single cell values corresponding to E. **G:** AP half-width of multipolar and pyramidal neurons from glia+ and glia- cultures. **H:** Single cell values corresponding to G. **I:** Afterhyperpolarization (AHP) of multipolar and pyramidal neurons from glia+ and glia- cultures, ** $p < 0.01$, Student's t-test. **J:** Single cell values corresponding to G. Bars and error bars represent means and standard errors of the mean, respectively.

81.4 ± 5.1 mV in neurons from glia- in the pyramidal population, was not significantly different (Figure 19E, F). Half width, as a measure of AP speed, was also not significantly different between neurons of both cultures (2.80 ± 0.38 ms in glia+ and 2.26 ± 0.20 ms in glia- cultures for multipolar cells; Figure 19G, H). Pyramidal cells had smaller half widths, in neurons from glia+ cultures it was 1.61 ± 0.24 ms and in neurons from glia- cultures it was 1.62 ± 0.09 ms. Interestingly, the size of the AHP was significantly different in the multipolar subpopulation (Figure 19I, J). It increased from -15.5 ± 1.3 mV in neurons from glia+ to -21.9 ± 1.4 mV in neurons from glia- cells ($p < 0.01$). Pyramidal cells had relatively strong AHPs: -22.9 ± 2.1 mV for neurons from glia+ and -24.9 ± 1.2 mV for neurons from glia- cultures without a significant difference.

These data suggest that there was no difference in AP parameters between neurons from glia+ and glia- cultures, except for a difference in AHP size in the multipolar subpopulation, which was increased in neurons from glia- cultures.

3.1.2.4 Effects of glial cells on excitability of subpopulations

To asses the excitability and firing behavior of subpopulations, depolarizing pulses consisting of 900 ms long current steps from -50 pA increasing stepwise by 10 pA to 240 pA were applied to multipolar (glia+: n = 40, glia-: n = 33) and pyramidal neurons (glia+: n = 8, glia-: n = 8), and resulting AP frequencies were analyzed. Almost all cells showed APs upon depolarization and most of the cells were capable of repetitive firing. Pyramidal cells were capable of higher firing rates than multipolar cells (Figure 20). Upon strong depolarization, a reduction of the AP amplitude was seen in some cells (Figure 20B, left).

Plotting the AP frequency versus the injected current (input-output relation) revealed increasing AP frequencies with increasing current injection (Figure 21). In the multipolar cells, the maximum frequency occurred at 70 pA current injection and was 6.99 ± 1.13 Hz in

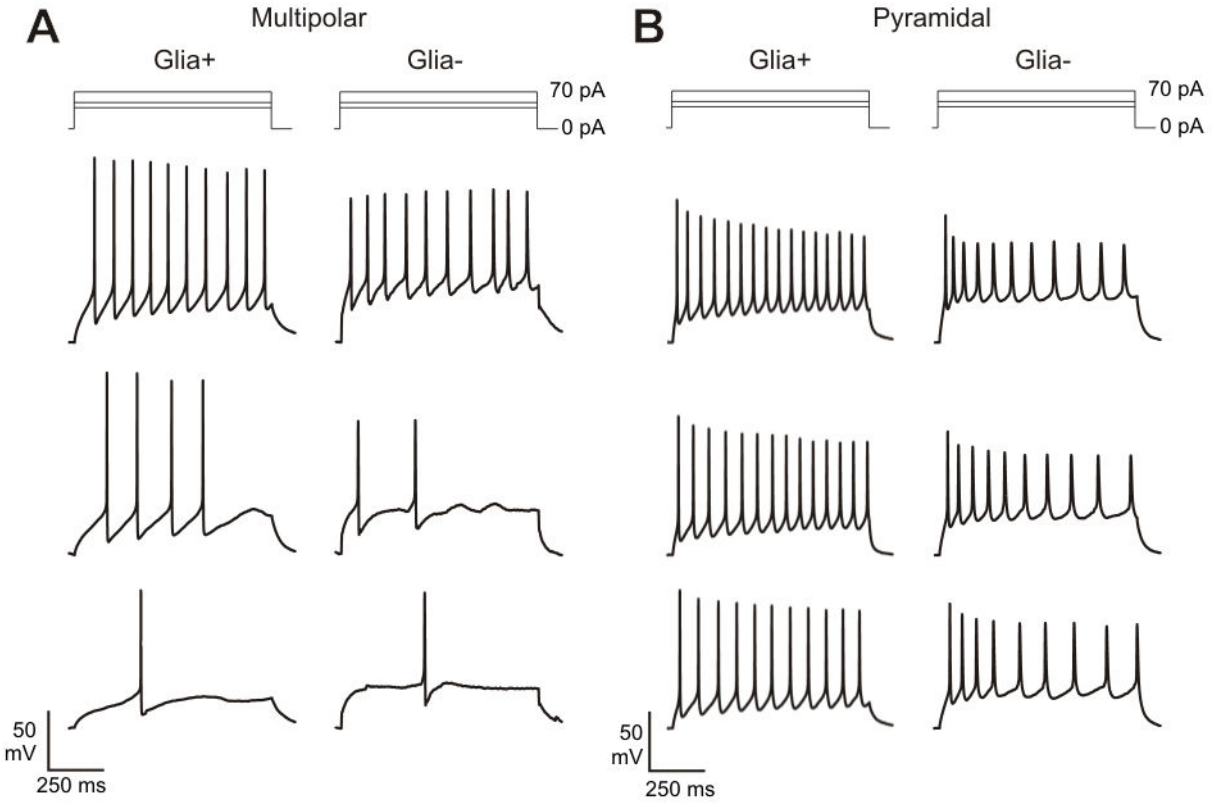

Figure 20: Spike patterns of human iPSC derived neurons.
Potential responses to depolarizing current injections of 40 (bottom), 50 (middle) and 70 pA (top) in multipolar (A) and pyramidal (B) cells from glia+ (left) and glia- (right) cultures.

neurons from glia+ and 5.83 ± 1.33 Hz in neurons from glia- cultures, showing no significant difference (Figure 21A). AP frequencies in pyramidal cells were higherand showed a strong, non-significant trend to be reduced in neurons from glia- cultures (Figure 21B). Maximum frequencies were 13.19 ± 3.93 Hz for neurons from glia+ and 8.33 ± 3.02 Hz for neurons from glia- cells at 60 pA and 70 pA current injection, respectively. The drop of AP frequencies beyond 70 pA current injection is resembling the drop of AP amplitudes at high depolarizations, making APs undetectable by the threshold based algorithm.

Because the passive electrical properties showed some differences in total input resistance, the same AP frequencies were plotted against the potential reached to minimize the influence of passive properties on spike rates. Multipolar cells had a maximum frequency at -30 mV of 8.05 ± 1.24 Hz for neurons from glia+ cultures and 5.93 ± 1.16 Hz for neurons from glia- cultures (Figure 21C). There was no significant difference between the two culture types. Pyramidal cells maintained the higher frequencies from frequency versus current plots in plots

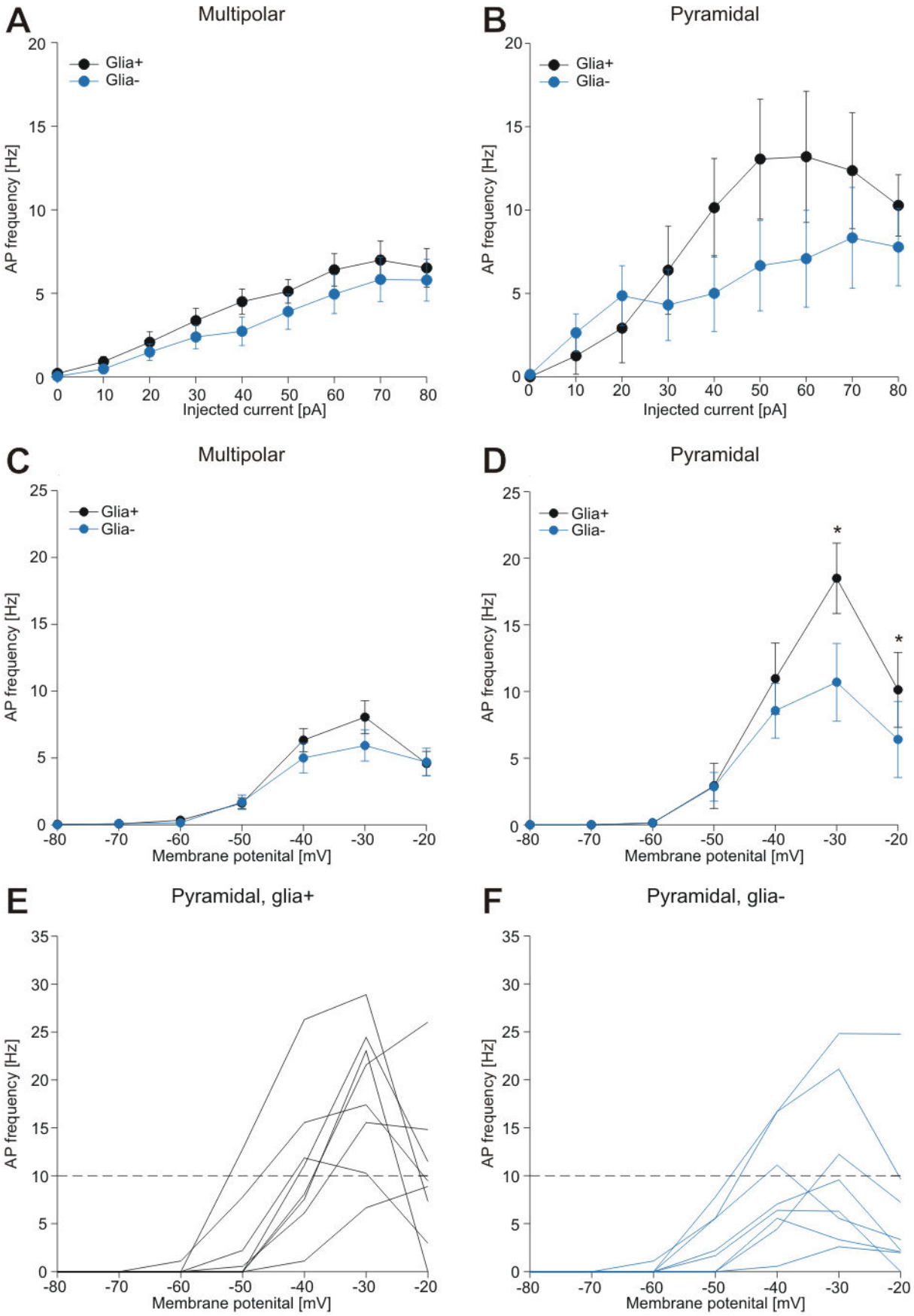

Figure 21: Input-Output relationship of human iPSC derived neurons.
Legend on next page.

Figure 21 legend: Multipolar (glia+: n = 40, glia-: n = 33) and pyramidal (glia+: n = 8, glia-: n = 8) cells were analyzed separately. **A, B:** Action potential (AP) frequency response to depolarizing current injections in multipolar (A) and pyramidal (B) cells from glia+ and glia- cultures. **C, D:** AP frequency response versus binned membrane potential measured from potential responses to current injections in pyramidal (C) and multipolar (D) cells from glia+ and glia- cultures, * $p < 0.05$, two way repeated measures ANOVA with Holm-Sidak method. **E, F:** Single cell AP frequency responses from pyramidal neurons of glia+ (E) and glia- (F) cultures, dashed line indicates, that most of the pyramidal neurons have AP frequencies above 10 Hz in glia+ cultures (E) and below 10 Hz in glia- cultures. Points and error bars represent means and standard errors of the mean, respectively.

versus potential and peaked also at -30 mV (Figure 21D). There were significant differences between cultures at this maximum, with AP frequencies decreasing from 18.49 ± 2.64 Hz in neurons from glia+ cultures to 10.69 ± 2.92 Hz in neurons from glia- cultures, and at -20 mV, with frequencies dropping from 10.12 ± 2.81 Hz to 6.40 ± 2.85 Hz in neurons from glia+ and glia- cultures, respectively ($p < 0.05$). AP frequency versus membrane potential curves for single pyramidal cells revealed, that most of pyramidal cells from glia+ cultures had maximum frequencies above 10 Hz (Figure 21E) and most of pyramidal cells from glia- cultures had maxium frequencies below 10 Hz (Figure 21F).

In summary, the maximum spike rates and thus electrical excitability were only different between glia+ and glia- cultures in the pyramidal population. Multipolar neurons seemed to be unaltered regarding their AP frequencies.

3.1.2.5 Effects of glial cells on TTX sensitive sodium ion currents

To study, whether there was a general difference in excitability arising from differences in voltage dependent Na^+ channel expression, voltage clamp experiments were attempted. Cells were depolarized from -60 mV by voltage pulses increasing by 10 mV up to 40 mV in five independent experiments. Neurons of both cultures exhibeted voltage dependent Na^+ currents in the nA range upon depolarization (Figure 22). These Na^+ currents were characterized by application of TTX, which blocked all transient currents, while leaving the outward K^+ currents unaffected. No further analysis of Na^+ currents was done, because only a rather poor spatial potential control (space clamp) could be achieved in these neurons with complex arborizations (Williams & Mitchell, 2008).

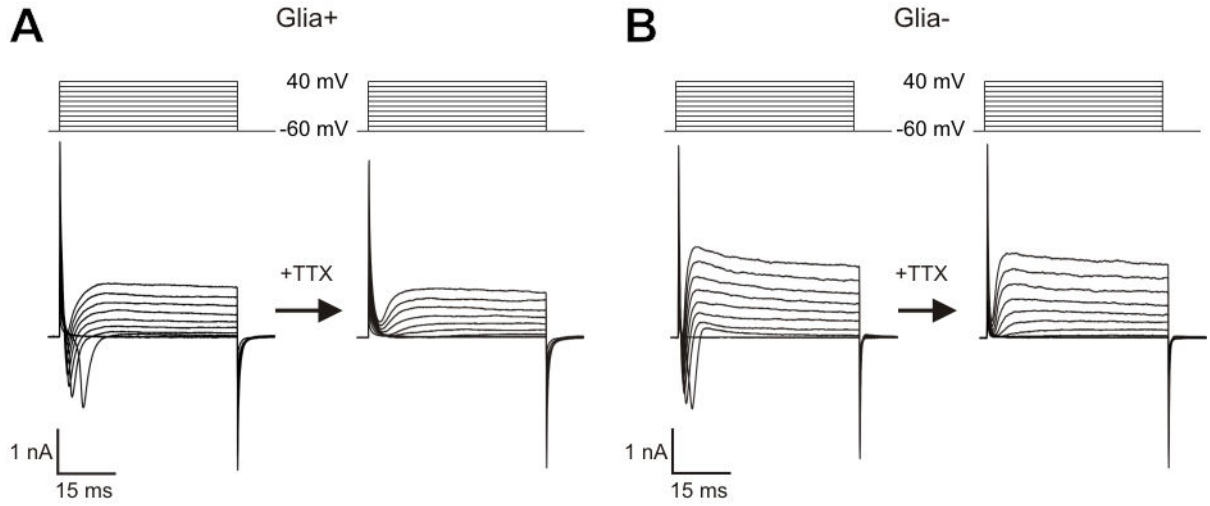

Figure 22: Human iPSC derived neurons express voltage dependent sodium and potassium ion currents.
Cells were depolarized from -60 mV by depolarizing voltage pulses increasing by 10 mV up to 40 mV. The resulting Na^+ currents are shown as negative peak currents during the first few milliseconds of depolarization. **A:** Na^+ currents of neurons from glia+ cultures (left) were blocked completely by TTX (1 µM, right), K^+ currents remained as steady outward currents. **B:** Na^+ currents of neurons from glia- cultures (left) were blocked by TTX (right), with K^+ currents remaining as steady outward currents similarly.

3.1.2.6 Effect of glial cells on synapse maturation

As effects of glia cells on synapse formation and maturation have already been studied in mouse systems and positive effects on synaptic connectivity have been found (Pfrieger and Barres, 1997; Böhler et al., 2007), the effect of the presence of glial cells in glia+ cultures on synaptic transmission was addressed. Electrophysiological measurements of pharmacologically isolated mPSCs revealed, that both culture systems developed functional synaptic transmission (Figure 23). Fast AMPA receptor mediated miniature excitatory postsynaptic currents (mEPSCs) were found in neurons from glia+, as well as in neurons from glia- cultures (Figure 23A, B). Isolation of AMPA receptor mediated mEPSCs was verified by completely blocking mEPSCs with NBQX in five independent experiments. Slow $GABA_A$ receptor mediated mPSCs were also observed in both types of cultures Figure 23C, D) and pharmacological isolation was verified by blocking mPSCs with gabazine in five independent experiments.

The quantification of mPSC data did not show any significant differences between neurons from glia+ and glia- cultures in respect to mPSC amplitude and frequency. Mean AMPA receptor mediated mEPSC frequency in neurons from glia+ cultures was 0.54 ± 0.22 Hz ($n = 20$) as compared to 0.45 ± 0.20 Hz ($n = 20$) in neurons from glia- cultures (Figure

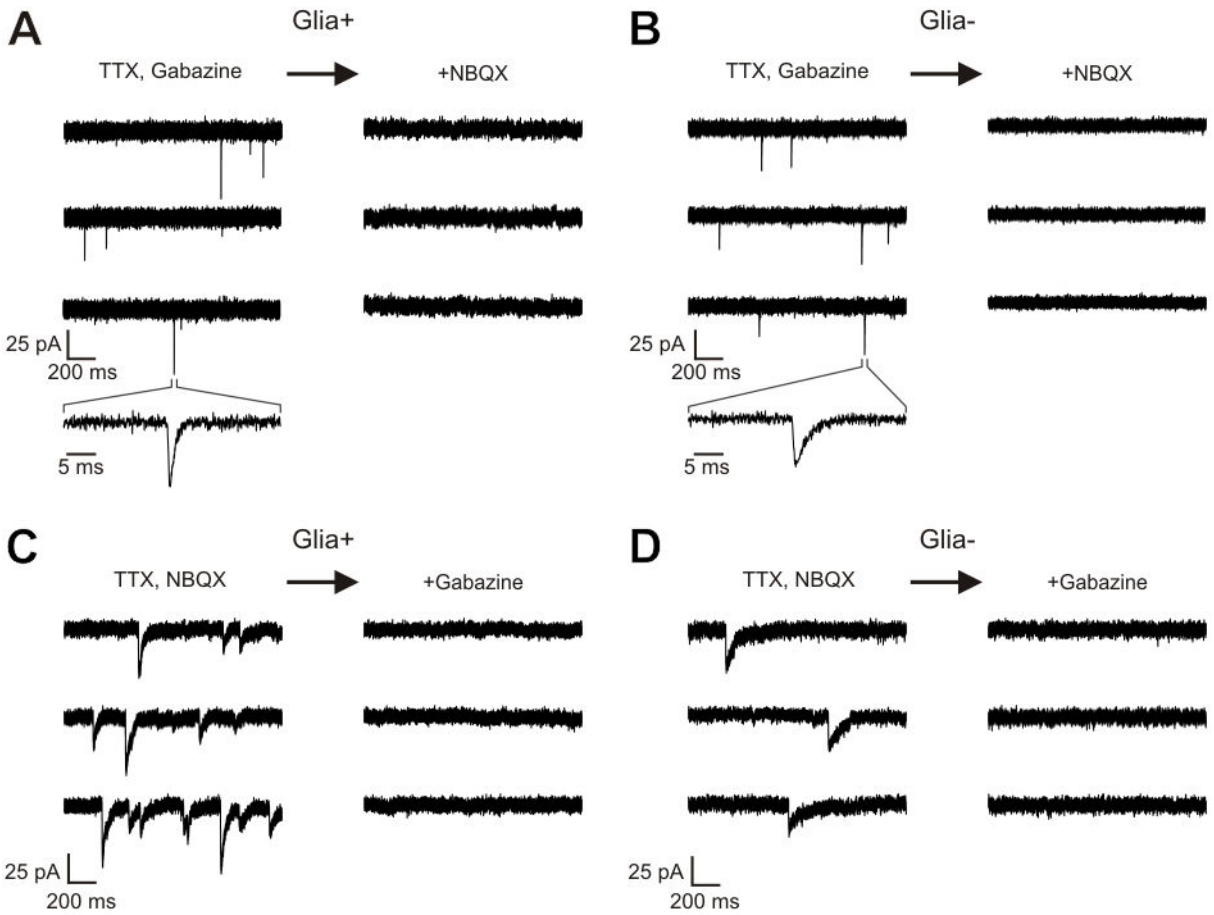

Figure 23: Miniature postsynaptic currents of human iPSC derived neurons.
A, B: AMPA receptor mediated miniature excitatory postsynaptic currents (mEPSCs) in neurons from glia+ (A) and glia- (B) cultures, pharmacologically isolated by TTX (1 µM) and gabazine (10 µM), were blocked by NBQX (10 µM). Inset trace: Enlarged single mEPSC. **C, D:** $GABA_A$ receptor mediated miniature postsynaptic currents (mPSCs) in neurons from glia+ (A) and glia- (B) cultures, pharmacologically isolated by TTX and NBQX, were blocked by gabazine.

24A+B) and the mean amplitude was 20.65 ± 1.87 pA (n = 15) and 19.69 ± 1.35 pA (n = 16) in the respective cultures (Figure 24C, D). Cumulative frequency distribution of amplitudes was also not different, with half of the mEPSCs having an amplitude not larger than approximately 17.5 pA in neurons from both cultures (Figure 24E).

$GABA_A$ receptor mediated mPSCs showed a trend to a reduced frequency, with mean frequencies of 1.22 ± 0.73 Hz (n = 19) in neurons from glia+ and 0.07 ± 0.03 Hz (n = 19) in neurons from glia- cultures (Figure 25A). However, statistics and single cell values showed that this trend was solely driven by two cells with very high mPSC frequencies in neurons from glia+ cultures and thus not significant (Figure 25B). Amplitudes were 19.24 ± 1.02 pA (n = 15) and 21.38 ± 1.35 pA (n = 14) in neurons from glia+ and glia- cultures, respectively (Figure 25C, D) the and cumulative frequency distribution of amplitudes showed a small shift

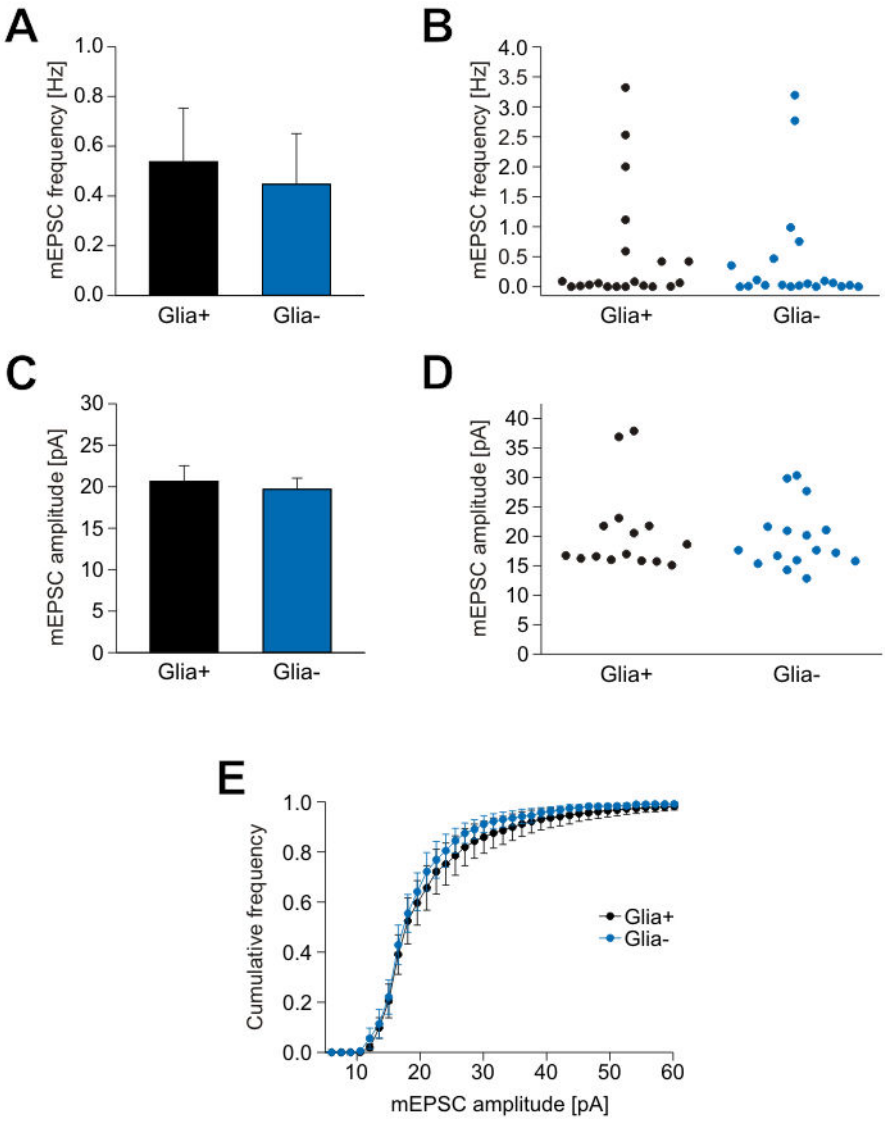

Figure 24: Quantification of AMPA receptor mediated miniature excitatory postsynaptic currents.
A: Frequency of miniature excitatory postsynaptic currents (mEPSC) in neurons from glia+ and glia- cultures. **B:** Single cell values of mEPSC frequencies corresponding to A. **C:** Amplitude of mEPSCs in neurons from glia+ and glia- cultures. **D:** Single cell values of mEPSC amplitudes corresponding to C. Bars and error bars represent means and standard errors of the mean, respectively. **E:** Cumulative frequency plot of mEPSC amplitudes. Points and error bars represent means and standard errors of the mean, respectively. No significant effect was found with Student's t-test.

of neurons from glia- cultures to slightly larger $GABA_A$ receptor mediated mPSCs (Figure 25E). Half of the mEPSCs had an amplitude not larger than approximately 17 pA in neurons from glia+ cultures and 21 pA in neurons from glia- cultures. However, there was no significant difference in the mean mPSC amplitude between neurons from glia+ and glia- cultures.

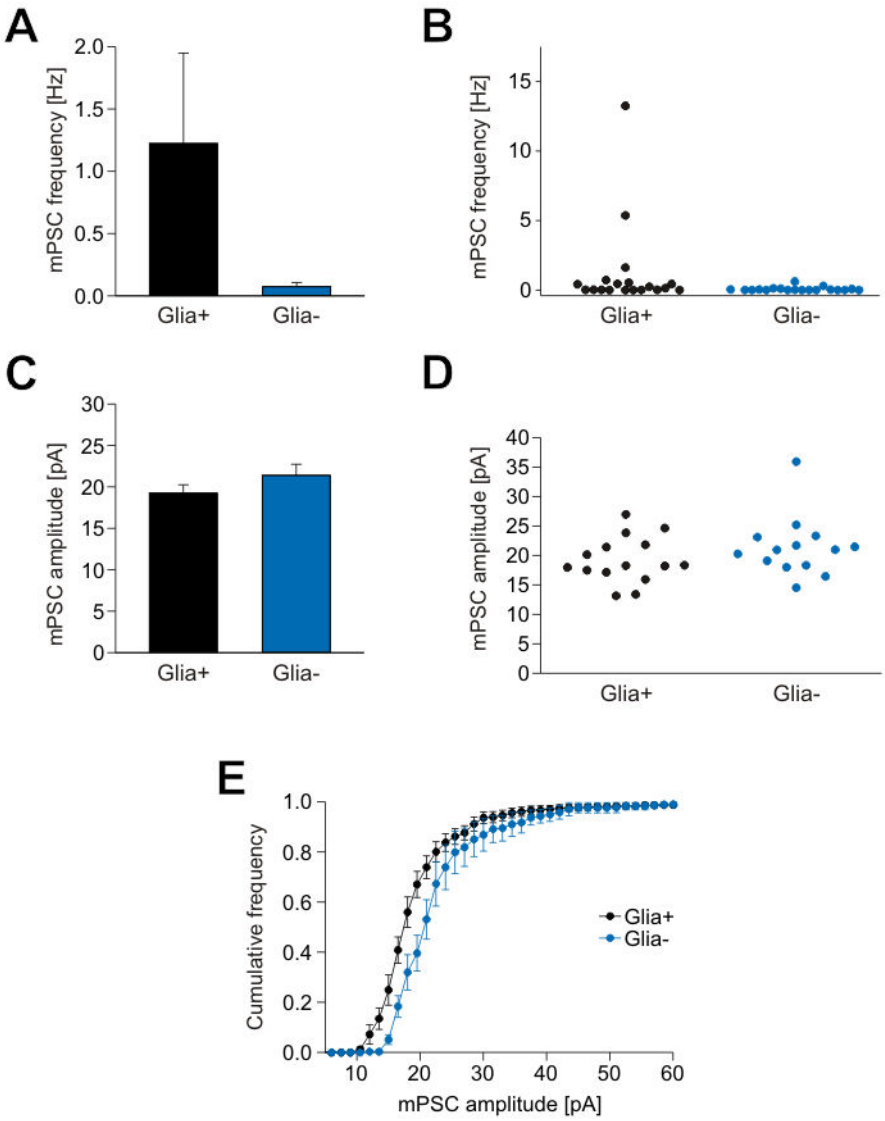

Figure 25: Quantification of $GABA_A$ receptor mediated miniature postsynaptic currents.
A: Frequency of miniature postsynaptic currents (mPSC) in neurons from glia+ and glia- cultures. **B:** Single cell values of mPSC frequencies corresponding to A. **C:** Amplitude of mEPSCs in neurons from glia+ and glia- cultures. **D:** Single cell values of mPSC amplitudes corresponding to C. Bars and error bars represent mean and standard error of the mean, respectively. **E:** Cumulative frequency plot of mPSC amplitudes. Points and error bars represent means and standard errors of the mean, respectively. No significant effect was found with Student's t-test.

In summary, neither synaptic responses mediated by AMPA receptors nor by $GABA_A$ receptors were significantly different between neurons from glia+ and glia- cultures.

3.1.3 Assessment of network function by calcium imaging

To asses the integration of neurons into a functional network, Fluo-4 based Ca^{2+} imaging was established in glia+ cultures to measure the intracellular Ca^{2+} levels of neurons. As intracellular Ca^{2+} concentration increases upon electrical activity due to Ca^{2+} influx from extracellular space through voltage gated Ca^{2+} channels and Ca^{2+} release from intracellular stores, this method can be used to estimate neuronal activity (Opitz et al., 2002). To study spontaneous network activity, Ca^{2+} imaging was done at arelatively low sample rate (1 Hz) and a low magnification (10×) for 5 min. In the end of each experiment, KCl with a final concentration of 40 mM was added to the imaging buffer to achieve maximum Ca^{2+} signals in neurons (Figure 26). This response was then used to define regions of interest (ROIs) around neuron somata for further analysis.

Analysis of imaging data revealed spontaneous single neuron activity ("blinking" of single neurons) that synchronized in regular intervals into a network-wide strong Ca^{2+} signal, which were strongest in somata, but also quite intense in the proximal dendrites of mature neurons (Figure 26A-D). Synchronous bursts of activity resulted in Ca^{2+} signal peaks, and treatment with KCl resulted in a huge Ca^{2+} signal involving all healthy neurons (Figure 26E-H).

To more specifically identify and quantify these spontaneous synchronous network bursts, the Ca^{2+} response induced by K^+ depolarization (KCl response) was used to define ROIs around neuron somata and to subsequently analyze the whole file by a macro written in ImageJ (NIH). The difference between each image and its preceding one was calculated, thus getting a kind of derivate of the fluorescence signal (see 6.4.1 ImageJ macro for the analysis of calcium imaging data). The subtracted images containing the KCl response were then summed up by using the *maximum projection* function of ImageJ (Figure 26I) followed by background subtraction (*rolling ball*) and subsequent automatic thresholding by the *moments* algorithm. The resulting binary image was median filtered to remove noise and a *watershed* algorithm was run to separate merged somata. This procedure resulted in a binary image mask of detected somata (Figure 26J). *Analyze particles* function of ImageJ was used to automatically create ROIs out of this binary image and transfer them to the original image stack, where mean fluorescence intensity per ROI versus time was analyzed and output to a table.

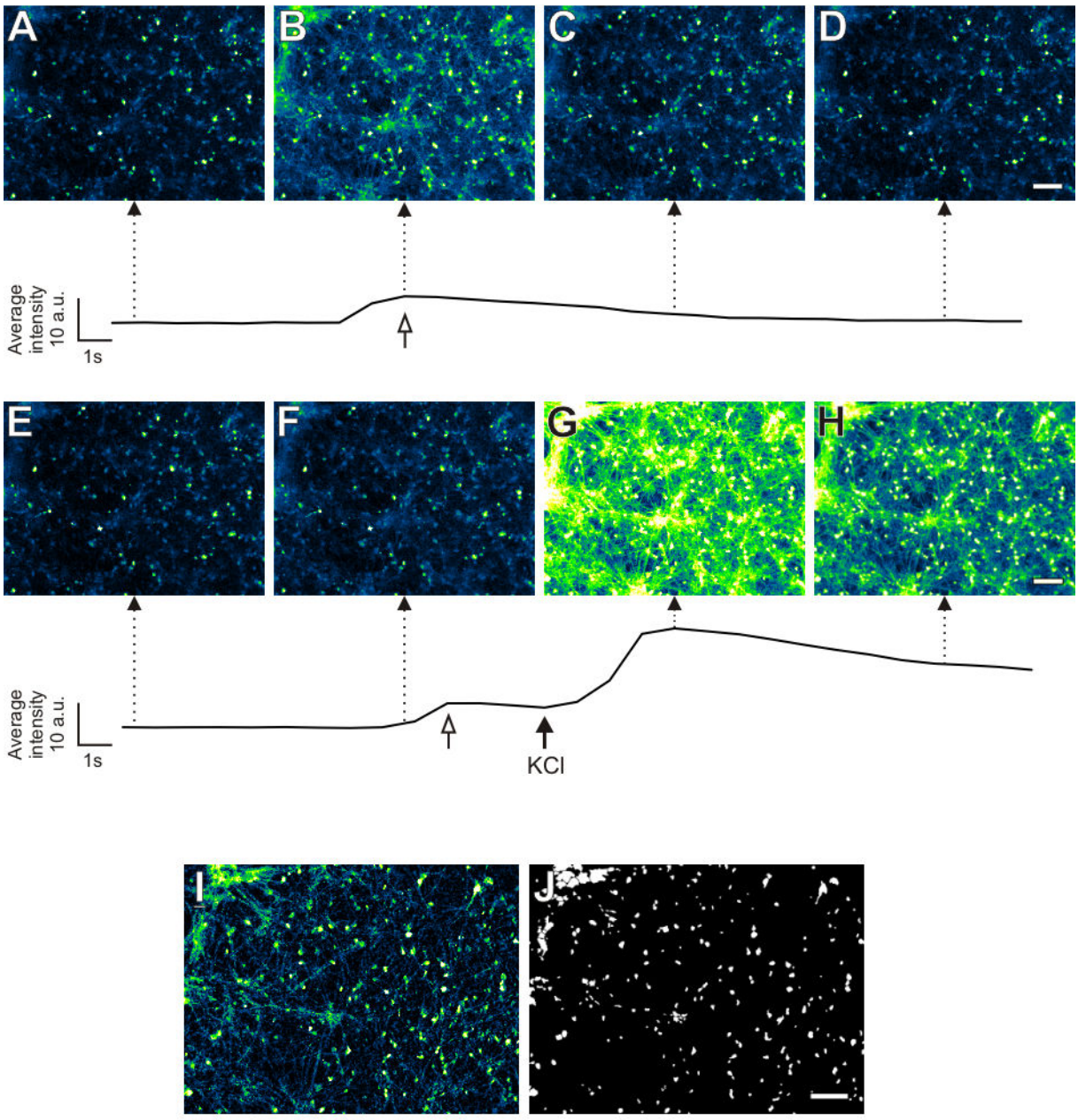

Figure 26: Defining regions of interest in calcium imaging of human iPSC derived neurons.
A: Baseline fluorescence of human iPSC derived neuronal network. **B:** Peak Ca^{2+} signal during a spontaneous synchronous network burst. **C, D:** Decay of Ca^{2+} signal. **E, F:** Baseline fluorescence. **G:** Peak of Ca^{2+} signal response to 40 mM K^{+} treatment. **H:** Decay of Ca^{2+} signal. **I:** Maximum projection of first derivation of Ca^{2+} signal induced by K^{+} depolarization. **J:** Regions of interest derived from I by thresholding. Scale bars = 100 µm, total average intensity is plotted below the images, open arrows = spontaneous synchronous network bursts.

The resulting traces (Figure 27A) were still in arbitrary units and it was often impossible to apply a threshold for burst detection because of drifts in the baseline (Figure 27C). Hence the output table was loaded into RStudio to calculate the ΔF/F signal (adapted from Jia et al., 2011; see 6.4.2 Synchronous burst detection from calcium imaging data). The mean of all

individual ΔF/F traces was calculated and bursts were defined as events that positively crossed a threshold of 0.006 ΔF/F (Figure 27E). Frequency of bursts was calculated as number of bursts per minute and statistical n represents the individual coverslip/network.

In summary, Ca^{2+} imaging of human iPSC derived neural cultures can be used to identify neuronal network bursts and their frequency from a wide range of networks. In the following, first data were obtained in glia+ networks that showed synchronous networks bursts.

3.1.3.1 Effects of removal of magnesium ions on synchronous network bursts

The first data from Ca^{2+} imaging showed, that glia+ cultures were capable to generate spontaneous synchronous network bursts. However, not every tested network showed this type of activity. To increase the number of active cultures, an epilepsy model was applied which is used in mouse models to induce excessive synchronous firing of bursts (Sombati and Delorenzo, 1995). This model deprives Mg^{2+} ions from the extracellular solution to activate NMDA receptors which then enhance synaptic transmission and excitability leading to synchronous network bursts.

By Mg^{2+} ion removal from the imaging buffer, the number of active networks was increased, while there was no effect on synchronous network burst frequency (Figure 27). In the following experiments, Mg^{2+} free solution was used to characterize the synchronous network bursting behavior.

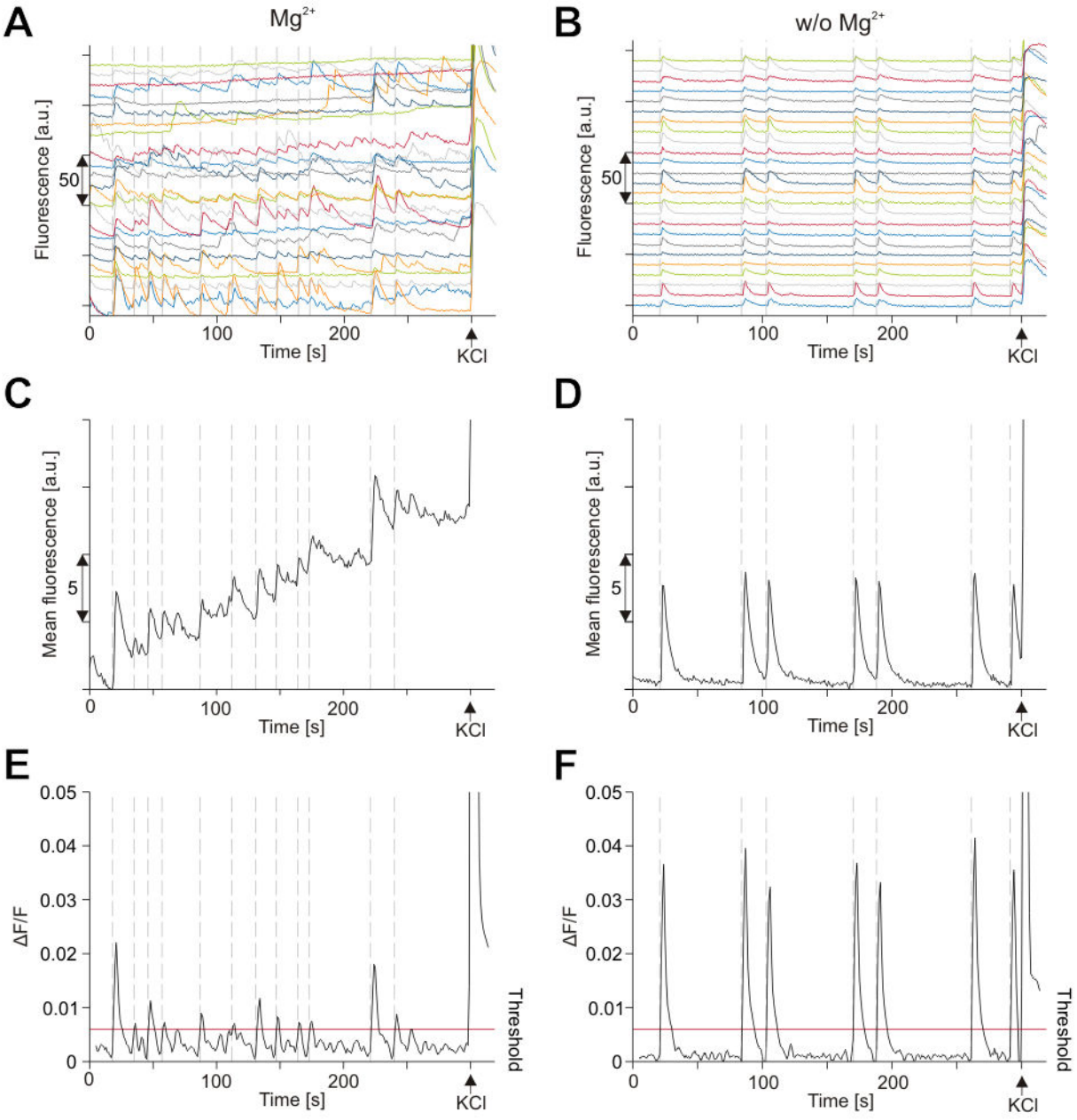

Figure 27: Spontaneous synchronous network bursts in human iPSC derived neurons in the presence and absence of magnesium ions.
Ca^{2+} imaging of human neuronal networks. **A:** Example single cell ROI traces of Ca^{2+} imaging data with Mg^{2+} containing buffer (0.75 mM). **B:** Example single cell ROI traces of Ca^{2+} imaging data with Mg^{2+} free buffer. **C, D:** Mean ROI fluorescence (single cell averaged) of networks in Mg^{2+} containing (C) and in Mg^{2+} free (D) buffer. **E, F:** Mean ΔF/F signal of networks in Mg^{2+} containing (E) and in Mg^{2+} free (F) buffer. **T**ransients that positively crossed the threshold (red line) were defined at synchronous network bursts. Vertical dashed gray lines mark detected bursts. At 300 s, extracellular KCl concentration was increased to 40 mM.

3.1.3.2 Dependence of synchronous network bursts on action potentials and synaptic transmission

To test, whether synchronous network bursts were dependet on APs in human iPSC derived cultures, active cultures were treated with TTX (1 µM), to completely block APs. Indeed, treatment with TTX inhibited all synchronous network bursts in three independent active networks (Figure 28). Individual cell traces showed no Ca^{2+} signals at all, indicating that all Ca^{2+} signals observed in this study were generated by APs (Figure 28B).

Synchronizing a network requires synaptic transmission between the different neurons in the network. To verify this and to find out which types of synapses are involved in the generation of synchronous network bursts, synapse dependence was assessed with different inhibitors of postsynaptic receptors.

First, NBQX and AP5 were used to block AMPA receptors and NMDA receptors, respectively, thus inhibiting all excitatory glutamatergic synaptic transmission (Figure 29). In three independent synchronously active networks, NBQX (10 µM) and AP5 (10 µM) blocked all synchronous network bursts while leaving single neurons capable of generating Ca^{2+} signals, as evident from single traces, where some neurons still showed activity (Figure 29B).

To block GABA-ergic transmission, the $GABA_A$ receptor antagonist gabazine (10 µM) was used. Gabazine did not have a clear effect on synchronous network bursts, as well as on single neuron signals in three independent networks as both were largely unchanged after gabazine treatment (Figure 30A-F). A slight trend to a reduced synchronous burst frequency from 7.1 ± 0.8 bursts/min to 4.9 ± 0.5 bursts/min was observed after gabazine treatment ($n = 3$), however this effect was not significant (Figure 30G, H). Together with the effect of AP5 and NBQX addition, this indicates that synchronous burst activity is solely dependent on excitatory synaptic transmission at the maturational state studied, and that GABA-ergic synaptic transmission is not necessary to maintain neuronal activity and synchronicity.

To test the dependence of synchronous network bursts on presynaptic vesicle release, Ca^{2+} imaging experiments were conducted with different extracellular Ca^{2+} concentrations in the imaging buffer (Figure 31). Each network was first tested for activity under default Ca^{2+} concentration of 1 or 1.5 mM and without Mg^{2+}. Inactive networks were not used further. In active networks, concentrations of 0.5, 1.5, 2, 5 and 10 mM $CaCl_2$ were tested in a

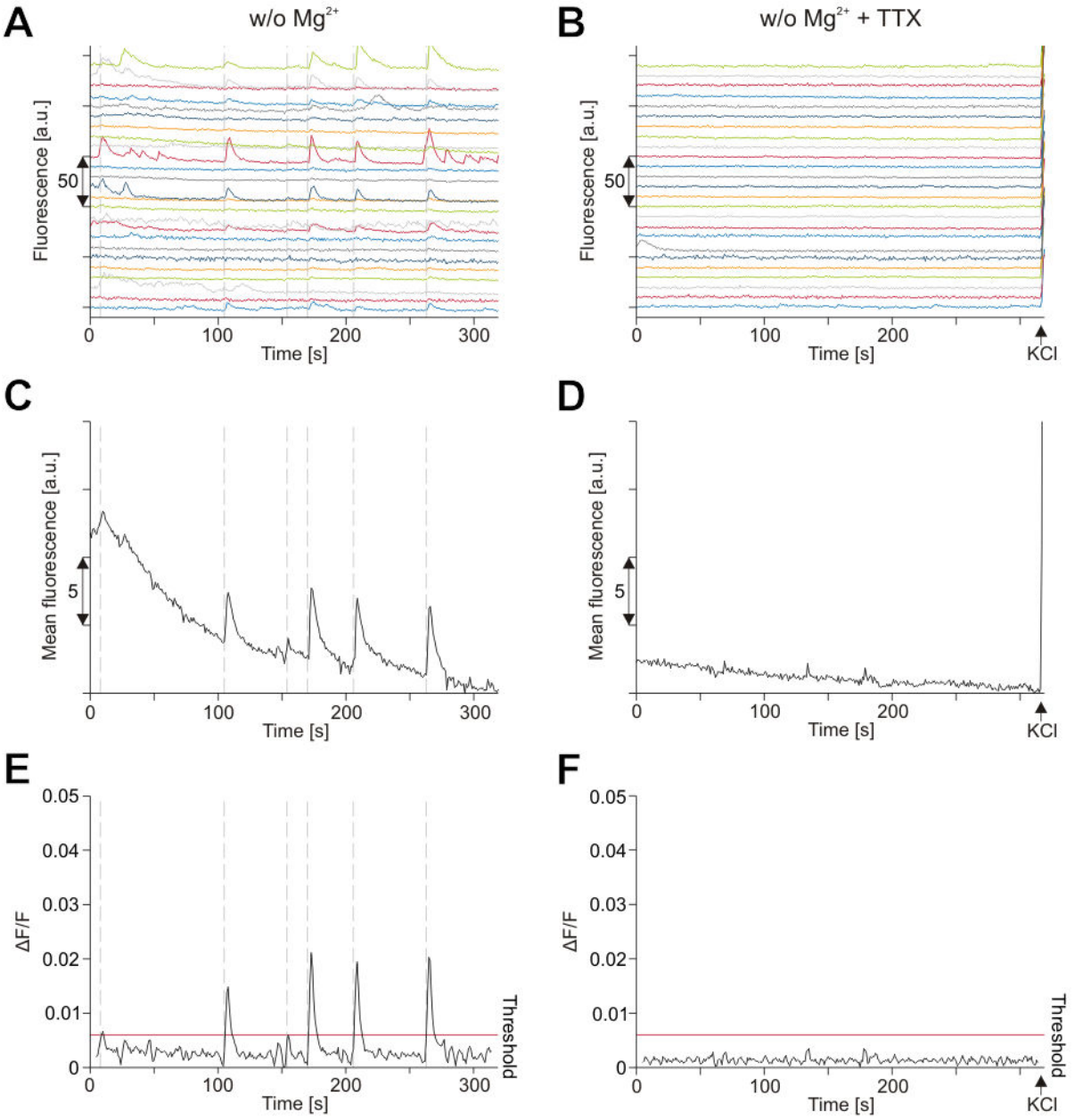

Figure 28: Neuronal calcium ion signals are blocked by TTX.
Ca^{2+} imaging of a human iPSC derived neuronal network in Mg^{2+} free buffer. **A:** Example single cell ROI traces of Ca^{2+} imaging data before TTX treatment. **B:** Example single cell ROI traces of Ca^{2+} imaging data after TTX (1 µM) addition. **C, D:** Mean ROI fluorescence (single cells averaged) of the network before (C) and after (D) TTX treatment. **E, F:** Mean ΔF/F signal of the network before (E) and after (F) TTX treatment. Transients that positively crossed the threshold (red line) were defined as synchronous network bursts. Vertical dashed gray lines indicate detected bursts. In the end of the experiemnt, extracellular KCl concentration was increased to 40 mM at 310 s.

randomized fashion (Figure 31D, E). Decreasing the Ca^{2+} concentration from standard level of 1.5 mM to 0.5 mM resulted in a significant reduction of synchronous network burst frequency from 4.0 ± 0.8 bursts/min (n = 4) to 1.2 ± 0.7 bursts/min (n = 6, $p < 0.05$). Reduction to 1 mM Ca^{2+} did not show a significant effect, although a trend to a reduced frequency was observed

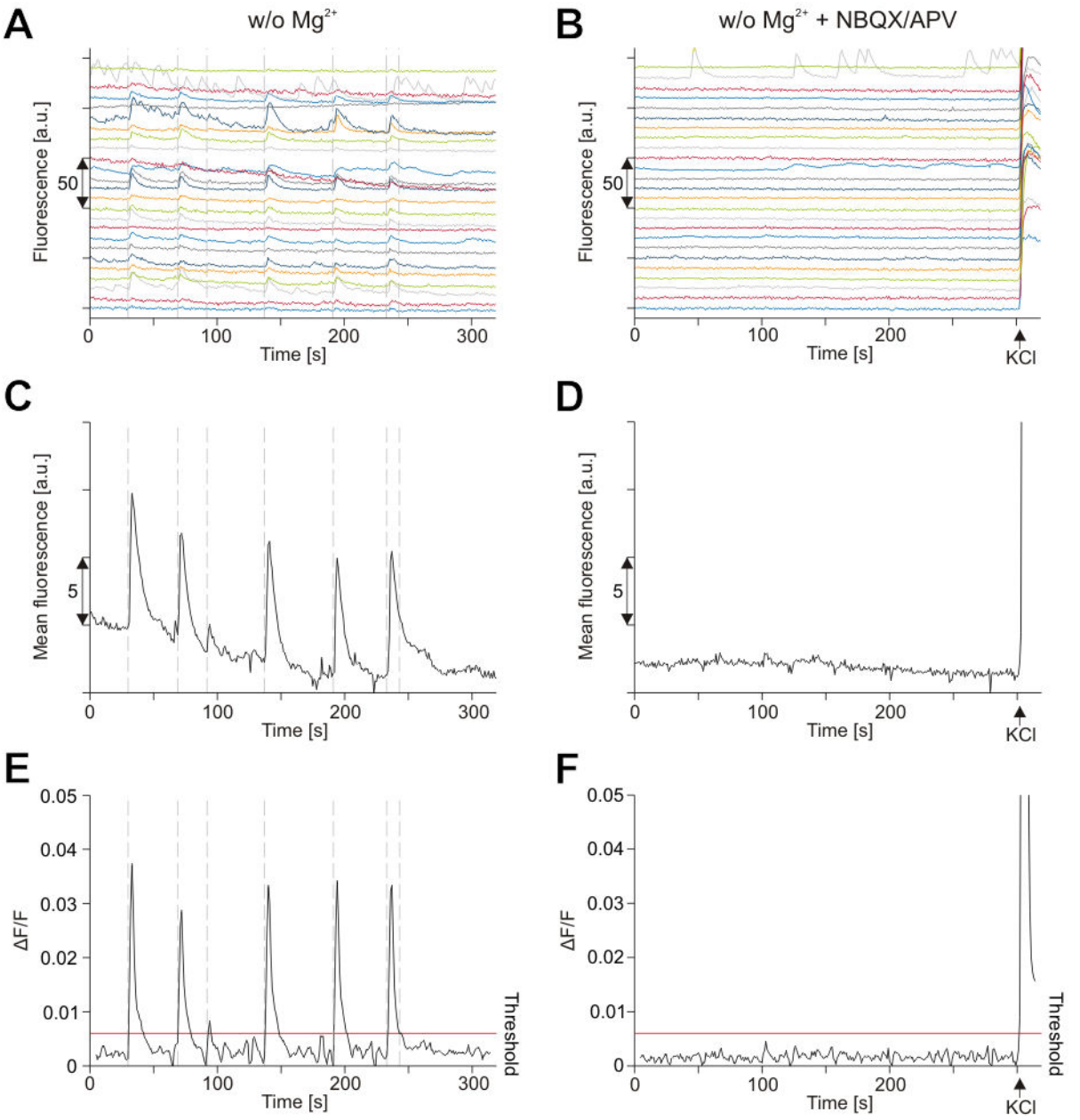

Figure 29: Synchronous network bursts are blocked by AP5 and NBQX.
Ca^{2+} imaging of a human neuronal network in Mg^{2+} free buffer. **A:** Example single cell ROI traces of Ca^{2+} imaging data before AP5 and NBQX treatment. **B:** Example single cell ROI traces of Ca^{2+} imaging data after AP5 (10 µM) and NBQX (10 µM) treatment. **C, D:** Mean ROI fluorescence of the network before (C) and after (D) AP5 and NBQX treatment . **E, F:** Mean ΔF/F signal of the network before (E) and after (F) AP5 and NBQX treatment. Transients that positively crossed the threshold (red line) were defined as synchronous network bursts. Vertical dashed gray lines indicate detected bursts. In the end of the experiemnt, extracellular KCl concentration was increased to 40 mM at 300 s.

(n = 5). Interestingly, increasing the Ca^{2+} concentration to 2 mM also decreased synchronous network burst frequency significantly to 1.1 ± 0.6 bursts/min ($n = 5$, $p < 0.05$). Further increment to 5 and 10 mM Ca^{2+} induced an even stronger reduction of synchronous network bursts to 0 bursts/min (n = 5) and 0.07 ± 0.07 bursts/min (n = 3), respectively ($p < 0.001$ and

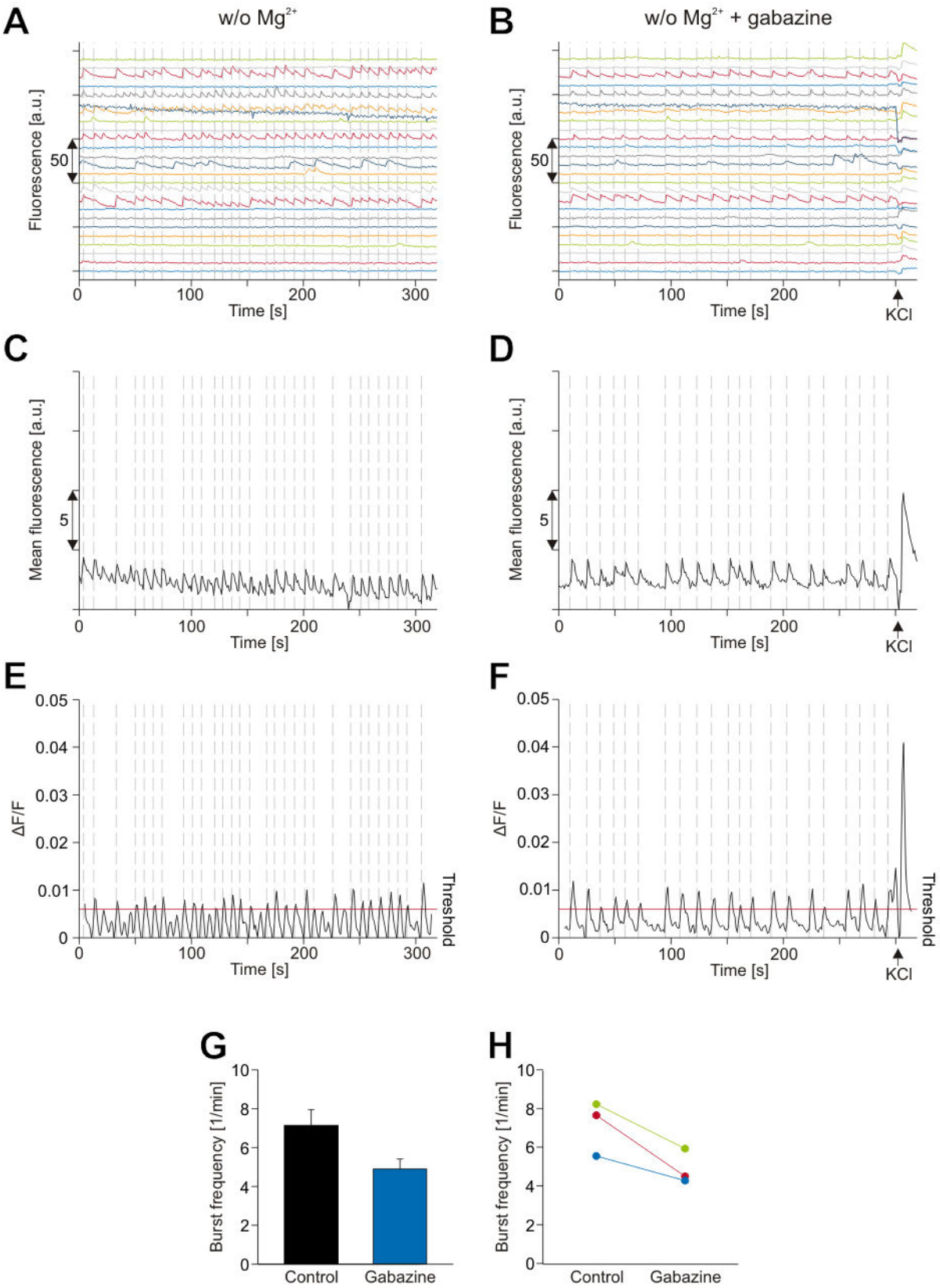

Figure 30: Effect of gabazine on neuronal calcium ion signals.
Ca^{2+} imaging of a human iPSC derived neuronal network in Mg^{2+} free buffer. Legend continued on next page.

Figure 30 legend continued: A: Example single cell ROI traces of Ca^{2+} imaging data before gabazine treatment. **B:** Example single ROI traces of Ca^{2+} imaging data after gabazine (10 µM) treatment. **C, D:** Mean ROI fluorescence of the network before (C) and after (D) gabazine treatment. **E, F:** Mean ΔF/F signal of the network before (E) and after (F) gabazine treatment. Transients that positively crossed the threshold (red line) were defined as synchronous network bursts. Vertical dashed gray lines mark detected bursts. In the end of the experiment, extracellular KCl concentration was increased to 40 mM at 300 s. **G:** Synchronous burst frequency before and after gabazine treatment (n = 3), bars and error bars represent means and standard errors of the mean, respectively. **H:** Single network values corresponding to G. No significant effect was found with paried t-test.

$p < 0.01$). This indicates an effect on excitability of negative surface charge screening with increasing Ca^{2+} concentrations.

In summary, synchronous network Ca^{2+} signals are generated by APs and depend on excitatory glutamatergic transmission, whereas GABA-ergic transmission is not necessary for synchronous network bursts. The used default Ca^{2+} concentration of 1.5 mM is optimal as it maximizes burst frequency and both, higher and lower Ca^{2+} concentrations reduced the synchronous network burst frequency.

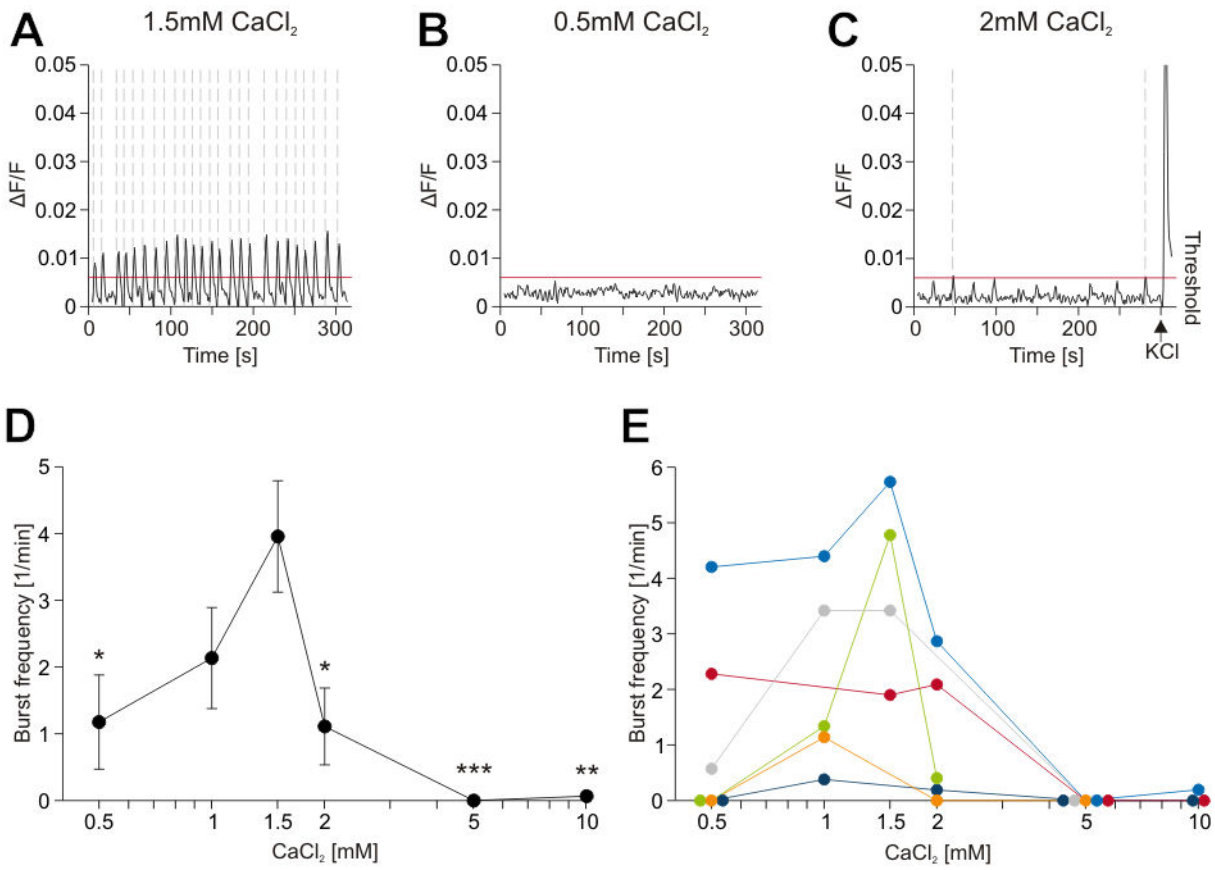

Figure 31: Synchronous network bursts are dependent on extracellular calcium ion concentration.
Networks that were active at 1 or 1.5 mM extracellular Ca^{2+} were further tested with 0.5 (n = 6), 1 (n = 5), 1.5 (n = 4), 2 (n = 5), 5 (n = 5) and 10 mM (n = 3) Ca^{2+} concentrations in a randomized fashion. **A:** Mean ΔF/F signal of an example network at default 1.5 mM extracellular Ca^{2+}. **B:** Mean ΔF/F signal of the network at reduced 0.5 mM extracellular Ca^{2+}. **C:** Mean ΔF/F signal of the same network at increased 2 mM extracellular Ca^{2+}. In the end of experiment, extracellular KCl concentration was increased to 40 mM at 300 s. Transients that positively crossed the threshold (red line) were defined at synchronous network bursts. Vertical dashed gray lines indicate detected bursts. **D:** Synchronous network burst frequency versus extracellular Ca^{2+} concentration (log scale). Points and error bars represent means and standard errors of the mean, respectively, * $p < 0.05$, ** $p < 0.01$, *** $p < 0.001$, one way repeated measures ANOVA with Holm-Sidak method versus 1.5 mM Ca^{2+}. **E:** Single network corresponding to D.

3.1.3.3 Effects of the presence of glial cells on synchronous network bursts

To asses the effects of glial cells on network function, synchronous network bursts were compared between glia+ and glia- cultures. Removing extracellular Mg^{2+} ions from the same networks enabled the analysis of the potential of the cultures to generate synchronous network bursts (Figure 32). Although the number of networks showing synchronous network bursts was almost doubled from 25% in Mg^{2+} buffer (0.75 mM) to 42.9% in Mg^{2+} free buffer (Figure 32C), the frequency was not changed (0.79 ± 0.50 bursts/min compared to 0.84 ± 0.45 bursts/min) by this treatment in glia+ cultures (n = 14, Figure 32A). However, in glia-

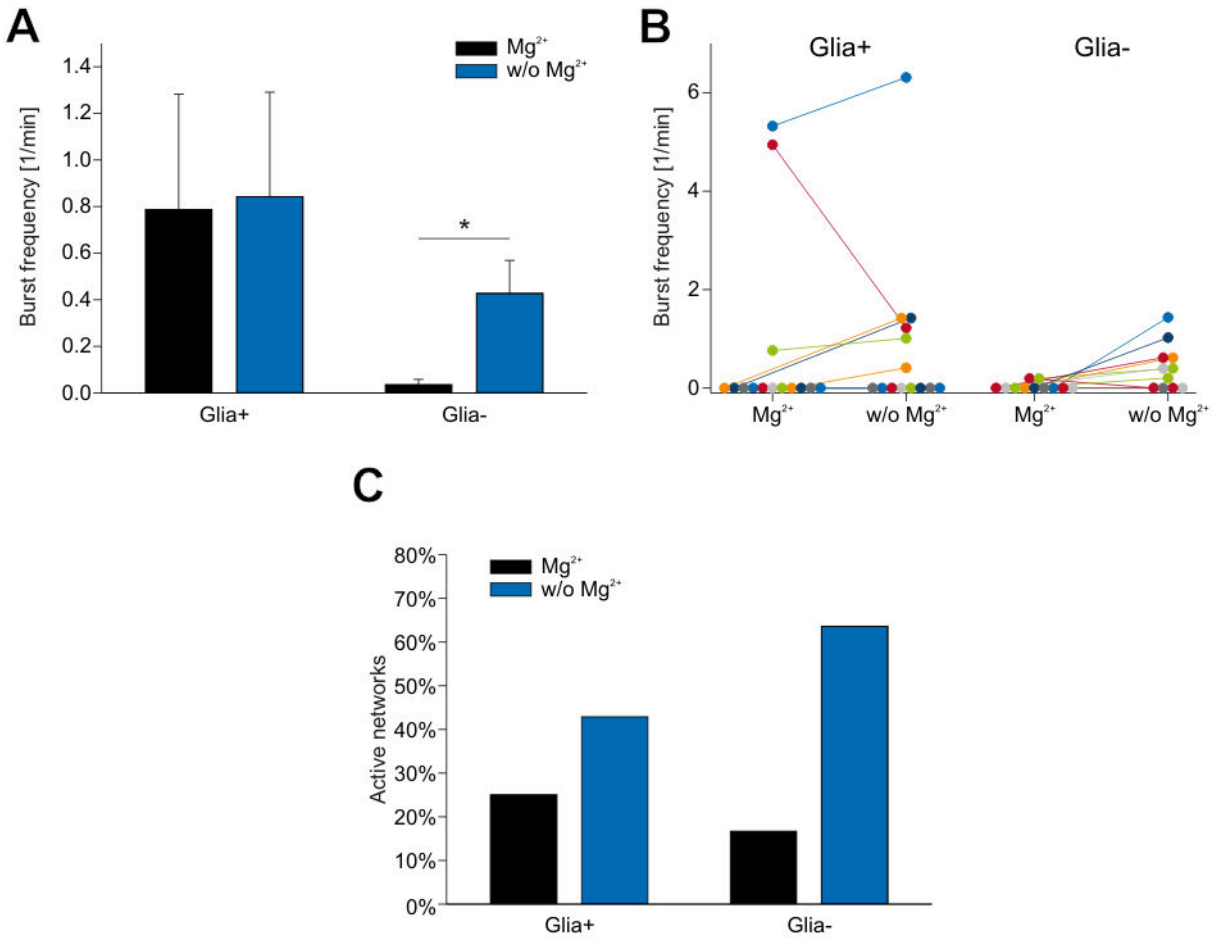

Figure 32: Effect of glial cells on spontaneous synchronous network bursts.
A: Synchronous network burst frequency with (0.75 mM) and without (w/o) extracellular Mg^{2+} (n = 14) in glia+ and glia- cultures (n = 11). Bars and error bars represent means and standard errors of the mean, respectively, * $p < 0.05$, paired t-test. **B:** Single network values corresponding to A. **C:** Ratio of active per total networks with and without Mg^{2+} in glia+ and glia- cultures.

networks, the very low basal frequency of 0.035 ± 0.023 bursts/min was significantly increased to 0.427 ± 0.142 bursts/min ($n = 11$, $p < 0.05$), making them as active as glia+ cultures. The ratio of active glia- networks was increased by almost four times from 16.7% to 63.6% by Mg^{2+} removal.

In summary, glia- cultures showed very low activity in Mg^{2+} containing buffer and there was a difference between glia+ and glia- cultures in the spontaneous generation of synchronous network bursts, pointing to a less excitable network in glia- cultures.

3.2 Effects of amyloid-β on synaptic transmission

Synaptotoxic effects of Aβ, the hallmark peptide of Alzheimer's disease, have been shown several times previously in mouse models. However, up to now its mechanisms of action are not yet completely understood and the conditions that are necessary to develop Alzheimer's disease, especially the sporadic form are not yet known, because mouse models differ from the the human system and the diseases phenotype occurs late in life. In this study, Aβ addition to the estabished mature human neuronal networks was used as a human disease model, simulating the increased abundance of Aβ peptides in diseased human brains. In addition to synapses, direct effects of Aβ on voltage dependent Na^+ channels underlying excitability were analyzed.

Because synapses are highly plastic structures that change function and structure according to neuronal activity, synaptotoxic effects of Aβ might be dependent on the plasticity state of the synapse. To check this hypothesis, Aβ in form of 7PA2 conditioned medium was applied to mouse neurons with different activity states.

3.2.1 Effects of synthetic amyloid-β on human neurons

After characterization of the human neuronal networks, these cultures were tested for suitability for human disease modeling by application of synthetic amyloid-β. Glia- cultures were used, because they are more homogenous and exclude potentially protective effects of glial cells.

3.2.1.1 Characterization of the synthetic amyloid-β preparation

The ability of Aβ to aggregate in aqueous solutions makes it necessary to characterize the state of aggregation in a given preparation, and to estimate its final concentration. In this study, native PAGE in combination with Western blot was used to analyze the composition of the Aβ preparation to avoid strong SDS effects on higher oligomers. A synthetic Aβ preparation in NBNS21S was used. This preparation contained a significant amount of monomers, as evident from native PAGE Western blot (Figure 33A). However, as estimated from Western blot comparison the amount of Aβ was approximately 100 times less than in the control that was dissolved directly in HFIP/DMSO (consisting of monomers). In both preparations, some aggregates that were too large to enter the gel got stuck in the wells of the

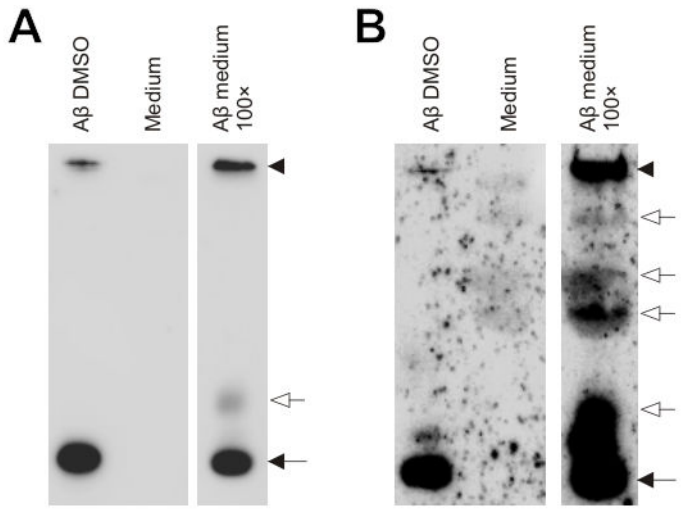

Figure 33: Western blots of synthetic amyloid-β dissolved in DMSO or in culture medium. Native PAGE was followed by 4G8 immunoreactivity assay. **A:** Synthetic amyloid-β (Aβ) preparations on Western blot with short exposure time. **B:** Synthetic Aβ preparation on Western blot with high exposure time. Medium (negative control without Aβ) = NBNS21S, Aβ DMSO (monomer control) = Aβ dissolved in HFIP, evaporated by N_2 flow and then reconstituted in DMSO. Arrowhead = gel well, open arrows =oligomers, arrow = Aβ monomer, 100× amount of Aβ in medium was loaded to achieve a similar signal to Aβ in HFIP/DMSO.

gel. The negative control with only medium loaded did not show any signal. Longer exposure of Western blots revealed the presence of bands between Aβ monomer and the wells, presumably dimers and higher oligomers which were neither present in the HFIP/DMSO preparation nor in the negative medium control (Figure 33B).

In summary, the Aβ preparation used in the following experiments contained Aβ monomer and oligomers in relatively physiological, low concentrations, thus representing an Aβ "cocktail", which might be suitable for human disease modeling.

3.2.1.2 Effect of amyloid-β on voltage dependent sodium ion currents

To test, whether synthetic Aβ has a direct effect on neuronal excitability, experiments were conducted to asses voltage dependent Na^+ currents in freshly dissociated human neurons which were treated with synthetic Aβ (1 µM nominal concentration, estimated 10 nM) for 4d (addition of Aβ at 1 week post immunopanning). In patch-clamp recordings, cells were depolarized from -80 mV holding potential by pulses of 40 ms, stepwise increasing by 5 mV up to 40 mV. With K^+ currents blocked by replacement of intracellular K^+ with Cs^+, resultant current traces showed a characteristic rise of inward Na^+ current at potentials positive to -40 mV (Figure 34A, B). Peak current amplitudes peaked around 0 mV and decreased at more positive potentials. There was no significant difference between vehicle and Aβ treated cells,

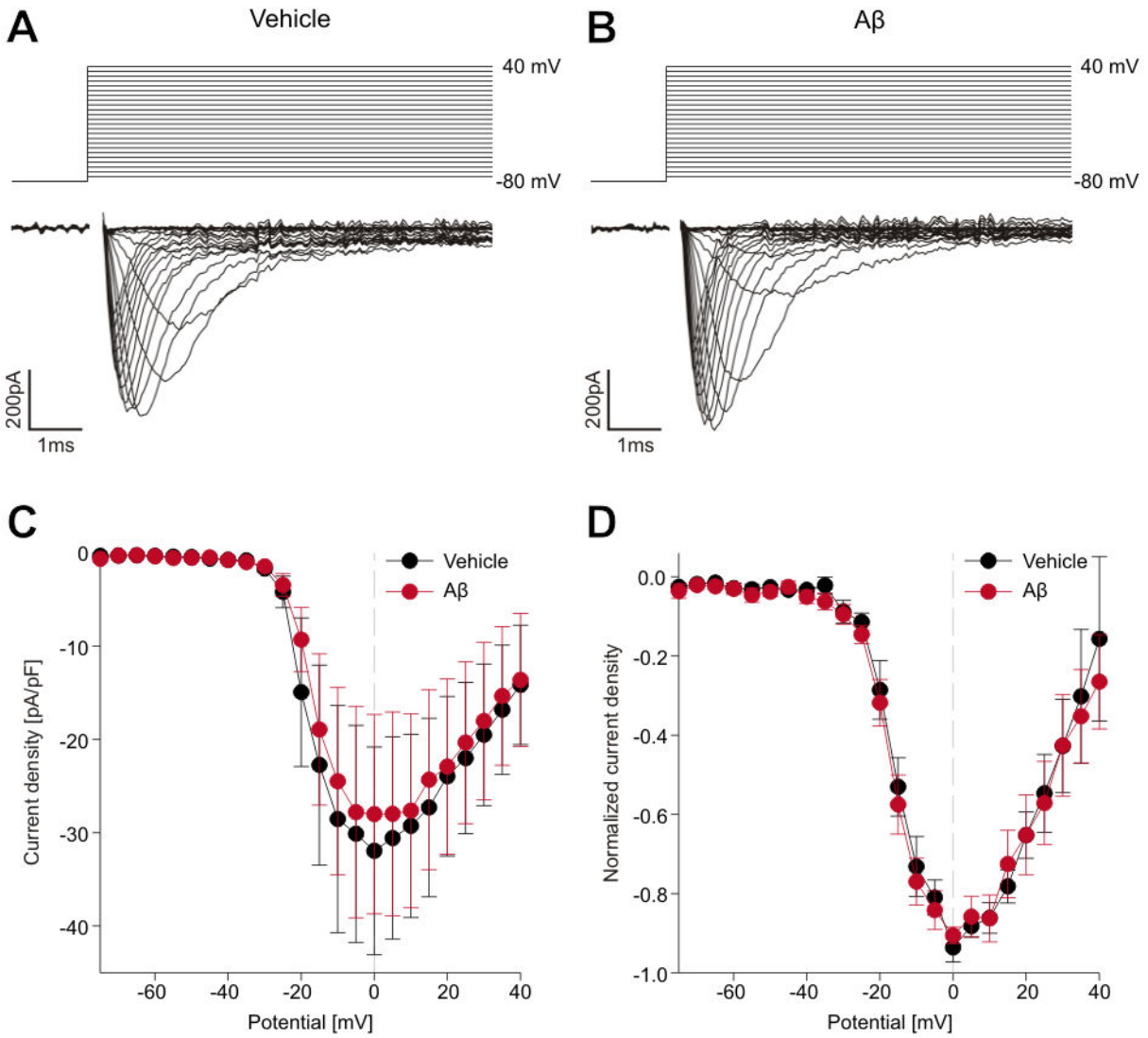

Figure 34: Effect of amyloid-β on voltage dependent sodium ion currents in human iPSC derived neurons.
Freshly dissociated human iPSC derived neurons were pretreated with amyloid-β (Aβ) for 4 d at 1 week post immunopanning and step depolarized in whole cell voltage clamp from -80 mV by pulses of 40 ms, with stepwise increase of depolarizations by 5 mV up to 40 mV. K^+ currents were blocked by replacement of intracellular K^+ with Cs^+. **A, B:** First few milliseconds of current traces from cells treated with vehicle (A) and Aβ (B) after correction for cell capacitance and leak current. **C:** Peak current densities versus clamped potentials in vehicle (n = 10) and Aβ (n = 10) treated neurons. **D:** Current densities corresponding to C, normalized to peak current density versus clamped potential. Points and error bars represent means and standard errors of the mean, respectively. No significant effect was found with two way repeated measures ANOVA.

with peak current densities at 0 mV of -31.9 ± 11.1 pA/pF in the vehicle (n = 10) and -28.0 ± 10.7 pA/pF in the Aβ (n = 10) treated cells (Figure 34C). Normalization to the peak current density in each cell did not reveal a shift of activation curves, as vehicle and Aβ treatment both peaked at 0 mV with ratios of -0.94 ± 0.04 and -0.91 ± 0.02, respectively.

Thus, synthetic Aβ treatment did not affect voltage dependent Na^+ currents in freshly dissociated human iPSC derived neurons.

3.2.1.3 Effects of amyloid-β on AMPA receptor mediated mEPSCs

As the deleterious actions of Aβ on synapses have widely been studied in mouse cultures and brain slices, synaptotoxic effects of Aβ on human iPSC derived neurons (8 weeks post immunopanning) were assessed by measurement of AMPAR receptor mediated mEPSCs using the whole cell voltage clamp technique. Glia- cultures were used to exclude a glial cell influence on Aβ effects. Aβ treatments were done for 3 d and 7 d in independent experiments prior to measurements.

There was no significant effect of Aβ on AMPA receptor mediated mEPSCs after 3 d of treatment as compared to vehicle (Figure 35). Mean mEPSC frequency was 0.24 ± 0.10 Hz in the vehicle (n = 19) and 0.26 ± 0.10 Hz in the Aβ (n = 18) treated neurons, mean amplitudes were 19.07 ± 1.21 pA in vehicle (n = 16) and 18.20 ± 1.71 pA in Aβ (n = 16) treated neurons. Cumulative frequency distributions of mEPSC amplitudes did not differ, too (Figure 35F). 50% of the mEPSC had amplitudes lower than 17.5 pA after vehicle treatment and lower than 15.5 pA after Aβ treatment.

Strikingly, after 7 d of Aβ treatment, neurons exhibited reduced mEPSC frequencies and amplitudes (Figure 36A). Quantification showed a strong trend to a reduced frequency from 0.61 ± 0.29 Hz in vehicle (n = 17) to 0.13 ± 0.05 Hz in Aβ (n = 17) treated neurons, however, without being significant (Figure 36B, C). mEPSC amplitudes were significantly reduced from 20.14 ± 1.92 pA in vehicle (n = 14) to 16.29 ± 0.56 pA in Aβ (n = 17) treated neurons ($p < 0.05$, Figure 36D, E). This amplitude reduction was also evident in the cumulative frequency distributions of mEPSC amplitudes. 50% of mEPSCs had amplitudes lower than 18.5 pA in the vehicle and 16 pA in the Aβ treated neurons (Figure 36F).

In summary, synaptotoxic effects of Aβ on human iPSC derived neurons were detectable after 7 d of Aβ pretreatment, with concentrations in the nM range, as evident from reduced mEPSC amplitudes. The absence of an effect after only 3 d of Aβ pretreatment confirmed that the observed synapse impairment might be relevant for the slowly developing human pathophysiology.

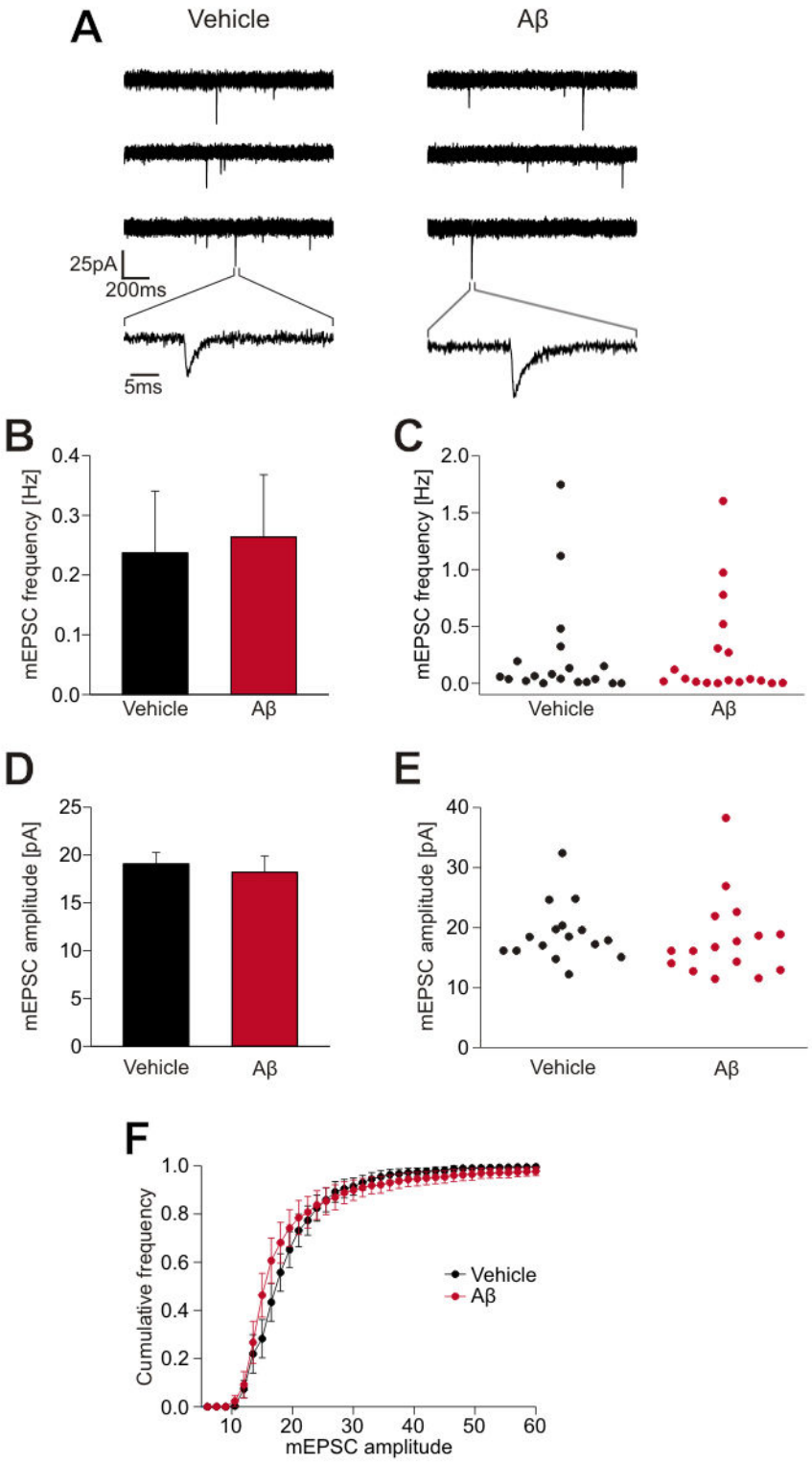

Figure 35: Effect of 3 d application of amyloid-β on AMPA receptor mediated mEPSCs in human iPSC derived neurons.
Whole cell voltage clamp at -60 mV holding potential and pharmacological isolation of AMPA receptor mediated mEPSCs by TTX (1 µM) and gabazine (10 µM). **A:** Example mEPSCs from recordings in vehicle (left) and Aβ (right) treated neurons. Inset: Enlarged single mEPSC. **B:** Frequencies of mEPSCs in vehicle (n = 19) and Aβ (n= 18) treated neurons. **C:** Single cell values corresponding to B. **D:** Amplitude of mEPSCs in vehicle (n = 16) and Aβ (n = 16) treated neurons. **E:** Single cell values corresponding to D. Bars and error bars represent means and standard errors of the mean, respectively. No significant effect was found with Student's t-test. Legend continued on next page.

Figure 35 legend continued: **F:** Cumulative frequency plot of mEPSC amplitudes, points and error bars represent means and standard errors of the mean, respectively.

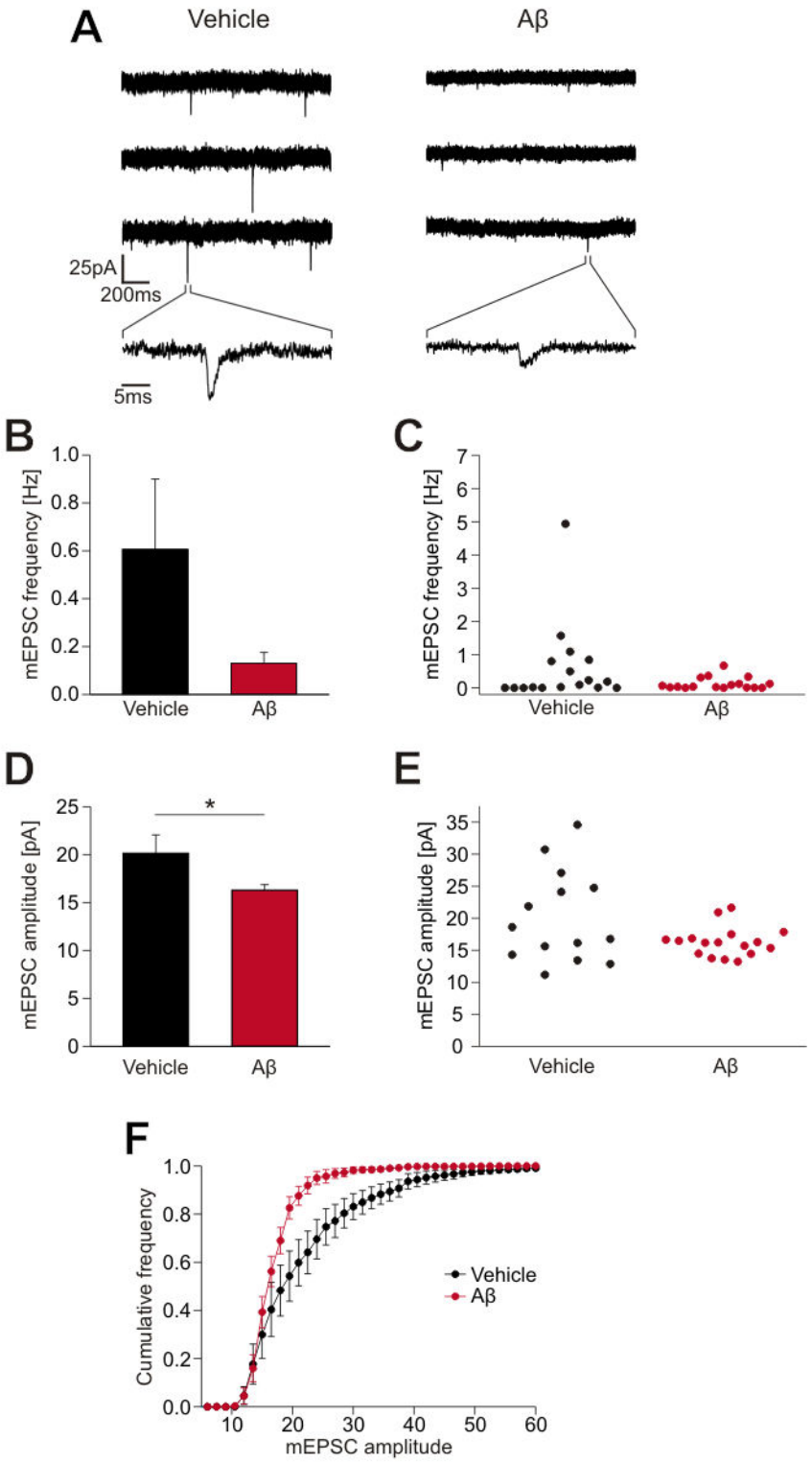

Figure 36: Effect of 7 d application of amyloid-β on AMPA receptor mediated mEPSCs in human iPSC derived neurons.
Whole cell voltage clamp at -60 mV holding potential and pharmacological isolation of AMPA receptor mediated mEPSCs by TTX (1 µM) and gabazine (10 µM). **A:** Example mEPSCs from recordings in vehicle (left) and Aβ (right) treated neurons. Inset: Enlarged single mEPSC. **B:** Mean frequency of mEPSCs in vehicle (n = 17) and Aβ (n= 17) treated neurons. **C:** Single cell values corresponding to B. **D:** Mean amplitude of mEPSCs in vehicle (n = 14) and Aβ (n = 17) treated neurons, * $p < 0.05$, Student's t-test. **E:** Single cell values corresponding to D. Bars and error bars represent means and standard errors of the mean, respectively. Legend continued on next page.

Figure 36 legend continued: F: Cumulative frequency plot of mEPSC amplitudes, points and error bars represent means and standard errors of the mean, respectively.

3.2.1.4 Effects of amyloid-β on cell viability

To verify that mEPSC effects of Aβ treatment did not arise from impaired cell viability and reduced cell density, cytotoxicity was assessed by a cell viability assay (Figure 37). Live and dead cells were stained by calcein AM and ethidium homodimer (EthD-1), respectively, and counted. After 4 d of Aβ treatment, there was no difference in the fraction of intact cells between vehicle (n = 5) and Aβ (n = 5) treated cultures, with values of 84.3 ± 1.8% and 77.6 ± 4.3%, respectively (Figure 37A, B, E, F). Also after 8 d, no difference in the fraction of intact cells between vehicle (n = 3) or Aβ (n = 5) treated cultures was found. Values were 87.3 ± 6.1% and 89.0 ± 2.9% in vehicle and Aβ treated cultures, respectively (Figure 37C, D, G, H).

In summary, no evidence of impaired cell viability or reduced cell density by Aβ treatment was found, pointing to the specificity of Aβ mediated synaptotoxicity.

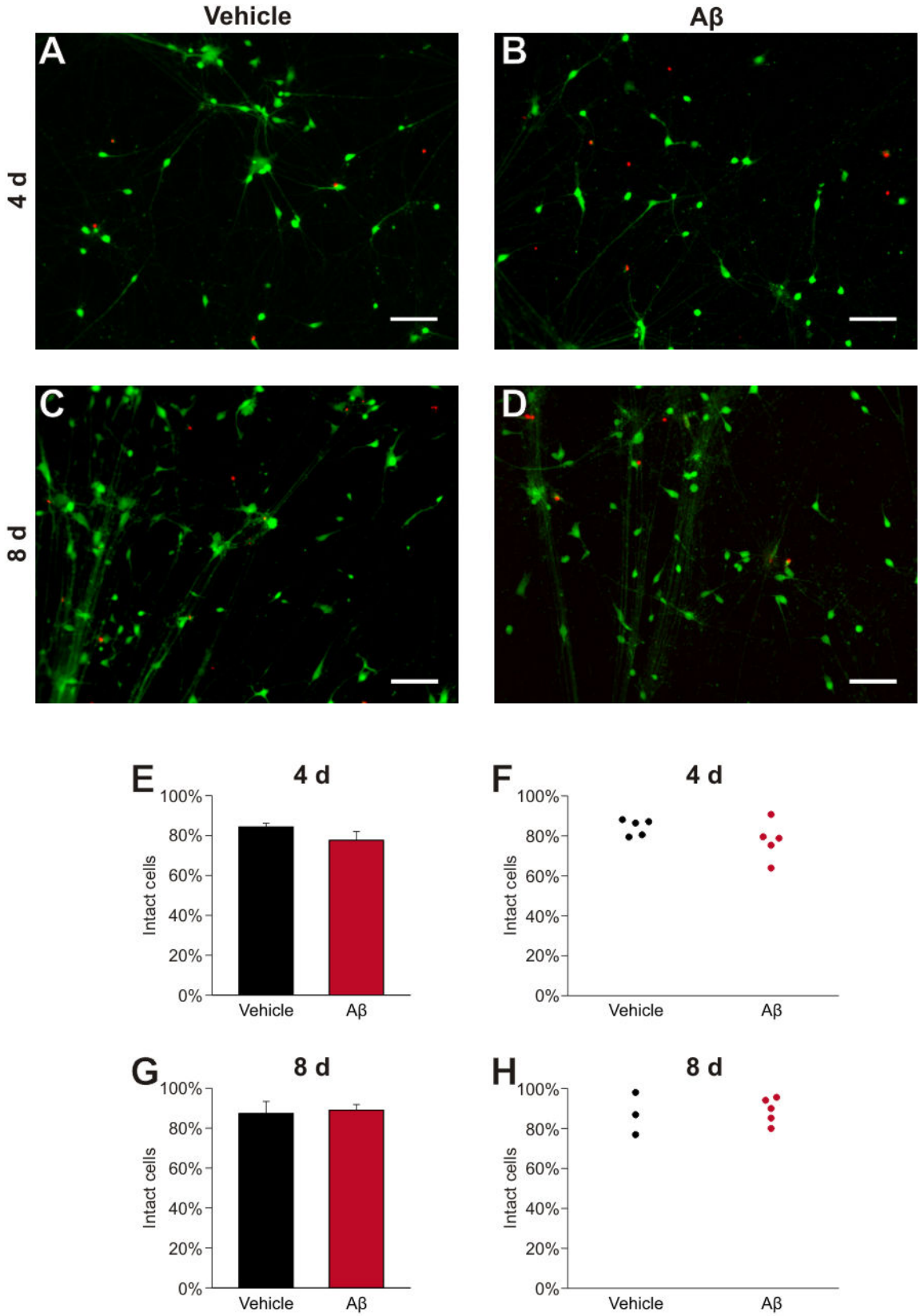

Figure 37: Effect of amyloid-β on cell viability in human iPSC derived neurons.
A-D: Cell viability assay of 4 d vehicle (A), 4 d Aβ (B), 8 d vehicle (C) and 8 d Aβ (D) treated cultures. Intact cell somata are labeled by calcein AM (green), dead cell condensed nuclei are labeled by ethidium homodimer (red), scale bar = 100 µm. Legend continued on next page.

Figure 37 legend continued: E: Fraction of intact cell somata per total cells after 4 d treatment with vehicle (n = 5) and Aβ (n = 5). **F:** Single coverslip values corresponding to E. **G:** Fraction of intact cell somata per total cells after 8 d treatment with vehicle (n = 3) and Aβ (n = 5). **H:** Single coverslip values corresponding to G. Bars and error bars represent means and standard errors of the mean, respectively. No significant effect was found with Student's t-test.

3.2.2 Activity dependence of synaptotoxicity mediated by amyloid-β peptides

Synaptotoxic effects of Aβ might be dependent on the plasticity state of the synapse, which is strongly dependent on previous neuronal activity. Different states of synaptic plasticity are characterized by different synaptic proteome thus might have different vulnerabilities to Aβ. Therefore, this work seeked to evaluate activity dependence of synaptotoxic Aβ effects in mature mouse neurons by creating different states of activity with addition of TTX, and subsequent measurements of AMPA receptor mediated mEPSCs. Before electrophsiological recordings, TTX was applied to the culture medium of primary hippocampal mouse nerons and glial cells for a total time of 4d before they were additionally treated with Aβ peptides in the form of 7PA2 supernatant or vehicle for another 4 d (Figure 38A). Thus, total treatment time was 8 d.

The activity deprivation by TTX resulted in synaptic up-scaling as evident from an increase in AMPA receptor mediated mEPSCs amplitudes (Figure 38B+C). Mean amplitudes increased from 11.46 ± 0.53 pA in control (n = 41) to 15.40 ± 0.85 pA in TTX (n = 38) treated cells. mEPSC Amplitudes of Aβ (7PA2 supernatant) treated cells were not significantly different from vehicle treated cells under none of the two activity conditions with 10.91 ± 0.41 pA in control (n = 40) and 14.56 ± 0.84 pA in TTX treated cells (n = 39).

Five out of six preparations showed an up-scaling of mEPSC amplitudes upon TTX treatment as expected from literature, whereas one culture surprisingly did not show this effect (Figure 38D). This finding was used to split cells into cells from responding and non-responding cultures. This reanalysis of the data resulted in opposite effects of 7PA2 treatment in TTX treated cells (Figure 38E). In cultures that exhibited up-scaling after TTX treatment, 7PA2 supernatant had a negative effect on mEPSC amplitudes, significantly reducing it from 17.20 ± 1.16 pA in TTX/vehicle condition (n = 21) to 13.12 ± 0.89 pA in TTX/7PA2 condition (n = 22, $p < 0.01$). The non responding culture showed an inverse effect of increasing amplitudes from 12.34 ± 1.21 pA (n = 12) after TTX/vehicle to 17.45 ± 1.74 pA after TTX/7PA2 treatment (n = 13, $p < 0.05$).

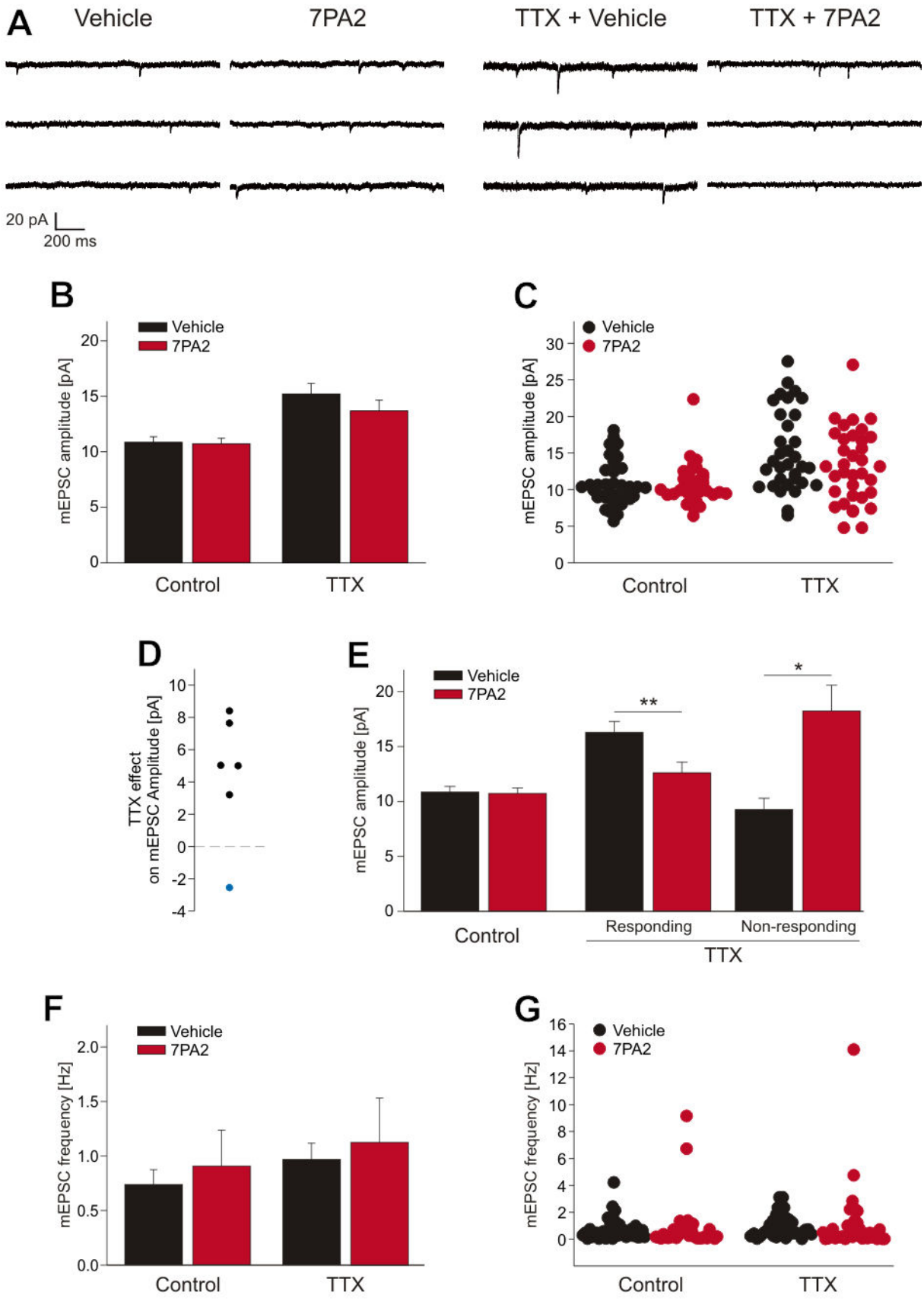

Figure 38: Synaptotoxicity of amyloid-β is activity dependent.
Legend on next page.

Figure 38 legend: Whole cell voltage clamp at -60 mV and pharmacological isolation of AMPA receptor mediated mEPSCs of hippocampal mouse neurons by TTX and gabazine. **A:** Example mEPSCs from neurons treated 4 d with vehicle (left), 7PA2 supernatant (second from left), 4 d with TTX + 4 d with vehicle (third from left) and 4 d with TTX + 4 d with 7PA2 supernatant (right). **B:** Amplitudes of mEPSCs in vehicle (n = 41), 7PA2 supernatant (n = 40), TTX + vehicle (n = 38) and TTX + 7PA2 supernatant (n = 39) treated neurons. **C:** Single cell values corresponding to B. **D:** Mean effect size of TTX pretreatment in all used preparations, given as difference in mean mEPSC amplitudes between control and TTX treated sister cultures. Positive values represent increases in amplitudes after TTX treatment. The preparations below (blue) and above (black) 0 pA effect size were regarded as non-responding and responding, respectively. **E:** Amplitudes of mEPSCs from B sorted into responding (TTX/vehicle: n = 21 and TTX/7PA2 supernatant: n = 22) and non-responding (TTX/vehicle: n = 12 and TTX/7PA2 supernatant: n = 13) cultures by data from D, * $p < 0.05$, ** $p < 0.01$, Student's t-test. **F:** Frequencies of mEPSCs in vehicle (n = 41), 7PA2 supernatant (n = 40), TTX + vehicle (n = 38) and TTX + 7PA2 supernatant (n = 39) treated neurons. **G:** Single cell values corresponding to F. Bars and error bars represent means and standard errors of the mean, respectively.

mEPSC frequencies, however were not different (Figure 38F, G). In control condition, frequency of vehicle treated cells was 0.71 ± 0.12 Hz (n = 41) as compared to 0.77 ± 0.26 Hz in 7PA2 supernatant treated cells (n = 40). Under TTX conditions, the frequency of vehicle treated cells was 0.87 ± 0.13 Hz (n = 38), whereas frequency of 7PA2 supernatant treated cells was 1.08 ± 0.37 Hz (n = 39).

In summary, the effects of Aβ peptides on synapses in mature mouse neurons appeared to be dependent on the plasticity state of the synapse, as suggested by differences in mEPSC amplitudes. Interestingly, scaled up synapses might be more vulnerable.

4 Discussion

4.1 Influence of intrinsic glial cells on the functional maturation of human neuronal networks

The lack of a human preparation and the drawbacks of post mortem material for basic research and disease modeling have made the use of animal models the major and first choice method of mechanistic analysis for example in the field AD. But problems arising from genomic and proteomic differences between animal models and humans have often been recognized in late phase clinical trials. Drugs that were developed with the help of animal models sometimes failed in patients even though they worked well in animal trials (Schnabel, 2008). These problems make human systems invaluable tools for medicine as well as for basic research. The advent of the iPSC technology (Takahashi & Yamanaka, 2006) made it possible to develop human culture systems, because human iPSCs theoretically can be differentiated into any type of cell. In neuroscience, iPSCs are now widely used to differentiate them into neurons of different types and these differentiated neurons are widely used for disease modeling (Inoue et al., 2014). However, as maturation of cultured human neurons seems to be much slower than in primary murine cultures, functional maturity is highly debated and sometimes not very well assessed in these cultures. Especially the formation of synapses and the development of spontaneous network activity is rarley reported with statistical certainty as it takes long culture periods for these neuronal functions to develop. As data from mouse cultures suggest, glial cells might speed up this differentiation process and lead to more mature neurons and networks (Böhler et al., 2007; Allen, 2013). Indeed, there is data on human iPSC derived neurons showing the positive influence of cultivation with murine astrocytes on differentiation and spontaneous network activity (Tang et al., 2013; Odawara at al., 2014). However, up to now there are no detailed studies on a solely human co-culture system. The advantage of such a system would be the consistency of the co-culture not only from the genetic background, but also from a developmental point of view. Especially for future use in disease modeling, for example by using patient derived cells, this culture system would have the advantage of carrying the same potential disease relevant genes in both, neurons and glial cells, so that the model more precisely resembles the situation *in vivo*.

In this study, a human neuron-glia co-culture with intrinsically differentiated astrocytes from the same iPSC origin was analysed to asses the influence of human glial cells on these

neurons and their networks. A comparative analysis of neuronal functions in glia enriched and largely glia free cultures was conducted. Cellular composition of these cultures was analyzed by immunocytochemistry and in depth electrophysiological characterization was applied to neuronal subpopulations to examine the influence of glial cells on neuronal function. Finally, as a fast and easy measure of integrative network function, a Ca^{2+} imaging based on Fluo-4 method was established to monitor synchronous network bursts of neurons. In summary, this work provided a wide range of data on neuronal function in these human iPSC derived networks and a basis for the comparative study of glial cell influence on neuronal differentiation and functional maturation.

4.1.1 Establishment of a co-culture of human neurons with intrinsic glial cells and of a glia free control culture

To create a human co-culture system of neurons with intrinsic glial cells, human iPSCs were differentiated with a long term protocol through an EB stage to generate NPCs first and then immature neurons. An immunopurification step with NCAM antibody called immunopanning was used to purify cells of neuronal lineage from undifferentiated cells (Nieweg et al., 2015). Small molecule treatment with DM and PD after immunopurification ensured further differentiation of precursor cells into neural lineage that were still present despite the immunopurification technique. As a parallel control culture, immature neurons immunopurified from EBs were treated with Ara-C, which kills all proliferating cells, and were then re-dissociated to achieve neuronal densities comparable to DM and PD treated cultures. Resulting neural cultures were kept for at least eight weeks post immunopanning to ensure morphological and functional maturation before conducting experiments.

Cellular composition of the human neural cultures was analyzed by immunocytochemistry to verify the similarity of the neuronal populations and the differences in glial cell content. The generation of a glial cell containing neuronal preparation by small molecule treatment was successful, as evident from the positive immunostaining for GFAP which was almost completely absent in the Ara-C treated cultures (Figure 13). This result led to the naming of the cultures as glia+ for the glia enriched cultures and glia- for the cultures with very few glial cells. The challenge of keeping the neuronal network comparable while having glial cells removed in the glia- cultures was well accomplished, as evident from the same neuronal densities in both cultures and the similarity of the neuritic network, as assessed by phase

contrast and MAP2 immunostaining. The similarity of neuronal identity was further assesed by GAD67 immunostaining of GABA-ergic neurons and the quantification revealed similar ratios of GAD67 per MAP2 cells, thus supporting the idea that neuronal identity and growth was not affected by the two different culture protocols (Figure 14). The difference the fraction of neurons is resembling the difference in fraction of glial cells, as adding the percentages of MAP2 and GFAP positive cells per DAPI nuclei ends up to similar fractions of 85.3% and 88.9% in glia+ and glia- cultures, respectively. Together with the same absolute neuronal densities, these data suggest, that glial cells add up to the neurons in glia+ cultures. However, a small population of 11.1% and 14.7% unidentified cells remained in both culture systems, presumably due to inefficient neural differentiation and this population was not assessed in this study. However, a more detailed analysis of cell types by different markers would be interesting not only to define the unknown cells, but also to examine glial and neuronal identity in more depth.

4.1.2 Effects of glial cells on the electrophysiological functions of neurons

Maturity of neurons is usually characterized by analysing morphology and functional properties. Functional properties of neurons include generation of APs and firing patterns and synaptic integrity. To asses the general maturity of the cultures and to analyze the effects of glial cells on neuronal function, passive and spiking properties were analyzed in morphologically defined subpopulations of neurons, and voltage dependent Na^+ currents as well as synaptic integrity were measured in general. There was neither a difference in the proportion of the different morphological neuron types (multipolar, pyramidal and unidentified) nor an obvious impact on dendritic arborization as evident from the staining of neurons with Alexa Fluor 488 (Figures 15-17). As already seen in immunocytochemistry data, these results indicate that neuronal networks were comparable between glia+ and glia- culture concerning neuron morphology and identity.

The effects of glial cells on the electrophysiological properties of neurons were complex and less pronounced than expected, as the glial cells were lacking a general strong impact e.g. on the survival of the neurons. Effects could only be seen for specific parameters either in multipolar or in pyramidal cells. There was an increase in total input resistance of the multipolar cells from glia- cultures compared to glia+ cultures (Figure 18). A higher resistance means a lower conductance, which might arise from a slightly reduced cell size and dendritic

arborization or a difference in membrane properties, potentially a reduced channel density (Hille, 1992). However, because most AP parameters except for AHP size were not different between cultures (Figure 19), a general difference in channel density is likely. Although AHP was increased in glia- cultures and is known to be mediated by K^+ channels (Bean, 2007), this can not explain any difference seen in passive properties, which were measured at hyperpolarized potentials because the K^+ channels responsible for AHP are usually voltage dependent. Moreover, a larger AHP means higher expression of K^+ channels, which would lead to in increased membrane conductance, i.e. reduced resistance and a more negative membrane potential. This is in contrast to the finding, that multipolar cells have higher total input resistance and similar RMP in glia- cultures. In conclusion, the two observed significant effects consisting of higher total input resistance and larger AHP size do probably not share the same primary cause, but the latter might resemble a compensatory mechanism to keep excitability constant.

With reference to the differences in total input resistance and AHP size in the multipolar neurons, it was unexpected at first that effects on maximum AP frequency were occurring selectively in the pyramidal cell population only (Figures 20, 21). It was expected, that multipolar cells from glia- cultures would show a changed excitability, as an increased total input resistance leads to larger changes in membrane potential upon identical current injections. The fact, that multipolar neurons from glia- cultures consistently tended to have unaltered spike frequencies at all injected currents was not consistent with the finding of higher total input resistance and hints to compensatory mechanisms such as increased K^+ channel expression. This is supported by the data on excitability of pyramidal cells, which was different between glia- and glia+ cultures, although neither passive properties nor AP waveform parameters were different in these cells. The trend of glia- pyramidal cells to have higher AP frequencies at low current injections presumably resembles the trend of higher total input resistance in these cells. At higher current injections, however, the excitability effect takes over and glia- pyramidal neurons are not able to keep up with the AP frequencies of glia+ pyramidal cells. This became more evident, when AP frequencies were plotted versus membrane potential, where maximum AP frequencies differed significantly between glia+ and glia- cultures in the pyramidal cells and AP frequencies at low depolarizations were similar. To conclude, this means that pyramidal cells are capable of higher firing rates when glial cells are present, whereas the excitability of multipolar cells is not directly effected by glial cells.

In glia- cultures the multipolar cells might somehow compensate for a drop of spike rate. A possible mechanism could work by expression of Kv3 K^+ or similar channels that might lead to larger AHP size, which in turn increases spike rate to a level similar to neurons in glia+ cultures. This is thought to be caused by a faster recovery from inactivation of Na^+ channels as it has been shown for fast spiking interneurons (Lien & Jonas, 2008).

A general drop of AP frequencies was observed at high depolarizations. This is a result of reduced amplitudes of APs upon high depolarizations which are therefore not detected anymore. Probably due to inactivation and the lack of reactivation of voltage dependent Na^+ channels during constant depolarization, AP amplitude is reduced as more and more channels inactivate during a single current pulse, until it falls below the detection threshold and thus is not counted anymore. Also, the enhanced activation of voltage gated K^+ channels might dampen AP amplitudes at high depolarizations.

Another, statistical problem arises from the different abundance of the different subpopulations. Thus, the number of pyramidal neurons was always smaller than the number of multipolar neurons, giving rise to a relatively small statistical n different from that of the multipolar population. To counteract this, much more data would be needed to be collected. However, as statistical comparisons between subpopulations were not made, this problem might not have an impact on the reliability of the data of this study. Also, a more detailed analysis of Alexa Fluor 488 stained cells, for example by Sholl analysis, might be helpful to assess, whether glial cells promote dendritic arborization and maturation, as it was shown for human neuronal co-cultures with murine astrocytes (Tang et al., 2013). Already after a few days after plating, the latter study showed an increased dendrite branching of neurons, when co-cultured with glial cells, which almost doubled during the following 60 d of culture. Such large differences were not found in the present study, as this would be directly evident from Alexa Fluor 488 stainings. The reason probably is a relatively low glial cell number in the glia+ cultures. A straightforward interpretation of the electrophyioslogical results from subpopulations in detail remains somewhat difficult, because of the heterogeneity of the effects. It would also require further measurements of morphologies, ion currents and maybe of single ion channels with Sholl analysis, dynamic clamp experiments and excised patches or overexpression experiments, respectively.

Measurements of voltage dependent Na^+ currents was hindered by a poor space clamp due to the complex morphologies of the mature neurons, which drives the single electrode patch clamp technique to the edge of its possibilities. In strongly arborized neurons, the membrane potential is not clamped in the whole cell, making the experimental conditions unpredictable at some distance to the opening of the cell membrane, where the electrode controls the potential (Williams & Mitchell, 2008). This can also be seen from the current traces, where the Na^+ current suddenly reaches its maximum peak value from one voltage step to the next and no gradual rise in amplitude can be seen. Hence no attempt was made to quantify the non-clamped Na^+ currents. Nonetheless, the method could be used for qualitative measurements and the neurons clearly expressed voltage dependent Na^+ currents that were sensitive to TTX treatment. Also voltage dependent delayed rectifier K^+ currents were detectable. No obvious differences were found between neurons from glia+ and glia- cultures.

It was expected, as known from mouse data, that glial cells would have a strong impact on synaptic maturity and density (Pfrieger and Barres, 1997; Böhler et al., 2007). This effect was not found in this study, there was no difference between glia+ and glia- cultures in AMPA receptor mediated mEPSCs (Figure 24) or $GABA_A$ receptor mediated mPSCs (Figure 25). Reasons for this might be the long culture time that is necessary for the neurons to build synapses at all and the relatively small amount of glial cells in the glia+ cultures. This leaves room for compensatory mechanisms. Also, effects on synaptic integrity might occur later in culture time as analyzed in this study, AMPA receptor mediated mEPSC frequency was still lower than in primary mouse cultures (Figure 38F+G). The cultures still might not have reached optimal maturation after 8 weeks post immunopanning, even with glial cells and it would be very interesting from a developmental viewpoint to follow the effects of glial cells over extended time periods. Finally, the synaptic density and integrity was not assessed by electrophysiology in the study of Böhler et al. and Pfrieger and Barres did not look at mEPSCs, but generally at spontaneous activity which could also rise from a general increase in excitability.

In summary, electrophysiological data suggests an effect of glial cells on the excitability of the pyramidal neuron subpopulation, leading to higher maximum spike rates. Minor effects in the multipolar neuron subpopulation might reflect compensatory mechanisms, which prevent a decrease in AP frequencies in multiploar neurons in glia- cultures.

4.1.3 Effect of human glial cells on synchronous network calcium bursts

Neurons do not function on a single cell level and need to form networks to execute their tasks. Thus, after analysis of single neuron properties, the function of mature human iPSC derived neurons as a network was of interest in this study, as well as the influence of human glial cells on it. To achieve a reliable overview assay of the integration of neurons into the network, a Ca^{2+} imaging technique was established. This technique enabled the indirect observation of single neuron burst activities through optical assessment of the intracellular Ca^{2+} concentration on a qualitative basis (Figure 26). This single neuron data was used to empirically determine parameters for the detection of spontaneous synchronous network wide bursts with a participation of a relatively high number of the imaged neurons while filtering off single neuron activity and synchronous events with low neuronal participation (Figure 27).

As it got evident already during first experiments that not all networks expressed synchronous activity in the glia+ cultures, an epilepsy model was used, to examine the potential of the networks to generate synchronous bursts. In the model used, extracellular Mg^{2+} removal leeds to an overexcitation in mouse hippocampal neuron cultures through activation of NMDA receptors (Sombati and Delorenzo, 1995) and an effect called altered surface charge screening (Isaev et al., 2012). The surface charge effect is characterized by an increase of excitability due to removal of divalent cations that otherwise mask the negative charge on the membrane surface (Hille, 1992). Surface charge leads to a decrease in strength of the electrical field inside the membrane and thus renders voltage sensitive elements of membrane channels more sensible to changes in membrane potential. Voltage gated channels now open at smaller depolarization than in presence of high divalent cation concentrations. For Mg^{2+} removal treatment in the human iPSC derived networks, extracellular Mg^{2+} was reduced from 0.75 to 0 mM in this study. Because of the small changes in extracellular divalent ion concetration, surface charge screening effects were negligible and Mg^{2+} removal effects were probably mediated by NMDA receptor activation. Mg^{2+} removal rendered more networks active while not changing the frequency, amplitude or kinetics of synchronous network bursts (Figure 27). Thus, the Mg^{2+} free condition was used to characterize the properties of these synchronous network bursts and their frequency was used as a parameter to asses the activity of human networks.

To verify, that these Ca^{2+} signals were indirect measurements of electrical activity, their dependence on AP generation was assessed by successful blockade of all synchronous network bursts with TTX (Figure 28). Hence, they were indeed an indirect measurement of electrical network activity, as it was also shown by Opitz et al. (2002). These authors used Ca^{2+} imaging by Fluo-3 to assess neuronal network activity in rat cultures. In contrast to their data, the relatively low imaging framerate of 1 Hz used in this work made Ca^{2+} signals from single APs undetectable. Synaptic potentials could not be observed, too, because of low time resolution and the medium affinity of Fluo-4 for binding Ca^{2+} ions. Due to these constraints, signals in Ca^{2+} imaging were regarded as AP bursts occurring in single neurons. Synchrony of these events between neurons in the whole network was assessed, which is useful to get an overview over the connectivity of the network. To analyze the need for synaptic connectivity of neurons in the network to generate synchronous Ca^{2+} signals, their dependence on synaptic transmission was characterized. Using postsynaptic glutamate and $GABA_A$ receptor inhibitors, it was shown that synchronous network bursts were completely dependent on glutamatergic synaptic transmission (Figure 29), whereas blockade of $GABA_A$ receptors did not have a strong impact on them (Figure 30). The latter observation might result from a low GABA-ergic synapse density, as frequencies of $GABA_A$ receptor mediated mPSCs were quite low, too (Figure 25A, B). Along with the results on AP dependence, these show that the signals that are observed with Ca^{2+} imaging represent proper neuronal communications throughout the whole network.

Another important player in synaptic transmission is the extracellular Ca^{2+} concentration. Ca^{2+} influx is needed at the presynaptic terminal to initiate vesicle release upon arrival of APs (Llinás, 1991). Thus, the frequency of synchronous network bursts was expected to be proportional with extracellular Ca^{2+} concentration, as it was clearly dependent on excitatory transmission. Lowering the extracellular Ca^{2+} concentration showed the expected effect of reduced synchronous network bursts, probably resulting from inhibited vesicle release (Figure 31). At the used extracellular Ca^{2+} concentrations in the mM range it is unlikely that the imaging method, which itself is depending on Ca^{2+} influx, is affected, because these concentrations would still be several orders of magnitude higher than the intracellular Ca^{2+} concentration in the range of 100 nM (Kandel et al., 2000), which is also in the range of the dissociation constant ($K_d(Ca^{2+}) = 345$ nM) for Fluo-4 (Molecular Probes, 2011). Thus, Ca^{2+} influx could still be detected with this method and even if Ca^{2+} influx is reduced to a small

extent, the number of detected bursts would not be lower, as long as Fluo-4 can bind sufficient Ca^{2+}. The ΔF/F method used for burst detection additionally ensures, that intensity differences are minimized and thresholding is minimally affected by basic intensity differences. It might be hypothesized that increasing extracellular Ca^{2+} will lead to more vesicle release, thus enhancing synchronous network bursting. This could not be observed, as the frequency of synchronous network bursts dropped to zero upon increases of extracellular Ca^{2+} concentration to 5 or 10 mM. The reason for this is likely to be a surface charge effect which describes masking of the negative charges on the outside of the cell membrane by divalent ions, mainly Ca^{2+} (Hille, 1992). This results in a stronger electrical field across the membrane, which makes it harder to open voltage dependent channels by depolarization, thus reducing excitability. In summary, both Ca^{2+} and Mg^{2+} ions play a crucial role in the generation of synchronous network bursts (Isaev at al., 2012) and there is an inhibition by surface charge screening at high Ca^{2+} concentrations and an inhibition of synaptic transmission at low Ca^{2+} concentrations, thus creating a narrow window of optimal extracellular Ca^{2+} concentration in the Mg^{2+} free condition.

After characterization of the synchronous network bursts, comparative Mg^{2+} removal experiments were conducted to examine a potential difference in the ability of glia+ and glia- cultures to generate synchronous network bursts (Figure 32). Surprisingly, both cultures were able to express network bursts to the same extent in Mg^{2+} free condition. However, in the presence of Mg^{2+}, there was almost no activity in glia- cultures as measured by the synchronous network burst frequency. The fact that the synchronous network bursts frequency was not increased in the glia+, but in the glia- cultures shows, that the Mg^{2+} removal is not simply a surface charge effect. As ion concentrations are the same in both cultures, glia+ cultures should also have lower frequencies in Mg^{2+} containing conditions, if the effect was solely driven by surface charge effects. On the other hand, glia- cultures showed very little activity when Mg^{2+} was present, but were susceptible to Mg^{2+} removal which increased synchronous network burst frequency. Apart from surface charge effects, all NMDA receptors should be activated as the Mg^{2+} free condition removes the Mg^{2+} block from NMDA receptors (Mayer et al., 1984). Because frequencies are the same in glia+ and glia- cultures under Mg^{2+} free conditions, a difference in NMDA receptor expression or composition between glia+ and glia- cultures was not likely. This points to a general lack of excitatory drive in the glia- cultures and is in line with the finding that there is a difference in excitability of the pyramidal

cells between glia+ and glia- cultures. The latter finding might be the reason for the very low synchronous network burst frequencies seen in glia- networks. It appears conceivable, that the observed effect on the whole network is caused by the relatively small subpopulation of pyramidal neurons. In line with the findings from this work, a computer model showed a crucial impact of a specific subpopulation of neurons with relatively high firing frequencies on synchronous network activity by removing it from the model and assessment of population burst frequency (Tsodyks at al., 2000). Removing the population of neurons that fired spontaneously at medium frequencies of 2-3 Hz resulted in a complete extinction of population bursts, whereas high and low frequency spiking neurons did not have any impact on the population burst frequency. In the present study, spontaneous firing was not assessed and the pyramidal subpopulation had the highest maximum AP frequencies, making a direct comparison difficult. Spontaneous frequencies would be expected to be lower than maximum AP frequencies and might end up in the range of a few Hz like in the study of Tsodyks et al.. Moreover, the difference in maximum AP frequency in the pyramidal subpopulation was the only prominent difference found in electrophysiological experiments that could explain the difference in synchronous network burst frequencies. As the influence of NMDA receptors was evident from Ca^{2+} imaging and Mg^{2+} free experiments, the question arises, if glycine might play a role as it is an important co-factor for NMDA receptor activation (Kleckner and Dingledine, 1988). Kleckner and Dingledine reported a half maximal response of NMDA receptors to NMDA at a concentration of 670 nM glycine. The NBNS21S culture medium contained 400 µM glycine, which is well above the half maximal response. However, during electrophysiological measurements and Ca^{2+} imaging, no glycine was added to the buffers. This might explain differences in Ca^{2+} imaging concerning the excitability of NMDA receptors between glia+ and glia- cultures, as astrocytes might provide glycine through glycine co-transporters which possibly mediate glycine efflux upon astrocyte depolarization during experiments (Verkhratsky and Butt, 2007). Thus, addition of glycine might enhance the ability of networks from glia- cultures to generate synchronous network bursts. The data on Mg^{2+} removal experiments indicates that the synchronous network activity is a very complex property of a recisely balanced system.

In summary, it is suggested, that the excitability of excitatory pyramidal neurons drives the synchronous network activity in glia+ cultures and that glial cells have a positive influence on that excitability, leaving glia- cultures inactive under physiological conditions. It would be

interesting to more precisely define the dependence of the synchronous network activity on NMDA receptor functionsor and surface charge effects in glia- cultures with Mg^{2+} dependence experiments, glycine addition and NMDA receptor inhibitors.

4.1.4 Outlook

During the time of conducting the present work, lots of improvements have been made on protocols to differentiate human iPSCs to neurons, making them faster, more specific and more pure. The natural differentiation through a neuronal precursor state (neuronal progenitor cells, NPC) that is widely used is being challenged by direct reprogramming and faster differentiation techniques. Possible methods include direct conversion (Vierbuchen et al., 2010), application of small molecules at more early stages (Choi and Nam, 2012) and transcriptional activation (Busskamp et al., 2014). In the present study, speeding up the process of differentiation would increase efficiency of protocols, although maturation will still take a long time, even under glia+ conditions. Modifying the protocol to increase purity might in turn decrease the amount of glial cells in the glia+ cultures, as they only arise from a not completely specific neuronal selection. Creating two different differentiation protocols, one for neurons and another one for glial cells and then bringing the cells into co-culture after differentiation would be the next reasonable step which also would make it possible to increase the amount of glial cells in glia+ cultures, which is a major drawback of this culture system. The hypothesis is that more glial cells would lead to stronger effects on maturation and that the function of the networks would become more reproducible to achieve 100% active networks. These networks could then be used to further study effects of human glial cells on neuronal networks and *vice versa,* or for disease modeling. Especially for the latter case, sophisticated human neural cultures are necessary, as *in vivo* experiments are not possible and differences between murine and human biology are obvious. So it remains a long term goal to achieve networks that are more close to human physiological conditions than mouse primary cultures. However, the latter are still important to break down experimental conditions to the most simple small parts or to get a preliminary idea of *in vivo* situations and mechanisms. Thus, the aim of the development of human neural networks differs from the use of mouse culturs in respect to their complexity. In the end, murine and other animal models might become less abundant in neuroscience but are still very precious, especially for basic research and to build a basis for experiments on human cells.

4.2 Synaptotoxic effects of amyloid-β

Alzheimer's diseases is a neurodegenerative disease which is characterized by an abnormal increase in brain levels of the Aβ peptide that leads to the formation of amyloid plaques. Elevated concentrations of soluble Aβ oligomers are thought to be synapto- and neurotoxic, as shown in studies on murine models (Lambert et al., 1998; Walsh et al., 2002) and human models (Vazin et al., 2014; Nieweg et al., 2015). The present study confirmed in parts the findings of Nieweg et al. (2015) in the above characterized human iPSC derived neuronal network by demonstrating synaptotoxic effects of a synthetic Aβ preparation. In addition, the activity dependence of synaptotoxic Aβ effects was analyzed by preapplication of TTX and addition of naturally secreted Aβ containing 7PA2 conditioned medium in mouse hippocampal neurons.

4.2.1 Synthetic amyloid-β preparation

By using synthetic Aβ peptides, it is possible to create a more defined and reproducible Aβ preparation as it is not depending on the secretion by cells. The latter issue might be a considerable source of variation concerning concentration and aggregation in the 7PA2 supernatant preparation. However, definition and characterization of physiological Aβ peptides from synthetic Aβ for experiments and disease modeling is still problematic, as Aβ has many aggregation states and therefore preparations differ a lot between labs and studies. For example, it is not yet clear, whether there is a single toxic species or whether Aβ has a more general effect when present in different conformations (Belinova et al., 2012). Belinova et al.state that analysis of the used Aβ preparation is necessary in every study. In some studies characterization is done extensively by biophysical methods but biological assays lack in-depth analysis of mechanisms (Broersen et al., 2011). In other studies, very sensitive assays to find mechanisms are applied while Aβ preparations are characterized only roughly without biophysical methods (Shankar et al., 2007). Especially the use of SDS-PAGE is popular to show the presence of the so called SDS stable oligomers, which are thought to be the main effector of synaptotoxic effects. However, the use of SDS breaks down higher oligomers and under certain circumstances can even induce artificial oligomerization (Bitan et al., 2005). Usually, synthetic Aβ preparations consist of several different aggregation states of Aβ and these might be differentially affected by SDS treatment. Thus, SDS changes the composition of the sample dramatically, giving a very distorted image of the used Aβ preparation. To

overcome this problem, a native PAGE and subsequent Western blot technique was established in the present study to see the natural state of the used Aβ preparation.

The method to dissolve synthetic Aβ stably in HFIP and evaporate it to a thin Aβ film under constant nitrogen flow for storage is widely used (Fa et al., 2010; Broersen et al., 2011). However, for the treatment of cells, reconstitution has to be done in DMSO which is toxic to cells and has effects on tau phosphorylation at lower concentrations (Julien et al., 2012). As tau posphorylation is another cellular mechanism that is impaired in AD, one should be extremely cautious about the use of DMSO, especially in AD disease modeling. Thus removal of DMSO from the preparation by buffer exchange using desalting columns is usually done after reconstitution of Aβ (Broersen et al., 2011). However, these steps introduce even more sources of variation and loss of Aβ to material surfaces. Moreover, this protocol is merely suitable to generate monomers, as seen in the present study by the use as a monomeric control. No oligomeric bands were observed in any fresh HFIP/DMSO sample, making the preparation clean, but rather unphysiological (Figure 33). To create physiological Aβ species out of this HFIP/DMSO preparation, an aggregation protocol has to be applied, which again introduces sources of variability. In contrast, dissolving the peptide directly in culture medium instead is easy and ensures minimal interference of the vehicle with the cells and immediately creates a range of oligomers as was shown native PAGE and subsequent Western blot in the present study. The most abundant species in this preparation were monomers and very large, probably fibrillary structures that did not enter the gel. Bands in between indicated that different aggregation states were present, from dimers to higher oligomers, which are thought to be the major toxic species of Aβ (Benilova et al., 2012). However, this procedure leads to a strong loss of peptide, probably due to incomplete dissolution and aggregation processes, reducing the concentration of Aβ monomer to about 1% of the nominal value as indicated by comparison to the monomeric HFIP/DMSO control preparation. Thus, the final nominal treatment concentration has to be corrected from 1 µM to about 10 nM Aβ monomer, which is equivalent to about 40-50 ng/ml. Seubert et al. (1992) reported a physiological value of 2.5 ng/ml Aβ as assessed by ELISA (enzyme-linked immunosorbent assay) in human cerebrospinal fluid. As the concentrations of different oligomers would be even lower than the estimated monomer concentration, the effective Aβ concentration used in the present study night be close to pathophysiological concentrations, but elevated and thus can be used to assess Aβ effects on neurons under physiological conditions. A final issue is the long term

storage of such an Aβ preparation, which might be rather difficult. However this was not done and assessed in the present study and might be overcome by using exclusively fresh preparations.

4.2.1.1 Absence of effects of amyloid-β on voltage dependent sodium ion currents

In mouse hippocampal slices, Ren et al. (2014) reported an increase and Brown et al. (2011) reported and decrease of peak Na^+ current density after treatment with synthetic Aβ, which might be caused by a direct interaction between the channels and Aβ that is membrane bound in some form (summarized in Strodel et al., 2010). In addition to the proposed direct interaction with membrane and channels or to the formation of pores by Aβ, the free charges of massively membrane incorporated Aβ might lead to surface charge effects that might lead to a change in excitability. To check, whether the Aβ preparation used induces similar effects in human iPSC derived neurons, whole cell patch-clamp experiments in freshly dissociated neurons were conducted to exclude measurement errors arising from poorly clamped cells (Williams and Mitchell, 2008). However, there was no direct effect on excitability, as voltage dependent Na^+ currents were not different between vehicle and Aβ treatment (Figure 34). Neither a difference in peak current density nor a shift in I/V curves was found. Several reasons might account for this different result as compared to the studies of Ren et al. and Brown et al.. In both studies, Aβ and cell preparations were different from those used in the present work. Ren et al. used a HFIP/DMSO preparation in rat hippocampal slices, wheres Brown et al. used hippocampal slices of a transgenic AD mouse model. Although the Aβ preparation used in this work contained many different species, it is possible that the specific aggregation state that would incorporate into the membrane was missing. Furthermore, as the kinetics of Aβ membrane incorporation are not known, it might be necessary to keep Aβ present during measurements in case that the affinity for the cell membrane is low and Aβ is washed out of the membrane during experiment. Different Aβ exposure times might also explain the contradictory results of the studies by Ren et al. (short term application) and Brown et al. (transgenic model). This was not accounted for in the present study. Another difficulty was the high variability of the voltage dependent Na^+ currents. Some of the cells were only expressing very small Na^+ currents, thereby increasing the variability of current densities. Thus, the human preparation has to be optimized further to use it for further studies on effects of membrane bound Aβ.

4.2.1.2 Synthetic amyloid-β is synaptotoxic in human iPSC derived neurons

Amyloid-β is known to be synaptotoxic and these effects were verified in human iPSC derived neurons that were generated in this study. To assess Aβ effects on synaptic AMPA receptors, mEPSCs were measured in whole cell patch-clamp experiments in human neurons at 8 weeks post immunopanning. After 3 d of treatment with Aβ, an effect on mEPSC frequency or amplitude was not detectable (Figure 35). However, when treated for 7 d, human neurons showed reduced AMPA receptor mediated mEPSC amplitudes and a trend to lower frequencies, indicating that the Aβ preparation used is synaptotoxic (Figure 36). These results are in line with the results of Nieweg et al. (2015) who used the same human iPSC derived neuron preparation and described synaptotoxic effects of naturally secreted Aβ (7PA2 supernatant) after 8 d treatment. In that study, a significant reduction of AMPA receptor mediated mEPSC amplitudes was significantly induced by treatment of human iPSC derived neurons with 7PA2 supernatant and a trend to reduced mEPSC frequencies was also shown. The trend to a reduced mEPSC frequency might the result of smaller amplitude mEPSCs beeing occluded by the recording noise. The present data also verify, that the Aβ preparation used in Na^+ current experiments was generally active, solidifying the negative results. Furthermore, the absence of cell death in cell viability essays ensured the absence of general cytotoxicity and thus the specificity of Aβ effects on synapses (Figure 37).

4.2.2 Activity dependence of synaptotoxicity of naturally secreted amyloid-β

Synaptic plasticity is a dynamic process that changes synapse function and structure in an activity dependent manner. Although neurons only function in networks, it is the synapses and their dynamics which enable neuronal networks to do the powerful computations that happen in the brain. These dynamic changes can lead to drastic changes in structure and composition of synapses and their receptors, for example in NMDA receptor subunit composition (Ehlers, 2006). It is well known, that Aβ can interfere with synaptic plasticity such as LTP (Walsh et al., 2002) or LTD (Li et al., 2006). However it is still not clear, what the pathological mechanisms of Aβ mediated synaptotoxicity are. Although there is evidence that the NMDA receptors play a crucial role (Rönicke et al., 2011; Kessels et al., 2013; Varga et al., 2014), several different other mechanisms have been proposed, like direct interactions with Ca^{2+} channels (Herman et al., 2013), K^+ channels (Nava-Mesa et al., 2013) and cell membrane (Lukiw, 2013). One reason for the heterogeneity of effects might be the fact, that the plasticity

states of neurons and their synapses are not well defined or characterized in studies of Aβ synaptotoxicity, although it is known that there are defined changes in molecular and structural composition upon plasticity (Ehlers, 2006). Therefore, this work aimed to push synaptic plasticity states into an AMPA receptor up-scaled state, which is occurring after blockade of all activity with TTX (Turrigiano et al., 1998) and then to assess synaptotoxicity of Aβ in this defined synaptic state. Aβ treatment in the form of 7PA2 supernatant was done in TTX pretreated mature mouse hippocampal neurons and AMPA receptor mediated mEPSCs were measured in whole cell patch-clamp experiments (Figure 38). In control condition without TTX, no effect of Aβ was found, in contrast to earlier findings of reduced mEPSC amplitudes after 3 d of 7PA2 supernatant treatment in immature mouse cortical neurons (Andreyeva et al., 2012). This might be due to the use of more mature hippocampal neurons in co-culture with glia cells, which might protect neurons from Aβ effects. Scaled up synapses only showed a trend to be more vulnerable to Aβ treatment in mature mouse hippocampal neurons. However, when the preparations used were examined for their mean increase in mEPSC amplitude under TTX treatment, one preparation did not show an up-scaling effect. Selecing preparations by their response to TTX revealed, that preparations that showed an up-scaling process were more vulnerable to Aβ under TTX condition. To verify these preliminary data, neuronal preparation protocols neet to be improved to get more stable up scaling responses to TTX. Also, an activity inducing condition could be tested to see if the effect is reversed under down scaling conditions, for example using gabazine or Mg^{2+} free treatment.

4.2.3 Outlook

Several studies reported the successful differentiation of AD patient derived iPSCs to neurons which exhibited an increased production of Aβ (Qiang et al., 2011; Yagi et al., 2011; Israel et al., 2012). The advantage of such systems is the close resemblance of *in vivo* situations. However, synaptotoxicity was not described in these studies and it is not yet clear, what role epigenetics might play in the disease and often differentiation protocols include treatments that might delete those epigenetic imprints. In the end, patient specific preparations might be useful for drug screening and individualized therapy (Inoue et al., 2014). Also new insights will be gained into mechanisms which might then be verified in simpler culture systems and *vice versa*. It is thus still necessary to develop a simple, yet reliable human neuronal AD disease model, in which Aβ effects can be studied by external application. To achieve this,

both, human neurons and Aβ preparations have to get more defined and sophisticated. For example, the next step towards a more physiological AD model would be the generation of plaques in the dish along with human neurons, as described by Choi et al. (2014). These authors generated a three-dimensional human neuronal culture system with FAD mutations carrying cells that naturally secret amyloid-β and develop plaque like deposits of amyloid protein along with the hyperphosphorylated tau phenotype. However, neuronal function was not assessed in this study. FAD patient derived neurons might develop a synpaptic phenotype after prolonged cultivation, which would be a big step forward to a realistic cell culture model of the AD.

5 References

Acuna, C., Guo, Q., Burré, J., Sharma, M., Sun, J. & Südhof, T. C. (2014). Microsecond dissection of neurotransmitter release: SNARE-complex assembly dictates speed and Ca^{2+} sensitivity. *Neuron*, *82*(5), 1088–100. doi:10.1016/j.neuron.2014.04.020

Allen, N. J. (2013). Role of glia in developmental synapse formation. *Current Opinion in Neurobiology*, *23*(6), 1027–1033.

Allen, N. J., Bennett, M. L., Foo, L. C., Wang, G. X., Chakraborty, C., Smith, S. J. & Barres, B. A. (2012). Astrocyte glypicans 4 and 6 promote formation of excitatory synapses via GluA1 AMPA receptors. *Nature*, *486*(7403), 410–414.

Alzheimer, A. (1907). Uber eine eigenartige Erkrankung der Hirnrinde. *Allgemeine Zeitschrift für Psychiatrie*, *64*, 146–148.

Andreyeva, A., Nieweg, K., Horstmann, K., Klapper, S., Müller-Schiffmann, A., Korth, C. & Gottmann, K. (2012). C-terminal fragment of N-cadherin accelerates synapse destabilization by amyloid-β. *Brain*, *135*(7), 2140–2154.

Barrett, S. D., Biwersi, C., Kaufman, M., Tecle, H. & Warmus, J. S. (2002). Oxygenated esters of 4-iodo phenylamino benzhydroxamic acids. Retrieved from http://www.google.tl/patents/WO2002006213A2?cl=pt-PT

Bean, B. P. (2007). The action potential in mammalian central neurons. *Nature Reviews Neuroscience*, *8*(6), 451–465.

Ben-Ari, Y. (2001). Developing networks play a similar melody. *Trends in Neurosciences*, *24*(6), 353–360.

Benilova, I. & De Strooper, B. (2013). Promiscuous Alzheimer's Amyloid: Yet Another Partner. *Science*, *341*(6152), 1354–1355.

Benilova, I., Karran, E. & De Strooper, B. (2012). The toxic Aβ oligomer and Alzheimer's disease: an emperor in need of clothes. *Nature Neuroscience*, *15*(3), 349–357.

Bero, A. W., Yan, P., Roh, J. H., Cirrito, J. R., Stewart, F. R., Raichle, M. E., … Holtzman, D. M. (2011). Neuronal activity regulates the regional vulnerability to amyloid-β deposition. *Nature Neuroscience*, *14*(6), 750–756.

Bitan, G., Fradinger, E. A., Spring, S. M. & Teplow, D. B. (2005). Neurotoxic protein oligomers-what you see is not always what you get. *Amyloid*, *12*(2), 88–95.

Boehler, M. D., Wheeler, B. C. & Brewer, G. J. (2007). Added astroglia promote greater synapse density and higher activity in neuronal networks. *Neuron Glia Biology*, *3*(02), 127–140.

Broersen, K., Jonckheere, W., Rozenski, J., Vandersteen, A., Pauwels, K., Pastore, A., … Schymkowitz, J. (2011). A standardized and biocompatible preparation of aggregate-free amyloid beta peptide for biophysical and biological studies of Alzheimer's disease. *Protein Engineering Design and Selection*, *24*(9), 743–750.

Brown, J. T., Chin, J., Leiser, S. C., Pangalos, M. N. & Randall, A. D. (2011). Altered intrinsic neuronal excitability and reduced Na^+ currents in a mouse model of Alzheimer's disease. *Neurobiology of Aging*, *32*(11), 2109–e1.

Busskamp, V., Lewis, N. E., Guye, P., Ng, A. H., Shipman, S. L., Byrne, S. M., … others. (2014). Rapid neurogenesis through transcriptional activation in human stem cells. *Molecular Systems Biology*, *10*(11).

Caceres, A., Banker, G., Steward, O., Binder, L. & Payne, M. (1984). MAP2 is localized to the dendrites of hippocampal neurons which develop in culture. *Developmental Brain Research*, *13*(2), 314–318.

Cárdenas-Aguayo, M. del C., Silva-Lucero, M. del C., Cortes-Ortiz, M., Jiménez-Ramos, B., Gómez-Virgilio, L., Ramirez-Rodriguez, G., … others. (2014). Physiological Role of Amyloid Beta in Neural Cells: The Cellular Trophic Activity.

Chen, Y., Stevens, B., Chang, J., Milbrandt, J., Barres, B. A. & Hell, J. W. (2008). NS21: re-defined and modified supplement B27 for neuronal cultures. *Journal of Neuroscience Methods*, *171*(2), 239–247.

Chiappalone, M., Bove, M., Vato, A., Tedesco, M. & Martinoia, S. (2006). Dissociated cortical networks show spontaneously correlated activity patterns during in vitro development. *Brain Research*, *1093*(1), 41–53.

Choi, S. H., Kim, Y. H., Hebisch, M., Sliwinski, C., Lee, S., D'Avanzo, C., … others. (2014). A three-dimensional human neural cell culture model of Alzheimer's disease. *Nature*, *515*(7526), 274–278.

Choi, Y. & Nam, T. (2012). Chemical biology in stem cell research. *Archives of Pharmacal Research*, *35*(2), 281–297.

Christopherson, K. S., Ullian, E. M., Stokes, C. C., Mullowney, C. E., Hell, J. W., Agah, A., … Barres, B. A. (2005). Thrombospondins are astrocyte-secreted proteins that promote CNS synaptogenesis. *Cell*, *120*(3), 421–433.

Cirrito, J. R., Deane, R., Fagan, A. M., Spinner, M. L., Parsadanian, M., Finn, M. B., … others. (2005). P-glycoprotein deficiency at the blood-brain barrier increases amyloid-β deposition in an Alzheimer disease mouse model. *Journal of Clinical Investigation*, *115*(11), 3285.

Daley, G. Q. & Scadden, D. T. (2008). Prospects for stem cell-based therapy. *Cell*, *132*(4), 544–548.

Deane, R., Du Yan, S., Submamaryan, R. K., LaRue, B., Jovanovic, S., Hogg, E., … others. (2003). RAGE mediates amyloid-β peptide transport across the blood-brain barrier and accumulation in brain. *Nature Medicine*, *9*(7), 907–913.

DeKosky, S. T. & Scheff, S. W. (1990). Synapse loss in frontal cortex biopsies in Alzheimer's disease: correlation with cognitive severity. *Annals of Neurology*, *27*(5), 457–464.

Duyckaerts, C., Delatour, B. & Potier, M.-C. (2009). Classification and basic pathology of Alzheimer disease. *Acta Neuropathologica*, *118*(1), 5–36.

Ehlers, M. D. (2003). Activity level controls postsynaptic composition and signaling via the ubiquitin-proteasome system. *Nature Neuroscience*, *6*(3), 231–242.

Eng, L. F. (1985). Glial fibrillary acidic protein (GFAP): the major protein of glial intermediate filaments in differentiated astrocytes. *Journal of Neuroimmunology*, *8*, 203–214.

Fa, M., Orozco, I. J., Francis, Y. I., Saeed, F., Gong, Y. & Arancio, O. (2010). Preparation of Oligomeric β-amyloid$_{1\text{-}42}$ and Induction of Synaptic Plasticity Impairment on Hippocampal Slices. *Journal of Visualized Experiments: JoVE*, (41).

Funke, S. A. & Willbold, D. (2012). Peptides for therapy and diagnosis of Alzheimer's disease. *Current Pharmaceutical Design*, *18*(6), 755.

Garcia-Osta, A. & Alberini, C. M. (2009). Amyloid beta mediates memory formation. *Learning & Memory (Cold Spring Harbor, N.Y.)*, *16*(4), 267–72. doi:10.1101/lm.1310209

Gonzales, C., Kaufman, D., Tobin, A. & Chesselet, M.-F. (1991). Distribution of glutamic acid decarboxylase (Mr 67 000) in the basal ganglia of the rat: an immunohistochemical study with a selective cDNA-generated polyclonal antibody. *Journal of Neurocytology*, *20*(12), 953–961.

Grüning, C. S. R., Klinker, S., Wolff, M., Schneider, M., Toksöz, K., Klein, A. N., … Hoyer, W. (2013). The off-rate of monomers dissociating from amyloid-β protofibrils. *The Journal of Biological Chemistry*, *288*(52), 37104–11. doi:10.1074/jbc.M113.513432

Haass, C. & Selkoe, D. J. (2007). Soluble protein oligomers in neurodegeneration: lessons from the Alzheimer's amyloid β-peptide. *Nature Reviews Molecular Cell Biology*, *8*(2), 101–112.

Hermann, D., Mezler, M., Müller, M. K., Wicke, K., Gross, G., Draguhn, A., … Nimmrich, V. (2013). Synthetic Aβ oligomers ($A\beta_{1-42}$ globulomer) modulate presynaptic calcium currents: Prevention of Aβ-induced synaptic deficits by calcium channel blockers. *European Journal of Pharmacology*, (0), – . doi:10.1016/j.ejphar.2013.01.030

Hille, B. & others. (1992). *Ion channels of excitable membranes* (Vol. 507, p. 8; 457–461). Sinauer Sunderland, MA.

Inoue, H., Nagata, N., Kurokawa, H. & Yamanaka, S. (2014). iPS cells: a game changer for future medicine. *The EMBO Journal*, *33*(5), 409–417.

Isaev, D., Ivanchick, G., Khmyz, V., Isaeva, E., Savrasova, A., Krishtal, O., … others. (2012). Surface charge impact in low-magnesium model of seizure in rat hippocampus. *Journal of Neurophysiology*, *107*(1), 417–423.

Israel, M. A., Yuan, S. H., Bardy, C., Reyna, S. M., Mu, Y., Herrera, C., … others. (2012). Probing sporadic and familial Alzheimer's disease using induced pluripotent stem cells. *Nature*, *482*(7384), 216–220.

Jia, H., Rochefort, N. L., Chen, X. & Konnerth, A. (2011). In vivo two-photon imaging of sensory-evoked dendritic calcium signals in cortical neurons. *Nature Protocols*, *6*(1), 28–35.

Jones, E. V., Bernardinelli, Y., Tse, Y. C., Chierzi, S., Wong, T. P. & Murai, K. K. (2011). Astrocytes control glutamate receptor levels at developing synapses through SPARC-β-integrin interactions. *The Journal of Neuroscience*, *31*(11), 4154–4165.

Julien, C., Marcouiller, F., Bretteville, A., El Khoury, N. B., Baillargeon, J., Hébert, S. S. & Planel, E. (2012). Dimethyl sulfoxide induces both direct and indirect tau hyperphosphorylation. *PloS One*, *7*(6), e40020.

Kandel, E. R., Schwartz, J. H., Jessell, T. M. & others. (2000). *Principles of neural science* (4th ed., p. 19; 20; 159). McGraw-Hill New York.

Kessels, H. W., Nabavi, S. & Malinow, R. (2013). Metabotropic NMDA receptor function is required for β-amyloid-induced synaptic depression. *Proceedings of the National Academy of Sciences*.

Kim, D. H., Yeo, S. H., Park, J.-M., Choi, J. Y., Lee, T.-H., Park, S. Y., … Cha, H.-J. (2014). Genetic markers for diagnosis and pathogenesis of Alzheimer's disease. *Gene*, *545*(2), 185–193.

Kleckner, N. W., Dingledine, R. & others. (1988). Requirement for glycine in activation of NMDA-receptors expressed in Xenopus oocytes. *Science (New York, NY)*, *241*(4867), 835.

Kramer, M. A. & Cash, S. S. (2012). Epilepsy as a disorder of cortical network organization. *The Neuroscientist*, *18*(4), 360–372.

Kucukdereli, H., Allen, N. J., Lee, A. T., Feng, A., Ozlu, M. I., Conatser, L. M., … others. (2011). Control of excitatory CNS synaptogenesis by astrocyte-secreted proteins Hevin and SPARC. *Proceedings of the National Academy of Sciences*, *108*(32), E440–E449.

Kuperstein, I., Broersen, K., Benilova, I., Rozenski, J., Jonckheere, W., Debulpaep, M., … others. (2010). Neurotoxicity of Alzheimer's disease Aβ peptides is induced by small changes in the $A\beta_{42}$ to $A\beta_{40}$ ratio. *The EMBO Journal*, *29*(19), 3408–3420.

Ladiwala, A. R. A., Litt, J., Kane, R. S., Aucoin, D. S., Smith, S. O., Ranjan, S., … Tessier, P. M. (2012). Conformational differences between two amyloid-β oligomers of similar size and dissimilar toxicity. *Journal of Biological Chemistry*, *287*(29), 24765–24773.

Lambert, M. P., Barlow, A., Chromy, B. A., Edwards, C., Freed, R., Liosatos, M., … others. (1998). Diffusible, nonfibrillar ligands derived from $A\beta_{1\text{-}42}$ are potent central nervous system neurotoxins. *Proceedings of the National Academy of Sciences*, *95*(11), 6448–6453.

Laßek, M., Weingarten, J. & Volknandt, W. (2015). The synaptic proteome. *Cell and Tissue Research*, *359*(1), 255–265.

Li, S., Hong, S., Shepardson, N. E., Walsh, D. M., Shankar, G. M. & Selkoe, D. (2009). Soluble oligomers of amyloid-β protein facilitate hippocampal long-term depression by disrupting neuronal glutamate uptake. *Neuron*, *62*(6), 788–801.

Li, S., Jin, M., Koeglsperger, T., Shepardson, N. E., Shankar, G. M. & Selkoe, D. J. (2011). Soluble Aβ oligomers inhibit long-term potentiation through a mechanism involving excessive activation of extrasynaptic NR2B-containing NMDA receptors. *The Journal of Neuroscience*, *31*(18), 6627–6638.

Lien, C.-C. & Jonas, P. (2003). Kv3 potassium conductance is necessary and kinetically optimized for high-frequency action potential generation in hippocampal interneurons. *The Journal of Neuroscience*, *23*(6), 2058–2068.

Llinás, R. R. (1991). Depolarization release coupling: an overview. *Annals of the New York Academy of Sciences*, *635*(1), 3–17.

Malinow, R. & Malenka, R. C. (2002). AMPA receptor trafficking and synaptic plasticity. *Annual Review of Neuroscience*, *25*(1), 103–126.

Molecular Probes (2011). Fluo Calcium Indicators manual.

Morizane, A., Kikuchi, T., Nishimura, K., Takahashi, J. & others. (2011). Small-molecule inhibitors of bone morphogenic protein and activin/nodal signals promote highly efficient neural induction from human pluripotent stem cells. *Journal of Neuroscience Research*, *89*(2), 117–126.

Mucke, L. & Selkoe, D. J. (2012). Neurotoxicity of Amyloid β-Protein: Synaptic and Network Dysfunction. *Cold Spring Harbor Perspectives in Medicine*, *2*(7).

Nava-Mesa, M. O., Jiménez-Diaz, L., Yajeya, J. & Navarro-Lopez, J. D. (2013). Amyloid-β induces synaptic dysfunction through G protein-gated inwardly rectifying potassium channels in the fimbria-CA3 hippocampal synapse. *Frontiers in Cellular Neuroscience*, *7*.

Nieweg, K., Andreyeva, A., van Stegen, B., Tanriöver, G. & Gottmann, K. (2015). Alzheimer's disease-related amyloid-β induces synaptotoxicity in human iPS cell-derived neurons. *Cell Death \& Disease*, *6*(4), e1709.

Nityanandam, A. & Baldwin, K. K. (2015). Advances in reprogramming based study of neurologic disorders. *Stem Cells and Development.* doi:10.1089/scd.2015.0044.

Odawara, A., Saitoh, Y., Alhebshi, A. H., Gotoh, M. & Suzuki, I. (2014). Long-term electrophysiological activity and pharmacological response of a human induced pluripotent stem cell-derived neuron and astrocyte co-culture. *Biochemical and Biophysical Research Communications*, *443*(4), 1176–81. doi:10.1016/j.bbrc.2013.12.142

Opitz, T., De Lima, A. D. & Voigt, T. (2002). Spontaneous development of synchronous oscillatory activity during maturation of cortical networks in vitro. *Journal of Neurophysiology*, *88*(5), 2196–2206.

Paul, B. Y., Hong, C. C., Sachidanandan, C., Babitt, J. L., Deng, D. Y., Hoyng, S. A., … Peterson, R. T. (2008). Dorsomorphin inhibits BMP signals required for embryogenesis and iron metabolism. *Nature Chemical Biology*, *4*(1), 33–41.

Payne, N. L., Sylvain, A., O'Brien, C., Herszfeld, D., Sun, G. & Bernard, C. C. (2015). Application of human induced pluripotent stem cells for modeling and treating neurodegenerative diseases. *New Biotechnology*, *32*(1), 212–228.

Pfrieger, F. W. & Barres, B. A. (1997). Synaptic efficacy enhanced by glial cells in vitro. *Science*, *277*(5332), 1684–1687.

Podlisny, M. B., Ostaszewski, B. L., Squazzo, S. L., Koo, E. H., Rydell, R. E., Teplow, D. B. & Selkoe, D. J. (1995). Aggregation of secreted amyloid-protein into sodium dodecyl sulfate-stable oligomers in cell culture. *Journal of Biological Chemistry*, *270*(16), 9564–9570.

Prince, M., Albanese, E. & Guerchet, M. (2014). World Alzheimer Report 2014.

Qiang, L., Fujita, R., Yamashita, T., Angulo, S., Rhinn, H., Rhee, D., … others. (2011). Directed conversion of Alzheimer's disease patient skin fibroblasts into functional neurons. *Cell*, *146*(3), 359–371.

Ren, S., Chen, P., Jiang, H., Mi, Z., Xu, F., Hu, B., … Zhu, Z. (2014). Persistent sodium currents contribute to $A\beta_{1\text{-}42}$-induced hyperexcitation of hippocampal CA1 pyramidal neurons. *Neuroscience Letters*, *580*, 62–67.

Roses, M. A. D. (1996). Apolipoprotein E alleles as risk factors in Alzheimer's disease. *Annual Review of Medicine*, *47*(1), 387–400.

Rönicke, R., Mikhaylova, M., Rönicke, S., Meinhardt, J., Schröder, U. H., Fändrich, M., … Reymann, K. G. (2011). Early neuronal dysfunction by amyloid-β oligomers depends on activation of NR2B-containing NMDA receptors. *Neurobiology of Aging*, *32*(12), 2219–2228.

Schnabel, J. (2008). Neuroscience: standard model. *Nature News*, *454*(7205), 682–685.

Seubert, P., Vigo-Pelfrey, C., Esch, F., Lee, M., Dovey, H., Davis, D., … others. (1992). Isolation and quantification of soluble Alzheimer's β-peptide from biological fluids.

Shankar, G. M., Bloodgood, B. L., Townsend, M., Walsh, D. M., Selkoe, D. J. & Sabatini, B. L. (2007). Natural oligomers of the Alzheimer amyloid-β protein induce reversible synapse loss by modulating an NMDA-type glutamate receptor-dependent signaling pathway. *The Journal of Neuroscience*, *27*(11), 2866–2875.

Shibata, M., Yamada, S., Kumar, S. R., Calero, M., Bading, J., Frangione, B., … others. (2000). Clearance of Alzheimer's amyloid-$\beta_{1\text{-}40}$ peptide from brain by LDL receptor-related protein-1 at the blood-brain barrier. *Journal of Clinical Investigation*, *106*(12), 1489.

Sombati, S. & Delorenzo, R. J. (1995). Recurrent spontaneous seizure activity in hippocampal neuronal networks in culture. *Journal of Neurophysiology*, *73*(4), 1706–1711.

Spicer, J. A. (2008). New small-molecule inhibitors of mitogen-activated protein kinase kinase.

Stine, W. B., Dahlgren, K. N., Krafft, G. A. & LaDu, M. J. (2003). In vitro characterization of conditions for amyloid-β peptide oligomerization and fibrillogenesis. *Journal of Biological Chemistry*, *278*(13), 11612–11622.

Strodel, B., Lee, J. W., Whittleston, C. S. & Wales, D. J. (2010). Transmembrane structures for Alzheimer's $A\beta_{1-42}$ oligomers. *Journal of the American Chemical Society*, *132*(38), 13300–13312.

Takahashi, K., Tanabe, K., Ohnuki, M., Narita, M., Ichisaka, T., Tomoda, K. & Yamanaka, S. (2007). Induction of pluripotent stem cells from adult human fibroblasts by defined factors. *Cell*, *131*(5), 861–872.

Takahashi, K. & Yamanaka, S. (2006). Induction of pluripotent stem cells from mouse embryonic and adult fibroblast cultures by defined factors. *Cell*, *126*(4), 663–676.

Tang, X., Zhou, L., Wagner, A. M., Marchetto, M. C., Muotri, A. R., Gage, F. H. & Chen, G. (2013). Astroglial cells regulate the developmental timeline of human neurons differentiated from induced pluripotent stem cells. *Stem Cell Research*, *11*(2), 743–757.

Thinakaran, G. & Koo, E. H. (2008). Amyloid precursor protein trafficking, processing, and function. *Journal of Biological Chemistry*, *283*(44), 29615–29619.

Tsodyks, M., Uziel, A., Markram, H. & others. (2000). Synchrony generation in recurrent networks with frequency-dependent synapses. *J Neurosci*, *20*(1), 825–835.

Turrigiano, G. G. (2008). The self-tuning neuron: synaptic scaling of excitatory synapses. *Cell*, *135*(3), 422–435.

Turrigiano, G. G., Leslie, K. R., Desai, N. S., Rutherford, L. C., Nelson, S. B. & others. (1998). Activity-dependent scaling of quantal amplitude in neocortical neurons. *NATURE-LONDON-*, 892–895.

Varga, E., Juhász, G., Bozsó, Z., Penke, B., Fülöp, L. & Szegedi, V. (2014). Amyloid-β 1-42 Disrupts Synaptic Plasticity by Altering Glutamate Recycling at the Synapse. *Journal of Alzheimer's Disease*.

Vazin, T., Ball, K., Lu, H., Park, H., Ataeijannati, Y., Head-Gordon, T., … Schaffer, D. V. (2014). Efficient derivation of cortical glutamatergic neurons from human pluripotent stem cells: A model system to study neurotoxicity in Alzheimer's disease. *Neurobiology of Disease*, *62*, 62–72.

Verkhratsky, A. & Butt, A. M. (2007). *Glial neurobiology* (pp. 78–79). John Wiley & Sons.

Vierbuchen, T., Ostermeier, A., Pang, Z. P., Kokubu, Y., Südhof, T. C. & Wernig, M. (2010). Direct conversion of fibroblasts to functional neurons by defined factors. *Nature*, *463*(7284), 1035–1041.

Walsh, D. M., Klyubin, I., Fadeeva, J. V., Cullen, W. K., Anwyl, R., Wolfe, M. S., … Selkoe, D. J. (2002). Naturally secreted oligomers of amyloid-β protein potently inhibit hippocampal long-term potentiation in vivo. *Nature*, *416*(6880), 535–539.

Walsh, D. M. & Selkoe, D. J. (2007). Aβ oligomers – a decade of discovery. *Journal of Neurochemistry*, *101*(5), 1172–1184.

Walz, W., Boulton, A. A. & Baker, G. B. (2002). *Patch-clamp analysis: advanced techniques* (p. 42). Springer Science & Business Media.

Weller, R. O., Djuanda, E., Yow, H.-Y. & Carare, R. O. (2009). Lymphatic drainage of the brain and the pathophysiology of neurological disease. *Acta Neuropathologica*, *117*(1), 1–14.

Williams, S. R. & Mitchell, S. J. (2008). Direct measurement of somatic voltage clamp errors in central neurons. *Nature Neuroscience*, *11*(7), 790–798.

Yagi, T., Ito, D., Okada, Y., Akamatsu, W., Nihei, Y., Yoshizaki, T., … Suzuki, N. (2011). Modeling familial Alzheimer's disease with induced pluripotent stem cells. *Human Molecular Genetics*, *20*(23), 4530–4539.

6 Appendix

6.1 Abbreviations

AD	Alzheimer's disease
AHP	afterhyperpolarization
AM	acetoxymethyl
AMPA	α-amino-3-hydroxy-5-methyl-4-isoxazolepropionic acid
AP	action potential
APP	amyloid precurosr protein
Ara-C	arabinofuranosyl cytidine
Aβ	amyloid-β peptide
BMP	bone morphogenic protein
CNS	central nervous system
DAPI	4',6-diamidino-2-phenylindole
ddH_2O	double-distilled water
DM	dorsomorphin
DMSO	dimethyl sulfoxide
DPBS-/-	DPBS without calcium and magnesium
e	euler's number
EB	embryoid body
ELISA	enzyme-linked immunosorbent assay
EPSP	excitatory postsynaptic potential
EthD-1	ethidium homodimer
FAD	familial Alzheimer's disease
GABA	γ-aminobutyric acid
GAD67	glutamate decarboxylase 67
GFAP	glial fibrillary acidic protein
glia- cultures	low glia cultures
glia+ cultures	glial cell enriched cultures
HFIP	hexafluoro-2-propanol
IDE	insulin degrading enzyme
iPSCs	induced pluripotent stem cells
$K_d(Ca^{2+})$	dissociation constant for the binding of calcium ions
λ_{Em}	Emission wavelength

λ_{Ex}	Excitation wavelength
LRP-1	lipoprotein receptor like protein
LTD	long term depression
LTP	long term potentiation
MAP2	microtubule-associated protein 2
MEK1/2	mitogen-activated protein kinase kinase 1/2
mEPSC	miniature excitatory postsynaptic current
mPSC	miniature postsynaptic current
NBQX	2,3-dihydroxy-6-nitro-7-sulfamoyl-benzo[f]quinoxaline-2,3-dione
NCAM	neuronal cell adhesion molecule
NMDA	N-Methyl-D-aspartic acid
NPC	neuronal progenitor cell
PAGE	polyacrylamid gel electrophoresis
PD	PD0325901
RAGE	receptor for advanced glycation endproducts
RMP	resting membrane potential
ROI	region of interest
SDS	Sodium dodecyl sulfate
SNARE	soluble N-ethylmaleimide-sensitive factor attachment proteinreceptor
SPARC	secreted protein acidic and rich in cysteine
TTX	tetrodotoxin
τ	tau

6.2 Units and SI prefixes

Units		SI prefixes	
d	day	G	giga, 10^{9}
h	hour	m	milli, 10^{-3}
min	minute	µ	micro, 10^{-6}
s	second	n	nano, 10^{-9}
Hz	hertz		
m	meter		
M	molarity, mol/liter		
l	liter		
V	volt		
A	ampere		
Ω	ohm		
F	farad		
g	gram		

6.3 List of figures

6.4 Scripts and macros

6.4.1 ImageJ macro for the analysis of calcium imaging data

```
macro "Analyse Fluo-4 image stack"{
  //get analysis information
  new_ROIs=getBoolean("Create new regions (Old RIOs are deleted)?")

  if (new_ROIs==true){
    run("Select All");
    run("Add to Manager");
    roiManager("Deselect");
    roiManager("Delete");
    Dialog.create("Analysis Settings");
    Dialog.addMessage("Please select analysis settings.");
    Dialog.addCheckbox("KCl signal", true);
    Dialog.addCheckbox("Automatic thresholding", true);
    Dialog.addCheckbox("Create background region", true);
    Dialog.addCheckbox("Close stack after analysis", false);
    Dialog.addCheckbox("Clear ROIs after analysis (ROIs are still
      saved)",false);
    Dialog.addCheckbox("Only create ROIs (no intensity measurement will be
      done)", false);
    Dialog.addCheckbox("Run Watershed (divide ROIs into smaller ones)",
      false);
    Dialog.show;
    kcl_check = Dialog.getCheckbox();
    autothreshold_check = Dialog.getCheckbox();
    bg=Dialog.getCheckbox();
    close_image=Dialog.getCheckbox();
    roi_delete=Dialog.getCheckbox();
    roi_only=Dialog.getCheckbox();
    watershed=Dialog.getCheckbox();
    if (kcl_check==true){
      kcl=getNumber("Slice number, at which KCl was added:", 300);
    }
  } else {
    Dialog.create("Analysis Settings");
    Dialog.addMessage("Please select analysis settings.");
    Dialog.addCheckbox("Close stack after analysis", true);
    Dialog.addCheckbox("Clear ROIs after analysis (ROIs are still saved)",
      true);
    Dialog.show;
    close_image=Dialog.getCheckbox();
    roi_delete=Dialog.getCheckbox();
    roi_only=false;
  }

  //get and save image path and name for proper result files naming
  dir = getDirectory("image");
  name=getTitle;
  path=dir+name;
  getDimensions(width, hight, channels, slices, frames);

  if (new_ROIs==true){

    if (bg==true){
      //create maximum projection
      run("Z Project...", "start=1 stop="+slices+" projection=[Max
      Intensity]");
      //create threshold of background
      setAutoThreshold("Percentile");
      run("Convert to Mask");
```

```
    run("Options...", "iterations=1 count=1 pad edm=Overwrite
      do=Nothing");
    run("Erode");
    run("Erode");
    run("Open");
    run("Median...", "radius=4");
    //select thresholded area
    run("Create Selection");
    //add to ROI manager, this means that ROI_1 will be the background
      signal
    //roiManager("Add");
    roiManager("Set Color", "red");
    run("Add to Manager");
    close();
    selectWindow(name);
  }

  if (kcl_check==true){
    //Analysis with KCl response present
    selectWindow(name);
    //threshold KCl signal;
    //duplicate original stack and create offset stack to subtract;
    //"slices" is the number of slices in the stack.
    slice_end=slices-1;
    //define start of KCl signal integration to slices
    start=kcl-2;  before addition

    //make sure that the end is not defined higher than the last slice.
    if (kcl+4>slice_end){
      end = slice_end;
    } else {
      end=kcl+4;
    }

    //select the original window.
    selectWindow(name);
    //duplicate the whole original stack from the KCl start to the end
      (+end) and name it "original.tif".
    run("Duplicate...", "title=Original.tif duplicate
      range="+start+"-"+end);
    //select the original window
    selectWindow(name);
    //shift positions by 1 slice
    start=start+1;
    end=end+1;
    run("Duplicate...", "title=Offset.tif duplicate
      range="+start+"-"+end);
    //there are now 2 duplicate stacks with the KCl signal in them, while
      the two copies are offset by one image from another
    //select the offset stack
    selectWindow("Offset.tif");
    //add constant value to image to avoid negative pixels after
      subtraction
    run("Add...", "value=255 stack");
    //actual subtraction of the two stacks
    imageCalculator("Subtract stack", "Offset.tif","Original.tif");
    //select duplicate of original
    selectWindow("Original.tif");
    //close it
    close();
    //select subtracted stack
    selectWindow("Offset.tif");
    //get actual slice number of subtracted slice
    getDimensions(width, hight, channels, slices, frames);
    //create maximum projection
    run("Z Project...", "start=1 stop="+slices-1+" projection=[Max
      Intensity]");
```

```
  //select offset stack
  selectWindow("Offset.tif");
  //close it
  close();
  //select the amximum projection image
  selectWindow("MAX_Offset.tif");
} else {
//Analysis without KCl signal present
  selectWindow(name);
  slice_end=slices-1;
  //duplicate original stack and create offset stack to subtract
  run("Duplicate...", "title=Original.tif duplicate
    range="+1+"-"+slice_end);
  selectWindow(name);
  run("Duplicate...", "title=Offset.tif duplicate
    range="+2+"-"+slices);
  //add value to avoid negative pixels after subtraction
  selectWindow("Offset.tif");
  run("Add...", "value=255 stack");
  //subtract
  imageCalculator("Subtract stack", "Offset.tif","Original.tif");
  //close duplicate of original
  selectWindow("Original.tif");
  close();
  //create maximum projection
  selectWindow("Offset.tif");
  run("Z Project...", "start=1 stop="+slices-1+" projection=[Max
    Intensity]");
  //close stack
  selectWindow("Offset.tif");
  close();
  selectWindow("MAX_Offset.tif");
}

//threshold maximum projection
selectWindow("MAX_Offset.tif");
//background subtraction
run("Subtract Background...", "rolling=100 sliding slice");

if (autothreshold_check==true){
  //automatic thresholding
  setAutoThreshold("Moments dark");
  run("Convert to Mask");
} else {
  //manual thresholding
  run("Threshold...");
  selectWindow("Threshold");
  waitForUser("Set Threshold","Adjust the threshold and apply it.");
  selectWindow("Threshold");
  close();
}

//signal conditioning
selectWindow("MAX_Offset.tif");
//filter
run("Median...", "radius=2 slice");

//seperate merged somata
if (watershed==true){
  run("Watershed");
}

//create RIOs around fitting objects
roiManager("Set Color", "green");
run("Analyze Particles...", "size=10-Infinity circularity=0.30-1.00
  show=Nothing add");
selectWindow("MAX_Offset.tif");
```

```
    close();
  }

  //save ROIs
  ROIpath=path+"_roi.zip";
  roiManager("Save", ROIpath);
  //transfer ROIs to original stack
  selectWindow(name);
  roiManager("Show All");

  if (roi_only==false){
    //measure average intensity per ROI
    run("Set Measurements...", "  mean redirect=None decimal=3");
    roiManager("Deselect");
    roiManager("Multi Measure");
    //save results
    Resultspath=path+"_results.txt";
    saveAs("Results", Resultspath);
  }

//close images

  if (close_image==true){
    //close open images
    selectWindow(name);
    close();
  }

  if (roi_only==false){
    selectWindow("Results");
    run("Close");
  }

  //delete ROIs
  if (roi_delete==true){
    roiManager("Delete");
    selectWindow("ROI Manager");
    run("Close");
  }

} //end of macro
```

6.4.2 Synchronous burst detection from calcium imaging data

6.4.2.1 Formulae

Caclulation of ΔF/F signal was adapted from Jia et al. (2011). Fluorescence traces F(t) from the table output by ImageJ macro (see 6.4.1 ImageJ macro for the analysis of calcium imaging data) were smoothed to $F_S(t)$ by taking the mean of time windows of size k = 5 s around each timepoint t (equation 1). A baseline trace $F_0(t)$ was calculated as the minimum of $F_s(t)$ in time windows of size k around each timepoint t (equation 2). The relative fluorescence R(t) was defined as the ratio of F(t) minus $F_0(t)$ to $F_0(t)$ (equation 3). The final ΔF/F signal was achieved by taking the mean of R(t) in time windows of size i = 3 s around each timepoint t, thus denoising R(t).

$$(1)\ F_S(t) = \frac{1}{k}\sum_{t-\frac{k}{2}}^{t+\frac{k}{2}} F(t)$$

$$(2)\ F_0(t) = min_{t-\frac{k}{2}}^{t+\frac{k}{2}}\ F_S(t)$$

$$(3)\ R(t) = \frac{F(t) - F_0(t)}{F_0(t)}$$

$$(4)\ \Delta F/F = \frac{1}{i}\sum_{t-\frac{i}{2}}^{t+\frac{i}{2}} R(t)$$

6.4.2.2 R script

```
#measure execution time
start_time <- proc.time()
#analysis parameters
t_smooth_window_size <- 5
t_baseline_window_size <- 5
t_FoF_smooth_window_size <- 3
threshold <- 0.006
burst_threshold <- 0.3
Background_column <- 1 #number of column with background signal
#load required libraries
#for zerocross
library("msProcess")
#for rollmean
```

```
require(zoo)
#open file(s)
FileGroup <- "141127" # experiment group, here 141127 as an example
FilePath <- paste("J:/Simon Klapper/Daten/Calcium/", FileGroup, "/",
  FileGroup, "-Analyzed", sep = "")
FileList <- list.files(path = FilePath, pattern= paste(FileGroup, "_[A-
  Z]*_TimeSeries_[0-9]{2}.stk_results.txt$",sep = ""))
filename <- paste(FilePath,"/",FileList,sep = "")
#prepare result table
burst_frequencies <- matrix(nrow=length(FileList), ncol=5)

#loop trough all files found
for (n in 1:length(FileList)){
  print (filename[n])
  burst_frequencies[n,1] <- filename[n]
  data <- read.table(filename[n])
  #remove background column
  data <- data[,-Background_column]

  if(length(data)==0){
    #error if no data present
    print("No data available, skipping file!")
    next
  }

  #find and remove "not a number" containing columns
  #find NaN positions
  NoNumbers <- which(is.na(data), arr.ind = TRUE)
  #remove duplicate values
  NoNumbers <- NoNumbers [-which(duplicated(NoNumbers[,2]))]
  #remove seleceted colums
  if (length(NoNumbers)>0) data <- data[,-NoNumbers]
  #ask for timepoint of KCl response
  KCl <- readline(prompt = "Is there a KCL addition in this trace (1 =
    yes)? ")
  if (KCl == 1) KCl_timepoint <- as.numeric(readline(prompt = "Enter the
    timepoint of addition: ")) else KCl_timepoint <- length(data[,1])+1
  x <- 1:length(data[,1]) #define x coordinates with 1 to length of first
    column
  ROIs <- length(data[1,]) #number of ROIs analysed
  if (ROIs<50) print("WARNING: Low ROI number!")
  #smooth data (formula 1)
  data_smoothed <- matrix(nrow=length(data[,1]), ncol=ncol(data))
  data_smoothed <- rollmean(x = data, k = t_smooth_window_size,fill = NA)
  #time-dependet baseline (formula 2)
  data_baseline <- matrix(nrow=length(data[,1]), ncol=ncol(data))
  data_baseline <- rollapply(data_smoothed, width = t_baseline_window_size,
    FUN = min, fill = NA)
  #delta F over F (formula 3)
  data_deltaFoF <- matrix(nrow=length(data[,1]), ncol=ncol(data))
  data_deltaFoF <- (data-data_baseline)/data_baseline
  #denoise delta F over F (formula 4)
  data_deltaFoF <- rollapply(data_deltaFoF, width =
    t_FoF_smooth_window_size, FUN = mean, fill = NA)
  #detect bursts
  #mean delta-FoF
  data_deltaFoF_mean <- rowMeans(data_deltaFoF)
  #plot traces
  y_scale <- c(min(data_mean)-5,max(data_mean)+5)
  y_scale_dFoF <- c(min(data_deltaFoF_mean, na.rm = TRUE),
    max(data_deltaFoF_mean[1:KCl_timepoint], na.rm = TRUE))
  plot(x,data_deltaFoF_mean ,type = "l", xlab="Time [s]", ylim =
    y_scale_dFoF, col = "black", ylab=expression(paste ("mean ",
    Delta ,"F/F", sep="")), main = paste(FileList[n],"Calcium
    Signal"))
  #thresholding
  data_burst_thresholded <- (data_deltaFoF_mean>threshold)*1
```

```
  if (1 %in% data_burst_thresholded
      [((t_smooth_window_size+t_baseline_window_size+
      t_FoF_smooth_window_size-3)/2):(KCl_timepoint-3)]) {
    data_burst_thresholded_crossed <- data_burst_thresholded*2-1
    data_burst <- zeroCross(data_burst_thresholded_crossed
      [((t_smooth_window_size+t_baseline_window_size+
      t_FoF_smooth_window_size-3)/2):(KCl_timepoint-3)], "positive")
    data_burst_frequency <- length(data_burst)/TimeToAnalyse*60
    burstNumber <- length(data_burst)
  } else {
    data_burst_thresholded_crossed <- -1
    burstNumber <- 0
    data_burst_frequency <- 0
  }

  print (paste("Bursts per minute:", round(data_burst_frequency,3)))
  #calculate mean traces
  data_mean <- rowMeans(data)
  data_smoothed_mean <- rowMeans(data_smoothed)
  data_baseline_mean <- rowMeans(data_baseline)

  #add detected bursts to plot
  if (burstNumber>0) points(x=data_burst+
    ((t_smooth_window_size+t_baseline_window_size+
    t_FoF_smooth_window_size-3)/2), y=rep(threshold, length(data_burst)),
    col = "red", pch = 6)

  #write results to table
  burst_frequencies[n,2] <- burstNumber
  burst_frequencies[n,3] <- data_burst_frequency
  burst_frequencies[n,4] <- ROIs
  burst_frequencies[n,5] <- TimeToAnalyse
  #write deltaF over F mean & bursts into file
  write_FoF <- matrix(nrow=length(data[,1]), ncol=3)
  data_mean <- rowMeans(data)
  data_mean <- data_mean-min(data_mean)
  write_FoF[,1] <- data_mean
  write_FoF[,2] <- data_deltaFoF_mean
  write_FoF[,3] <- data_burst_thresholded
  write.table(write_FoF, file = paste(filename[n], "_dFoFmean.txt",
    sep=""),
  row.names = FALSE, sep = "\t", quote = FALSE,col.names = c("Raw","dFoF",
    "Burst threshold"))
}

#write data into file
write.table(burst_frequencies, file = paste(FilePath, "/", FileGroup,
  "_burst_frequencies.txt", sep = ""),row.names = FALSE, sep = "\t", quote
  = FALSE, col.names = c("File", "Number of Bursts", "Bursts per minute",
  "Number of ROIs", "Analyzed length"))

#show execution time
print ("Execution time [s]:")
print (proc.time() - start_time)

#end of script
```

6.5 Curriculum vitae

Name	Simon Klapper
Date of birth	1985/08/24
Place of birth	Duisburg, Germany
Martial status	single

2011-2015	PhD student: Heinrich-Heine-Universität Düsseldorf, Germany
2006-2011	Studies of biology: Heinrich-Heine-Universität Düsseldorf, Germany Degree: Diploma of biology
2005-2006	Civillian service: Die Johanniter Oberhausen, Germany
1996-2005	Sophie-Scholl Gymansium Oberhausen, Germany
1992-1996	Grundschule Schwarze Heide Oberhausen, Germany

6.6 Publications and conferences

6.6.1 Publications

Andreyeva, A., Nieweg, K., Horstmann, K., Klapper, S., Müller-Schiffmann, A., Korth, C. & Gottmann, K. (2012). C-terminal fragment of N-cadherin accelerates synapse destabilization by amyloid-β. *Brain*, *135*(7), 2140–2154.

Manuscript in preparation:
Klapper, S., Gottmann, K. & Nieweg, K. Comparative characterization of human iPSC derived neural networks: Evidence for control of functional differentiation by glia.

6.6.2 Meetings and poster presentations

11/2013	SfN Neuroscience Meeting 2013, San Diego, USA Poster: Acceleration of Amyloid-β Induced Synapse Impairment.
07/2012	8th FENS Forum of Neuroscience, Barcelona, Spain Poster: C-terminal Fragment of N-cadherin Accelerates Synapse Destabilization by Amyloid-β.
03/2011	9th Göttingen Meeting of the German Neuroscience Society, Göttingen, Germany

7 Acknowledgment

First of all I would like to thank Prof. Dr. Kurt Gottmann for offering me the option to conduct this work in his lab under his excellent supervision. Thanks for fruitful discussions, constant help and support.

Thanks to Jun.-Prof. Dr. Katja Nieweg for the establishment of and cooperation concerning the work on the iPSC derived neurons. Further, I would like to thank Prof. Dr. Thomas Voigt for his help with the Fluo-4 based calcium imaging technique and the Department of Neuropathology for providing the 7PA2 CHO cell line. Thanks also to my lab colleagues for a nice cooperative working atmosphere and to the graduate school “GRK1033” for financial support.

Many thanks to Prof. Dr. Dieter Willbold for co-supervision of this work.

Last but not least I would like to thank all my friends and my family for their constant sympathy, patience and support.

8 Eidesstattliche Erklärung

Ich versichere hiermit an Eides statt, dass die vorliegende Dissertation von mir selbstständig und ohne unzulässige fremde Hilfe unter Beachtung der „Grundsätze zur Sicherung guter wissenschaftlicher Praxis an der Heinrich-Heine-Universität Düsseldorf“ erstellt worden ist. Diese Dissertation wurde keiner anderen Fakultät vorgelegt und es gab bisher keine erfolglosen Promotionsversuche.

Düsseldorf, den 21. April 2015,

Simon Klapper